Jordan Journal of
PHYSICS
An International Peer-Reviewed Research Journal

Volume 7, No. 2, 2014, 1436 H

Jordan Journal of Physics (*JJP*): An International Peer-Reviewed Research Journal issued by the support of the Scientific Research Support Fund, Ministry of Higher Education and Scientific Research, Jordan, and published quarterly by the Deanship of Research and Graduate Studies, Yarmouk University, Irbid, Jordan.

Manuscripts should be submitted to:

Prof. Nihad A. Yusuf
Editor-in-Chief, Jordan Journal of Physics
Deanship of Research and Graduate Studies
Yarmouk University-Irbid-Jordan
Tel. 00 962 2 7211111 Ext. 2075
E-mail: *jjp@yu.edu.jo*
Website: *http://Journals.yu.edu.jo/jjp*

Jordan Journal of
PHYSICS
An International Peer-Reviewed Research Journal

Volume 7, No. 2, 2014, 1436 H

The Hashemite Kingdom of Jordan

Yarmouk University

Jordan Journal of PHYSICS

An International Peer-Reviewed Research Journal issued by the Support of the Scientific Research Support Fund

Volume 7, No. 2, 2014, 1436 H

Instructions to Authors

Instructions to authors concerning manuscript organization and format apply to hardcopy submission by mail, and also to electronic online submission via the Journal homepage website (http://jjp.yu.edu.jo).

Manuscript Submission

1- **Hardcopy**: The original and three copies of the manuscript, together with a covering letter from the corresponding author, should be submitted to the Editor-in-Chief:

Professor Nihad A. Yusuf
Editor-in-Chief, Jordan Journal of Physics
Deanship of Scientific Research and Graduate Studies
Yarmouk University, Irbid, Jordan.
Tel: 00962-2-7211111, Ext. 2075
Fax: 00962-2-7211121
E-mail: jjp@yu.edu.jo

2- **Online**: Follow the instructions at the journal homepage website.

Original *Research Articles*, *Communications* and *Technical Notes* are subject to critical review by minimum of two competent referees. Authors are encouraged to suggest names of competent reviewers. *Feature Articles* in active Physics research fields, in which the author's own contribution and its relationship to other work in the field constitute the main body of the article, appear as a result of an invitation from the Editorial Board, and will be so designated. The author of a *Feature Article* will be asked to provide a clear, concise and critical status report of the field as an introduction to the article. *Review Articles* on active and rapidly changing Physics research fields will also be published. Authors of *Review Articles* are encouraged to submit two-page proposals to the Editor-in-Chief for approval. Manuscripts submitted in *Arabic* should be accompanied by an Abstract and Keywords in English.

Organization of the Manuscript

Manuscripts should be typed double spaced on one side of A4 sheets (21.6 x 27.9 cm) with 3.71 cm margins, using Microsoft Word 2000 or a later version thereof. The author should adhere to the following order of presentation: Article Title, Author(s), Full Address and E-mail, Abstract, PACS and Keywords, Main Text, Acknowledgment. Only the first letters of words in the Title, Headings and Subheadings are capitalized. Headings should be in **bold** while subheadings in *italic* fonts.

Title Page: Includes the title of the article, authors' first names, middle initials and surnames and affiliations. The affiliation should comprise the department, institution (university or company), city, zip code and state and should be typed as a footnote to the author's name. The name and complete mailing address, telephone and fax numbers, and e-mail address of the author responsible for correspondence (designated with an asterisk) should also be included for official use. The title should be carefully, concisely and clearly constructed to highlight the emphasis and content of the manuscript, which is very important for information retrieval.

Abstract: A one paragraph abstract not exceeding 200 words is required, which should be arranged to highlight the purpose, methods used, results and major findings**.**

Keywords: A list of 4-6 keywords, which expresses the precise content of the manuscript for indexing purposes, should follow the abstract.

PACS: Authors should supply one or more relevant PACS-2006 classification codes, (available at http://www.aip.org/pacs/pacs06/pacs06-toc.html)

Introduction: Should present the purpose of the submitted work and its relationship to earlier work in the field, but it should not be an extensive review of the literature (e.g., should not exceed 1 ½ typed pages).

Experimental Methods: Should be sufficiently informative to allow competent reproduction of the experimental procedures presented; yet concise enough not to be repetitive of earlier published procedures.

Results: should present the results clearly and concisely.

Discussion: Should be concise and focus on the interpretation of the results.

Conclusion: Should be a brief account of the major findings of the study not exceeding one typed page.

Acknowledgments: Including those for grant and financial support if any, should be typed in one paragraph directly preceding the References.

References: References should be typed double spaced and numbered sequentially in the order in which they are cited in the text. References should be cited in the text by the appropriate Arabic numerals, enclosed in square brackets. Titles of journals are abbreviated according to list of scientific periodicals. The style and punctuation should conform to the following examples:

1. Journal Article:

a) Heisenberg, W., Z. Phys. 49 (1928) 619.
b) Bednorz, J. G. and Müller, K. A., Z. Phys. B64 (1986) 189
c) Bardeen, J., Cooper, L.N. and Schrieffer, J. R., Phys. Rev. 106 (1957) 162.
d) Asad, J. H., Hijjawi, R. S., Sakaji, A. and Khalifeh, J. M., Int. J. Theor. Phys. 44(4) (2005), 3977.

2. Books with Authors, but no Editors:

a) Kittel, C., "Introduction to Solid State Physics", 8th Ed. (John Wiley and Sons, New York, 2005), chapter 16.
b) Chikazumi, S., C. D. Graham, JR, "Physics of Ferromagnetism", 2nd Ed. (Oxford University Press, Oxford, 1997).

3. Books with Authors and Editors:

a) Allen, P. B. "Dynamical Properties of Solids", Ed. (1), G. K. Horton and A. A. Maradudin (North-Holland, Amsterdam, 1980), p137.
b) Chantrell, R. W. and O'Grady, K., "Magnetic Properities of Fine Particles" Eds. J. L. Dormann and D. Fiorani (North-Holland, Amsterdam, 1992), p103.

4. Technical Report:

Purcell, J. "The Superconducting Magnet System for the 12-Foot Bubble Chamber", report ANL/HEP6813, Argonne Natt. Lab., Argonne, III, (1968).

5. Patent:

Bigham, C. B., Schneider, H. R., US patent 3 925 676 (1975).

6. Thesis:

Mahmood, S. H., Ph.D. Thesis, Michigan State University, (1986), USA (Unpublished).

7. Conference or Symposium Proceedings:

Blandin, A. and Lederer, P. Proc. Intern. Conf. on Magnetism, Nottingham (1964), P.71.

8. Internet Source:

Should include authors' names (if any), title, internet website, URL, and date of access.

9. Prepublication online articles (already accepted for publication):

Should include authors' names (if any), title of digital database, database website, URL, and date of access.

For other types of referenced works, provide sufficient information to enable readers to access them.

Tables: Tables should be numbered with Arabic numerals and referred to by number in the Text (e.g., Table 1). Each table should be typed on a separate page with the legend above the table, while explanatory footnotes, which are indicated by superscript lowercase letters, should be typed below the table.

Illustrations: Figures, drawings, diagrams, charts and photographs are to be numbered in a consecutive series of Arabic numerals in the order in which they are cited in the text. Computer-generated illustrations and good-quality digital photographic prints are accepted. They should be black and white originals (not photocopies) provided on separate pages and identified with their corresponding numbers. Actual size graphics should be provided, which need no further manipulation, with lettering (Arial or Helvetica) not smaller than 8 points, lines no thinner than 0.5 point, and each of uniform density. All colors should be removed from graphics except for those graphics to be considered for publication in color. If graphics are to be submitted digitally, they should conform to the following minimum resolution requirements: 1200 dpi for black and white line art, 600 dpi for grayscale art, and 300 dpi for color art. All graphic files must be saved as TIFF images, and all illustrations must be submitted in the actual size at which they should appear in the journal. Note that good quality hardcopy original illustrations are required for both online and mail submissions of manuscripts.

Text Footnotes: The use of text footnotes is to be avoided. When their use is absolutely necessary, they should be typed at the bottom of the page to which they refer, and should be cited in the text by a superscript asterisk or multiples thereof. Place a line above the footnote, so that it is set off from the text.

Supplementary Material: Authors are encouraged to provide all supplementary materials that may facilitate the review process, including any detailed mathematical derivations that may not appear in whole in the manuscript.

Revised Manuscript and Computer Disks

Following the acceptance of a manuscript for publication and the incorporation of all required revisions, authors should submit an original and one more copy of the final disk containing the complete manuscript typed double spaced in Microsoft Word for Windows 2000 or a later version thereof. All graphic files must be saved as PDF, JPG, or TIFF images.

Allen, P.B., "…….", in: Horton, G.K., and Muradudin, A. A., (eds.), "Dynamical…….", (North……..), pp….

Reprints

Twenty (20) reprints free of charge are provided to the corresponding author. For orders of more reprints, a reprint order form and prices will be sent with the article proofs, which should be returned directly to the Editor for processing.

Copyright

Disclaimer

Indexing

JJP is currently applying for indexing and abstracting to all related International Services.

Jordan Journal of
PHYSICS
An International Peer-Reviewed Research Journal

Volume 7, No. 2, 2014, 1436 H

Table of Contents:

Volume 7, Number 2, 2014. pp. 53-63

Jordan Journal of Physics

ARTICLE

One-Step Synthesis of Fe-Doped ZnO Thin Films by a Convenient Electrochemical Technique at Room Temperature

M. A. Awawdeh[a], K. Al-Heuseen[b] and I. M. Odeh[a]

[a] *Department of Physics, Yarmouk University, Irbid, Jordan.*
[b] *Ajloun University College, Al-Balqa Applied University, Ajloun, Jordan.*

Received on: 9/9/2013; Accepted on: 18/5/2014

Abstract: This paper reports on the synthesis and characterization of Fe-doped ZnO thin films deposited onto gold coated glass substrates, using electrochemical deposition (ECD) technique at room temperature and different concentrations of Fe. X-ray diffraction (XRD), scanning electron microscopy (SEM), photoluminescence (PL) and optical transmission measurements were used to characterize the films. The effect of iron doping on the structural, morphological and optical properties of the films was studied. The XRD spectra of the Fe-ZnO films indicate the polycrystalline nature having hexagonal crystal structure. From the XRD pattern, it is observed that peak positions shift toward lower angles with Fe doping. The change in the peak positions with increase in Fe content clearly indicates that Fe ions replace Zn ions in the ZnO films. The SEM images showed different surface morphologies of the grown structures on the gold layer according to the doping concentration. The shape and dimensions of the structures depend on the doping level. The PL spectra illustrate that there is an obvious red-shift for the emission centre from ultraviolet to blue region. The intensities of emissions from defects increase with the increase of Fe doping. The growth and doping mechanism was also briefly discussed.
Keywords: Fe-doped ZnO thin films; Nanomaterials; Doping; Electrochemical deposition; ZnO.

Introduction

Transparent metal oxide films are of paramount technological importance for solar cells, chemical sensors, liquid crystal displays and as nano porous films for dye sensitized solar cells. Among these metal oxides, wide direct band-gap zinc oxide (ZnO) has gained increasing attention because of its promising properties. ZnO has a broad range of applications, such as light-emitting diodes, photo detectors and gas sensors [1-4]. The interest in ZnO is due to its unique properties, such as a relatively high exciton binding energy (60 MeV), wide band gap (3.34 eV at 300 K), piezoelectric behavior and the fact that it is a biocompatible material.

The undoped/doped ZnO can be fabricated using various methods, such as radio frequency plasma [5], ion-assisted cyclic sputtering [6], RF sputtering [7], thermal oxidation [8], electron beam evaporation [9], activated reactive evaporation [10], spray pyrolysis [11], low-pressure metal organic chemical vapor deposition (MOCVD) [12], chemical bath deposition [13] and electrodeposition [14].

Compared to other techniques, electrochemical methods offer several advantages including fast, simple, low cost operation at near room temperature, large-scale deposition area and the ability to control composition, crystallinity and the properties of the deposit by adjusting deposition conditions. It is interesting that the electrodeposition of ZnO can also produce a variety of different morphological deposits [15]. In addition, the

Corresponding Author: M. A. Awawdeh **Email**: amufeed@yu.edu.jo.

preparation of ZnO by electrodeposition is also eco-friendly because normally no toxic chemicals are used in the electrolytic bath [15-17]. Moreover, the deposition process can be carried out on various substrates such as glass, polymers, semiconductors and templates. There are no special requirements needed for the substrates, except that they should be conductive. Therefore, this technique is well adapted for industrial procedures in the fabrication of ZnO thin films.

Furthermore, ZnO thin films are also considered as a host material for diluted magnetic semiconductors (DMS) by transition metal elements doping [18-21]. The possibility of synthesizing ferromagnetic ZnO nanostructures is particularly encouraging, since this will enable several promising applications in the fields of spintronics and optoelectronics.

However, several inconsistent results have been obtained for the Fe-doped ZnO films. Polyakov et al. [22] found room temperature ferromagnetism by implanting Fe ions in a ZnO crystal grown by vapour phase, while Janisch et al. [23] reported that Fe-doped ZnO showed a paramagnetic behavior. In order to clarify this discrepancy, it is important to disclose the effect of doped-Fe on the structure and properties of ZnO thin films. For the Fe-doped ZnO materials, the results of some theoretical studies show that they can possess ferromagnetic properties at room temperature [24, 25]; therefore, most of the researchers mainly studied the ferromagnetic behavior of Fe-doped ZnO thin films [26-28]. There are few reports on their structural, optical and electrical properties. However, Fe-doped ZnO thin film could be an important multi-functional material; hence, it is important to study its structural, optical and electrical properties and the correlation between them.

In this work, we prepared Fe-doped ZnO nanostructures at room temperature by electrochemical techniques on gold coated glass substrates in an aqueous solution. The novelty of synthesis of thin films at room temperature is to reduce the thermal mismatch between films and substrates. The effect of Fe-doping concentration on the structural and optical properties of ZnO nanostructure was investigated. Structural and optical properties were investigated by scanning electron microscopy (SEM), X-ray diffraction (XRD) and photoluminescence (PL) spectroscopy.

Experimental Procedure

Fe doped ZnO nanostructures were deposited by electrochemical deposition (ECD) using 0.1 M Zn $(NO_3)_2$ aqueous solutions and a stock solution of 4.13 mM Fe $(NO_3)_3$ dissolved in deionized water. To adjust the composition of the deposits, the concentrations of Fe $(NO_3)_3$ in the baths were 10 µl, 20 µl, 30 µl and 40 µl. These correspond to the concentrations of Fe ions in the bath of 0.06 mM, 0.12 mM, 0.18 mM and 0.24 mM, respectively.

A simple two-electrode homemade Teflon cell was constructed using a platinum wire as an anode and the gold coated glass substrate as a cathode. The gold coating is sufficiently thin such that it allows transmittance measurements unhindered. The thicknesses of gold layers were about 20 nm. The distance between the anode and the substrate was about 5 mm. A constant electrodeposition current density of 3 mA/cm^2 producing the highest deposition rate was applied for 30 min. The good conducting gold layer was used to reduce the stress in the deposited films and to increase the deposition rate.

The possible electro-deposition mechanism of ZnO through nitrate precursors can be summarized as follows:

First, the reduction of nitrate ions produces nitrite and hydroxide ions in water. Then, Zn ions interact with hydroxide ions, forming Zinc Hydroxides. After dehydration of Zn $(NO_3)_2$, the final product ZnO forms [29].

$$Zn(NO_3)_2 + H_2O \rightarrow Zn^{2+} + NO_3^{1-} \quad (1)$$

$$NO_3^{1-} + H_2O + 2e^- \rightarrow NO_2^{1-} + 2OH^- \quad (2)$$

$$Zn^{2+} + 2OH^{1-} \rightarrow Zn(OH)_2 \quad (3)$$

$$Zn(OH)_2 \rightarrow ZnO + H_2O \quad (4)$$

Since iron oxides thin films were electrodeposited in an aerated solution, there are two possible reactions to accomplish the formation of Fe_2O_3.

Reaction 1

Dissolved oxygen can be reduced and then react with ferric ions to form Fe_2O_3 as in the following reaction:

$$4Fe^{3+} + 3O_2 + 12e^- \rightarrow 2Fe_2O_3 \quad (5)$$

This reaction is limited by the concentration of the dissolved oxygen.

Another possible reaction is manifested *via* water dissociation as shown in Eq. (6a). This enhances the formation of ferric hydroxide as in Eq. (6b). Ferric hydroxide is converted into Fe_2O_3 as in Eq. (6c). The overall reaction is shown in Eq. (6d). Due to the low dissolved oxygen concentration in the reaction cell, this suggests that reaction 2 is the predominant electrodeposition reaction pathway [30].

Reaction 2

$$6H_2O + 6e^- \rightarrow 3H_2\,(g) + 6OH^- \quad (6a)$$

$$2Fe^{3+} + 6OH^- \rightarrow 2\,Fe(OH)_3 \quad (6b)$$

$$2\,Fe(OH)_3 \rightarrow Fe_2O_3 + 3H_2O \quad (6c)$$

$$2Fe^{3+} + 6H_2O + 6e^- \rightarrow Fe_2O_3 + 3H_2\,(g) \quad (6d)$$

Finally, the synthesized products were characterized by X-ray diffraction (XRD), scanning electron microscopy (SEM) and photoluminescence (PL) spectroscopy.

High resolution XRD (PANalytical X'pert Pro MRD) with a Cu-Kα_1 radiation source (λ = 1.5406 Å) is used to assess the crystalline quality and the lattice parameters of the samples which can also be determined from the peak position. Under high resolution measurements, this system has a resolution of 12 arcsec. The grain structure and stoichiometry of the prepared samples were examined by scanning electron microscope (SEM FEI Quanta 200) equipped with energy dispersive X-ray spectroscopy (EDAX) facility for elemental analysis.

For SEM characterization, normally the measurements were performed at 10 kV to measure the surface morphology of the samples.

Photoluminescence (PL) measurements were performed by using Jobin Yvon HR800UV spectrometer system that is an integrated confocal micro-photoluminescence spectrometer. A helium cadmium (He-Cd) laser (325 nm) and an argon ion laser (514.5 nm) were used as excitation sources for PL measurements; the incident laser power was 20 mW.

Results and Discussion

Fig.1 (A) shows XRD spectra of (a) pure ZnO, (b) 0.06 mM Fe, (c) 0.12 mM Fe, (d) 0.18 mM Fe and (e) 0.24 mM Fe-doped ZnO thin films, respectively. In all cases, the observed diffraction peaks can be indexed to standard hexagonal wurtzite ZnO structure, indicating that Fe-doping did not change the hexagonal wurtzite structure of ZnO films. Seven peaks appear in the diffraction spectrum in the 2θ interval of 30-70^o and correspond to (100), (002), (101), (102), (110), (103) and (112) orientations of the ZnO hexagonal structure. The film formed is polycrystalline with a preferential orientation of the (002) diffraction peak, showing that the film is preferentially oriented along the c-axis direction. This indicates that this axis in the ZnO film tends to grow perpendicular to the substrate surface [31]. In the XRD pattern, characteristic peaks of the (111) gold substrate also appears.

Fig. 1B shows the main characteristic peaks ((100), (002), (101)) of wurtzite structure in order to see a close view and the impact of the dopant ions in the pristine ZnO lattice. The peaks are shifted to lower angles and the intensity decreased with increasing Fe doping concentration compared to those of pure bulk ZnO, which is consistent with that of other Fe-doped ZnO films [31]. This shift in peak positions clearly reflects that Fe replaces Zn in the ZnO films. Meanwhile, it was apparent that the intensity and the full width at half maximum (FWHM) of (002) diffraction peak decreases with the increment of Fe concentration, implying that more Fe concentration in ZnO films improves the ZnO film crystallinity.

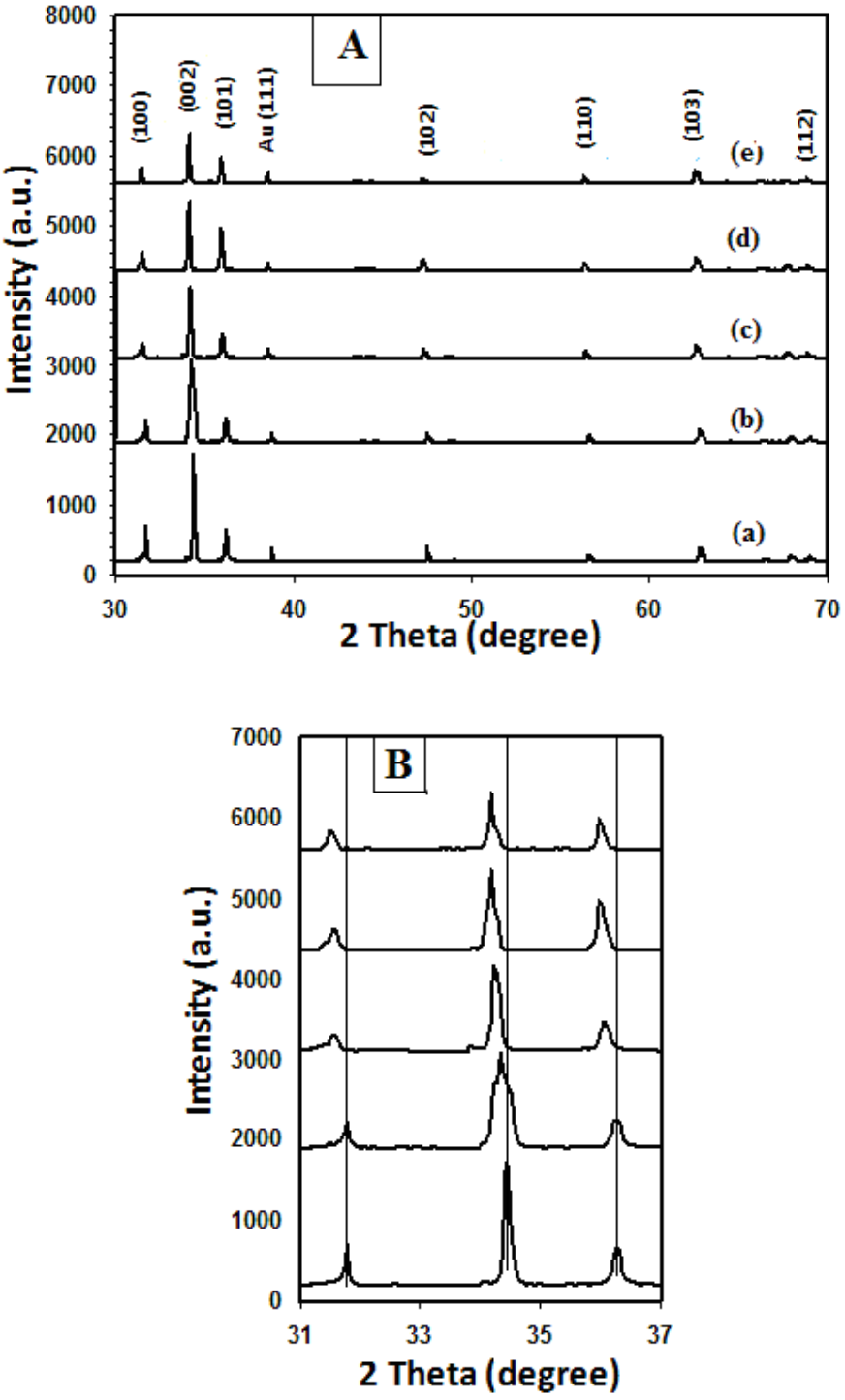

FIG. 1. (A) XRD spectra of of (a) pure ZnO, (b) 0.06 mM Fe, (c) 0.12 mM Fe, (d) 0.18 mM Fe and (e) 0.24 mM Fe-doped ZnO thin films. FIG. 1(B) shows an XRD pattern of the three most intense peaks ((100), (002) and (101), showing shifting of the centre of diffraction toward the left.

This might be due to the lattice disorder and strain induced by interstitial Fe atoms or the substitution of Fe for Zn. The lattice constants of Fe doped ZnO were found to be slightly larger than those of pure bulk ZnO. The larger ionic radii of Fe^{+2} ions (0.63 Å) compared to Zn^{+2} ions (0.60 Å) in the tetrahedral coordination [33] tend to increase the size of the lattice in doped ZnO

films. An approximate average size, D, of Fe-ZnO crystal was calculated from the well-known Scherrer formula:

$$D = \frac{K\lambda}{\beta \cos\theta} \quad (7)$$

where; k is a constant equal to 0.9, λ is the incident X-ray wavelength and β is the FWHM in radian. For the pure ZnO sample, the average size D was found to be 70 nm, meanwhile the values of D for all doped samples are listed in Table 1. They obviously increased with doping concentrations. The out-of -plane (along c-axis) strain, ε_c, has been calculated from the relation $\varepsilon_c = \Delta c/c_0$ [34] and presented in Table 1,where; Δc is defined as the deviation of the calculated lattice parameter c from the corresponding unstrained values of bulk ZnO c_o = 5.206 Å. The positive values of the out-of-plane strain ε_c indicate that the strain caused by the substrate is tensile in all doped samples.

TABLE 1. Lattice constant (c), out-of -plane strain (ε_c) and average crystal size(D) determined for the Fe-ZnO samples deposited for different durations

Sample	c (Å)	ε_c (%)	D (nm)
0.06 mM Fe	5.216	0.192	31
0.12 mM Fe	5.230	0.461	61
0.18 mM Fe	5.242	0.691	65
0.24 mM Fe	5.242	0.691	86

Fig. 2 shows the scanning electron micrographs of the morphology of ZnO films deposited on gold coated glass substrates using ECD. The films were deposited for different additions of Fe; (0.06, 0.12, 0.18 and 0.24) mM, keeping the current density constant at 3 mA/cm^2 (corresponding to the applied potential voltage of 15 V). The SEM images show different surface morphologies of the grown structures according to the concentration of Fe. As the Fe-concentration increases, changes in the morphology of the films are observed. The surface morphology of the Fe-ZnO thin films shows a network of flake-like nanostructures and clearly revealed that the average size of surface flakes is increased with increasing the concentration of Fe doping, which is in agreement with other results [25]. The flakes are a mixture of small sizes from a micron to100 nm for 0.06 mM Fe (Fig.2b), larger, denser and more uniform flakes with two forms for 0.12 mM Fe (Fig.2c). As the concentration of Fe is increased over 0.18 mM Fe, the flakes become denser and like a continuous structure and the Fe_2O_3 becomes more dominant as shown in (Fig.2d) and (Fig.2e). That is to say, when Fe-doping concentration is less than 0.18 mM Fe, the Fe_2O_3 has little effect on the morphology of ZnO nanostructures. One could observe that the concentration of Fe has a significant effect on the morphology, the shape and the size of the films, such that the dimensions of the structures were observed to increase with increasing the concentration.

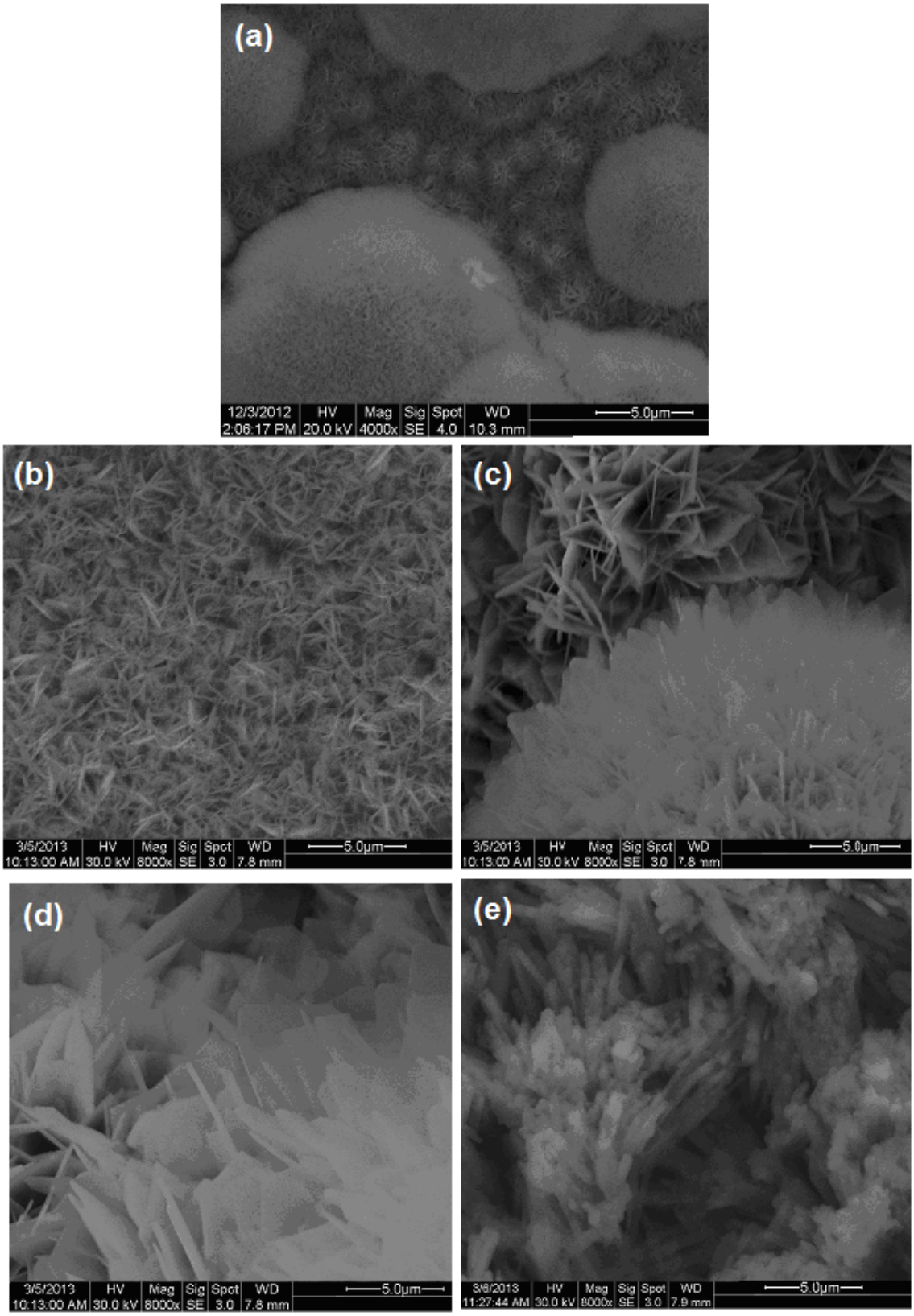

FIG. 2. The surface morphology (SEM) micrographs of (a) pure ZnO, (b) 0.06 mM Fe, (c) 0.12 mM Fe, (d) 0.18 mM Fe and (e) 0.24 mM Fe-doped ZnO thin films

FIG. 3 demonstrates the EDX image of pure and Fe-doped ZnO thin films. The ratios of Fe_2O_3 and ZnO were printed in the figure which shows that the ratio of Fe_2O_3 increased with doping.

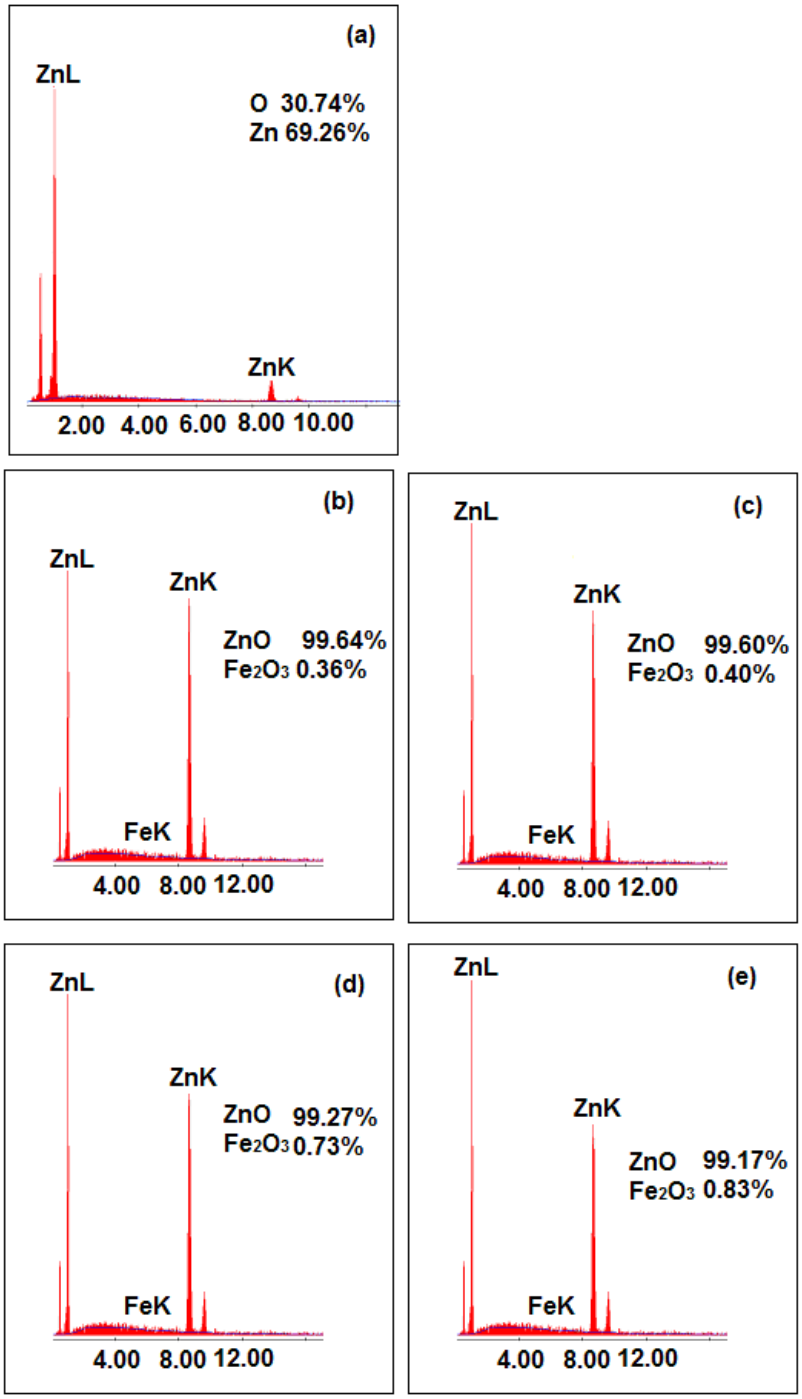

FIG. 3. The EDX spectra of (a) pure ZnO, (b) 0.06 mM Fe, (c) 0.12 mM Fe, (d) 0.18 mM Fe and (e) 0.24 mM Fe-doped ZnO thin films

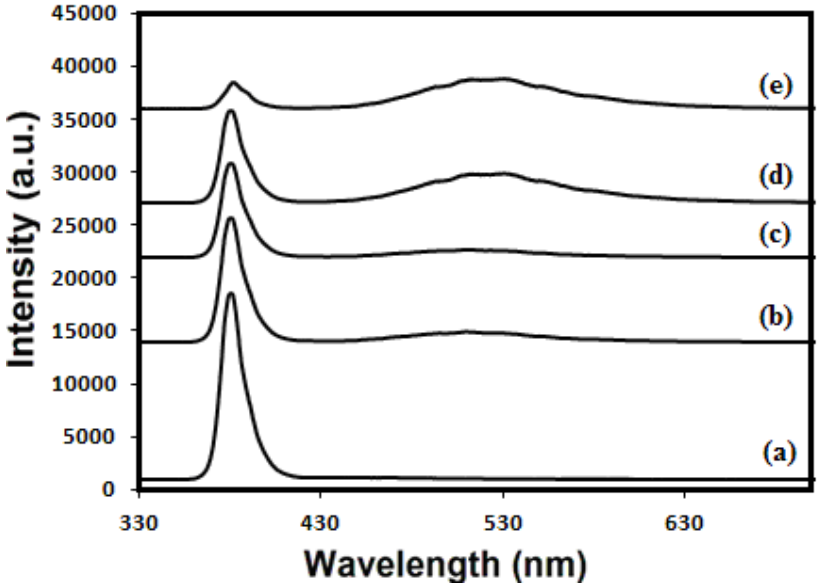

FIG. 4. Room temperature photoluminescence (PL) spectra of (a) pure ZnO, (b) 0.06 mM Fe, (c) 0.12 mM Fe, (d) 0.18 mM Fe and (e) 0.24 mM Fe-doped ZnO thin films

FIG. 4 shows the room-temperature photoluminescence spectra (330-700) nm of pure and Fe-doped ZnO thin films deposited on gold coated glass substrates. All the samples have an ultraviolet emission peak centered at 381 nm and a broad green-orange emission band ranging from (400 - 650) nm. The near band edge emission (NBE) centered at 381 nm is attributed to the irradiative recombination of a hole in the valence band and an electron in the conduction band also from free exciton [35, 36]. Therefore, the density of free exciton in ZnO thin films is the major factor affecting the intensity of ultraviolet emission. This tends to shift the peak continuously toward higher wavelength and broaden the peak with increasing doping concentration. The shift of the NBE emission peak has been attributed to the strong exchange interactions between the 'd' electrons of the doping ions, and the 's' and 'p' electrons of the host [37]. The green-orange emission band was related to defects; in addition, by increasing the concentration of the doping ions, there is a gradual increase in the intensity of the defect related peak. This indicates that the concentration of intrinsic defects (responsible for broad-band emission) increase with Fe doping in ZnO films. The doped captions may provide competitive pathways for recombination and result in quenching of the broad green-orange emission. It is clear from Fig. 4 that the intensity of ultraviolet emission has obviously decreased while the intensity of the green-orange emission band increased as Fe is added to ZnO thin film.

The above results show that the effect of Fe-doping on the luminescence behavior of ZnO is complex. The complexity is mainly associated with the following factors:

(1) The native point defects (including type and density) in ZnO are different due to the different preparation techniques of ZnO materials.

(2) The valence state of Fe in ZnO is not unique; that is to say, the doped Fe in ZnO may exist either in the form of Fe^{2+} or Fe^{3+} and even coexist in the form of Fe^{2+} and Fe^{3+}.

(3) The inclusion of iron ion which is larger than zinc ion by 6% into the ZnO thin films leads to an increase in the lattice parameter as in table 1 which in turn causes lattice strains by generating intrinsic defects or induces phase separation and/or precipitation of the dopant ions into interacting clusters [38]. This result is clearly manifested by the reduction of luminescence efficiency shown in Figure 4 and the appearance of clustering in SEM micrographs as the concentration of the dopant increases.

FIG. 5 shows the optical transmission spectra of Fe-doped ZnO thin films deposited on gold coated glass substrates at room temperature for different Fe doping concentrations in the corresponding wavelength range of 200-500 nm.

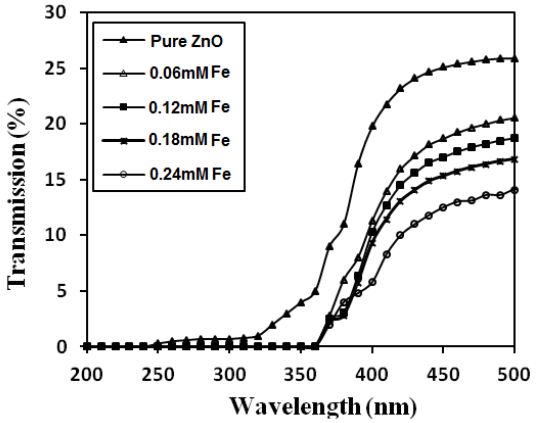

FIG. 5. Transmittance spectra of Fe-doped ZnO thin films.

It is interesting to note that for higher wavelengths (λ > 370 nm), transmission (%) is gradually reduced with Fe doping. The transmittance of Fe-ZnO films in the visible region decreases from 25% to10% as the Fe doping percentage increases. This decrease in the transmittance value of the Fe-ZnO thin films is due to the grain boundary scattering and attributed to the increased scattering of photons by crystal defects created by doping [39]. The free carrier absorption of the photons also contributes to the observed reduction in the optical transmission of heavily doped films. This decrease agrees with other workers. For example, Chen et al. [40] found that the transmittance in the visible region obviously decreased when ZnO thin films were doped with high Fe concentration, which is consistent with our observations. The transmittance curves show that for high energies (lower wavelengths) there is no transmission, because all the light is absorbed. For low energies (higher wavelengths), however, there are no appropriate electronic transitions possible, so the transmission is very high in this range. From transmittance spectra, it is observed that the Fe-ZnO samples show a decrease in the energy band gap from 3.5 eV for pure ZnO to 3.19 eV for Fe-ZnO. A blue shift in the band gap was observed in films as the doping concentration was increased. Band gaps estimated from these spectra were 3.5, 3.3, 3.2, 3.2 and 3.19 eV corresponding to the films deposited at 0.0 mM Fe, 0.06 mM Fe, 0.12 mM Fe, 0.18 mM Fe and 0.24 mM Fe, respectively.

Conclusions

Pure and Fe-ZnO thin films have been successfully synthesized on gold coated glass substrates by low-cost one-step electrodeposition technique. The ZnO film presented a pure phase and a crystal size on the nano-metric scale. From X-ray diffraction analysis, the polycrystalline ZnO with wurtzite structure and the formation of Fe-ZnO composite were also confirmed. Also, the XRD analysis showed that the Fe ions replaced Zn atoms and are incorporated into the crystal lattice positions of ZnO. The surface morphology of the Fe-ZnO thin films shows a network of flake-like nanostructures and clearly revealed that the average size of surface flakes increased with increasing the concentration of Fe doping.

The PL spectra of ZnO films illustrate that the concentration of Fe doping plays an important role in the evolution of PL properties. The intensities of defects emissions increase

with the increase of Fe concentration, resulting in the red-shift of emission centre in the PL spectra indicating that more defects were formed in Fe-ZnO doped films. The undoped ZnO thin films exhibited a pure excitonic emission centred at 382 nm, whereas the Fe-ZnO films showed a red shift in UV emission. The transmittance of Fe-ZnO films in the visible region decreases as the Fe doping percentage increases

References

[1] Savariumuthu, P.A., Jeong, I.L. and Jin, K.K., Appl. Phys. Lett., 90 (2007) 103.

[2] Saito, N., Haneda, H., Sekiguchi, T., Ohashi, N., Sakaguchi, I. and Koumoto, K., Adv. Mater., 14 (2002) 418.

[3] Ohashi, N., Kataoka, K., Ohgaki, T., Miyagi, T., Haneda, H. and Morinaga, K., Appl. Phys. Lett., 83 (2003) 4857.

[4] Abdulgafour, H.I., Yam, F.K., Hassan, Z., Al-Heuseen, K. and Jawad, M.J., J. Alloys Compd., 509 (2011) 5627.

[5] Choy, J.H., Jang, E.S., Jang, J.H. and Him, Y.W., Adv. Mater., 15 (2003) 1911.

[6] Novotny, I., Sutta, P., Mika F. and Trarozek, V., Proceedings of the International Conference on Microelectronics (IEEE Piscataway, N.J., 1995), p. 65.

[7] Mahnmood, F.S., Gould, R.D., Hassan A.K. and Salih, H.M., Thin Solid Films, 270 (1995) 376.

[8] Bonasewicz, P., Hirschwald, W. and Neumann, G., Thin Solid Films, 142 (1986) 77.

[9] Kuroyanagi, A., Jpn. J. Appl. Phys., 28 (1989) 219.

[10] Gpolaswamy, H. and Reddy, P.J., Semicond. Sci. Technol., 5 (1990) 980.

[11] Gomez, H., Maldonado, A., Asomoza, R., Zironi, E.P., Canetas-Ortega, J. and Palacios-Gomez, J., Thin Solid Films, 293 (1992) 117.

[12] Minami, T., Sato, H., Sohokara, H., Takata, S., Miyata, T. and Fukuda, I., Thin Solid Films, 253 (1994) 14.

[13] Ennaoui, A., Weber, M., Scheer, R. and Lewerenz, H.J., Sol.Energy Mater. Sol. Cells, 54 (1998) 277.

[14] Yingling, Y., Hongwei, Y., Zhengping, F., Beifang, Y., Linsheng, X., Yuandong, X., Jian, Z., Fanqing, L., Solid State Communications, 138 (2006) 521.

[15] Dalchiele, E.A., Giorgi, P., Marotti, R.E., Martin, F., Ramos- Barrado, J.R., Ayouci, R. and Leinen, D., Sol. Energy Mater. and Sol. Cells, 70 (2001) 245.

[16] Fahoume, M., Maghfoul, O., Aggour, M., Hartiti, B., Chralbi, F. and Ennaoui, A., Sol. Energy Mater. and Sol. Cells, 90 (2006) 1437.

[17] Annica, A., Nicklas, J., Per, B., Nu, Y., Donald, L. and Salaneck, W.R., Adv. Mat., 10 (1998) 859.

[18] Sharma, P.K., Dutta, R.K., Pandey, A.C., Layek, S and Verma, H.C., J. Magn. Mater., 321 (2009) 2587.

[19] Pan, F., Song, C., Liu, X.J., Yang, Y.C. and Zeng, F., Mater. Sci. Eng., R 62 (2008) 1.

[20] Van, L.H., Ding, J., Hong, M.H., Fan, Z.C. and Wang, L., Surf. Rev. Lett., 15(2008) 81.

[21] Song, C., Pan, S.N., Liu, X.J., Li, X.W., Zeng, F., Yan, W.S., He, B. and Pan, F., J. Phys.: Condens. Matter, 19 (2007) 176229.

[22] Polyakov, A.Y., Govorkov, A.V., Smirnov, N.B., Pashkova, N.V., Pearton, S.J., Ip, K., Frazier, R.M., Abernathy, C.R., Norton, D.P., Zavada, J.M. and Wilson, R.G., Mater. Sci. Semicond. Process, 7 (2004) 77.

[23] Janisch, R., Gopal, P. and Spaldin, N.A., J. Phys.: Condens. Matter, 17 (2005) R657.

[24] Debernardi, A. and Fanciulli, M., Appl. Phys. Lett., 90 (2007) 212510.

[25] Sato, K. and Katayama-Yoshida, H., Physica E, 10 (2001) 251.

[26] Wei, X.X., Song, C., Geng, K.W., Zeng, F., He, B. and Pan, F.J. Phys: Condens. Matter, 18 (2006) 7471.

[27] Karmakar, D., Mandal, S.K., Kadam, R.M., Paulose, P.L., Rajarajan, A.K., Nath, T.K., Das, A.K., Dasgupta, I. and Das, G.P., Phys. Rev. B, 75(2007) 144404.

[28] Feng, Q.J., Shen, D.Z., Zhang, J.Y., Li, B.H., Zhang, Z.Z., Lu, Y.M. and Fan., X.W., Mater. Chem. Phys., 112 (2008) 1106.

[29] Ishizaki, H., Imaizumi, M., Matsuda, S., Izaki, M. and Ito, T., Thin Solid Films, 411 (2002) 65.

[30] Hosik, P., Perla, A., Marc, A. D., Ashok, M., Heechul, C. and Nosang V. Myung. Chemical Engineering Journal, 139 (2008) 208.

[31] Chen, Z.C., Zhug, L.J., Wu, X.M. and Meng, Y.D., Thin Solid Films, 515 (2007) 5462.

[32] Panigrahy, B., Aslam, M. and Bahadur, D., J. Phys. Chem., C114 (2010) 11758.

[33] Barick, K.C., Aslam, M., Dravid, V.P. and Bahadur. D., J. Phys. Chem., C112 (2008) 15163.

[34] Krüger, J., Sudhir, G.S., Corlatan, D., Cho, Y., Kim, Y., Klockenbrink, R., Rouvimov, S., Liliental-Weber, Z., Kisielowski, C., Rubin, M. and Weber E.R., Mater. Res. Symp. Proc. 482 (1998).

[35] Wu, J.J., Wen, H.I., Tseng, C.H. and Liu, S.C., Adv. Funct. Mater., 14 (2004) 806.

[36] Chang, Y.C. and Chen, L.J., J. Phys. Chem., C111 (2007)1268.

[37] Panigrahy, B., Aslam, M. and Bahadur, D., J. Phys. Chem., C114 (2010)11758.

[38] Wang, Y., Milosevic, O., Gomez, L., Rabanal, M.E., Torralba, J.M., Yang, B. and Townsend, P.D., J. Phys. Condens. Matter, 18 (2206) 9257.

[39] Joseph, B., Manoj, P.K. and Vaidyan, V.K., Ceram. Int., 32 (2006) 487.

[40] Chen, Z.C., Zhuge, L.J., Wu, X.M. and Meng, Y.D., Thin Solid Films, 515 (2007) 5462.

Volume 7, Number 2, 2014. pp. 65-72

Jordan Journal of Physics

ARTICLE

A Computer Model for the Movement of Electrically Stimulated Paramecium

Abdul – Rahman A. Al – Rudainy

Ministry of Science and Technology, Baghdad - Iraq.

Received on: 7/1/2014; Accepted on: 18/5/2014

Abstract: In this paper, I will study some parameters that affect the motion behavior of a *Paramecium* which is exposed to stimulation by electrical pulses. This study is conducted by simulation using a two – segment electrophysiological model computer program. The goal of the simulation program is to find the relation between the intraciliary calcium concentration, $[Ca^{2+}]_i$ and the electric pulses' amplitude applied to a free swimming *Paramecium,* as well as to explore the relationship between the electric pulse amplitude and the ciliary reversal time. I have found that when the anterior segment of the model lies toward the anode before application of the electric pulses across the cell, the membrane potential of the cell will be depolarized at some electric pulses of different amplitude and duration. This depolarization causes the cilia to reverse their beating direction which makes the cell swim backward. The longest time for this reversal, about 2s, is found at the pulse of 80 mV and 0.6 ms. In contrast, the model shows that there are very small depolarization and no depolarization when the anterior segment lies toward the cathode before the electric pulses are applied.

Keywords: Computer model; Two–segment; Intraciliary calcium concentration $[Ca^{2+}]_I$.

Introduction

Paramecium is a unicellular micro-organism with a slipper – like shape. Its membranes are covered with tiny hair – like projections called cilia. This organism swims in a spiral path on its long axis due to beating the cilia. It swims forward when the cilia beat at angle backwards in unison, while it swims backward when the cilia reverse their beat (i.e., beating forward).

Many computer models were constructed for studying motile responses of cilia and flagella due to different stimulations [5–15]. A computer model was designed for simulation to study the responses of swimming *Paramecium* due to electric field (galvanotaxis) [16, 17]. Chemotactic behavior (Chemotaxis) of the *Paramecium* was also simulated by a computer model [18]. The effect of gravity on the *Paramecium* movement (gravitaxis) [19] and ciliate cell responses such as *Fabra salina* to light (Phototactic-behavior or Phototaxis-) had been studied by a computer model [20]. Other models simulated *Paramecium's* swimming orientation due to magnetic field (magnetotaxis) [21]. A considerable amount of information is now available on ionic relations and gating processes in *Paramecium*. Hook and Hildebrand's physiological model [2, 3] accounts well for available electrophysiological data on clamped cells and for variable ciliary reversing time which is observed when ionic concentrations in the medium are changed. A theoretical electrophysiological two – segment model for *Paramecium* based on Hook and Hildebrand's model is constructed to give an explanation to experimental results of freely – swimming *Paramecia* behavior when they are excited by electric pulses [1, 4]. Analysis of the experimental results [4] shows that the reverse swimming (backward swimming) due to external

Corresponding Author: Abdul – Rahman A. Al – Rudainy **Email**: asaoat@yahoo.com

electric field pulses applied across a trough containing a free swimming *Paramecia* occurs among those cells which are swimming forward toward the anode (i.e., cell's anterior toward the anode) before the electric pulses are applied. In contrast, those cells swimming toward the cathode before the application of pulses generally increase their forward swimming velocity afterwards. It is found that there is a direct proportional relationship between the percentage increase or decrease in forward swimming velocity of the cells after the pulse and the initial (pre-pulse) swimming velocity [4]. In this paper, the simulation of a two-segment model is done to see if there is an effect of intraciliary calcium concentration and the membrane potential on the swimming of the *Paramecium.*

Computer Simulation

The two-segment model computer program was run on a computer for an extended period, sometimes for two days, to enable the steady-state (unexcited) parameters to be determined. In the steady-state, the intraciliary calcium concentration for both cell segments (interior and posterior of the cell) and the cytoplasmic calcium concentration are both about 26 n.mol. dm^{-3}. The intraciliary calcium concentration required to initiate ciliary reversal in the two-segment model is chosen to be 500 n.mol.dm^{-3}. Table 1 shows some parameters which are used in the two – segment model. Other models' parameters are the same as shown in previous work [1].

TABLE 1. Some of the parameters used in the two – segments model

Parameter	Symbol	Value
Ca^{2+} - conductivity per cilium	g_{Ca}	3.75×10^{5} 1 / mV. s
K^{+} - conductivity per cilium	g_{K}	2.5×10^{8} 1 / mV. s
Intracellular Ca^{2+} - concentration	$[Ca^{2+}]_i$	10 nmol. dm^{-3}
Intracellular K^{+} - concentration	$[K^{+}]_i$	20×10^{6} nmol. dm^{-3}
Extracellular Ca^{2+} - concentration	$[Ca^{2+}]_o$	10 nmol. dm^{-3}
Extracellular K^{+} - concentration	$[K^{+}]_o$	2×10^{6} nmol. dm^{-3}
Steady – state membrane potential	V_m	- 30 mV
Overall membrane capacitance of the cell body	C	10.4×10^{-13} C / mV
Number of cilia	N	10^{4}
Volume of cilia	Δ_i	3×10^{-13} cm^{-3}
Effective volume of the cell body	Δ_c	10^{-5} cm^{-3}

Anterior Segment toward Anode before the Application of Electric Pulses

The two-segment asymmetric model predicts a reverse in cell swimming (backward swimming) after applying an electric pulse when the anterior segment faces the anode before the pulse. For pulses of a duration of 0.6 ms and varying amplitude, the simulation of the two – segment model shows that the membrane potential is depolarized (above 0mV) within 20-250 ms according to the amplitude of the pulse (FIG.1); then the membrane potential sharply drops around - 30 mV; i.e., the steady – state value.

The maximum value of membrane potential depolarization for each pulse increases as the pulse amplitude increases until it reaches a maximum peak at a pulse of 80 mV, then decreases for further increases in pulse amplitude (FIG.2).

The average intraciliary calcium concentration, $[Ca^{2+}]_{i.ave.}$, of both segments following a pulse amplitude of 80 mV and duration of 0.6 ms, remains on the plateau of about $6x10^{-5}$ mol. dm^{-3} for about 1.5s, then drops to around $6x10^{-6}$ mol. dm^{-6} and remains at this level for more than 20s without showing any indication of returning to the original steady level, while at 65 mV and 100 mV for 0.6 ms $[Ca^{2+}]_I$ shoos within a very short time to peak, then drops sharply to steady state level (FIG.3).

The maximum value of $[Ca^{2+}]_{i.ave}$ for different pulse amplitudes increases with increasing amplitude until it reaches maximum, then decreases with further increase in pulse amplitude (FIG.4). These findings suggest that the pulse of 80 mV and 0.6 ms has strong effects on the depolarization of the membrane potential and increase in intraciliary calcium concentration; hence, the cell will undergo a

longer ciliary reversal time than for other pulses. Cytoplasmic calcium concentration, $[Ca^{2+}]_c$, builds up to a maximum plateau due to a pulse (FIG.5) and remains at this level for a long time before returning to the steady – state level. This may be caused by slow diffusion process of Ca^{2+} ions from cytoplasm to cilia. The peak of $[Ca^{2+}]$ increases as the strength of the pulse increases until it reaches a maximum (peak) value of about $6x10^{-6}$ mol.dm^{-3} at a pulse of 80 mV and 0.6 ms and then decreases with further increase in pulse strength until reaching 0 mV (FIG.6).

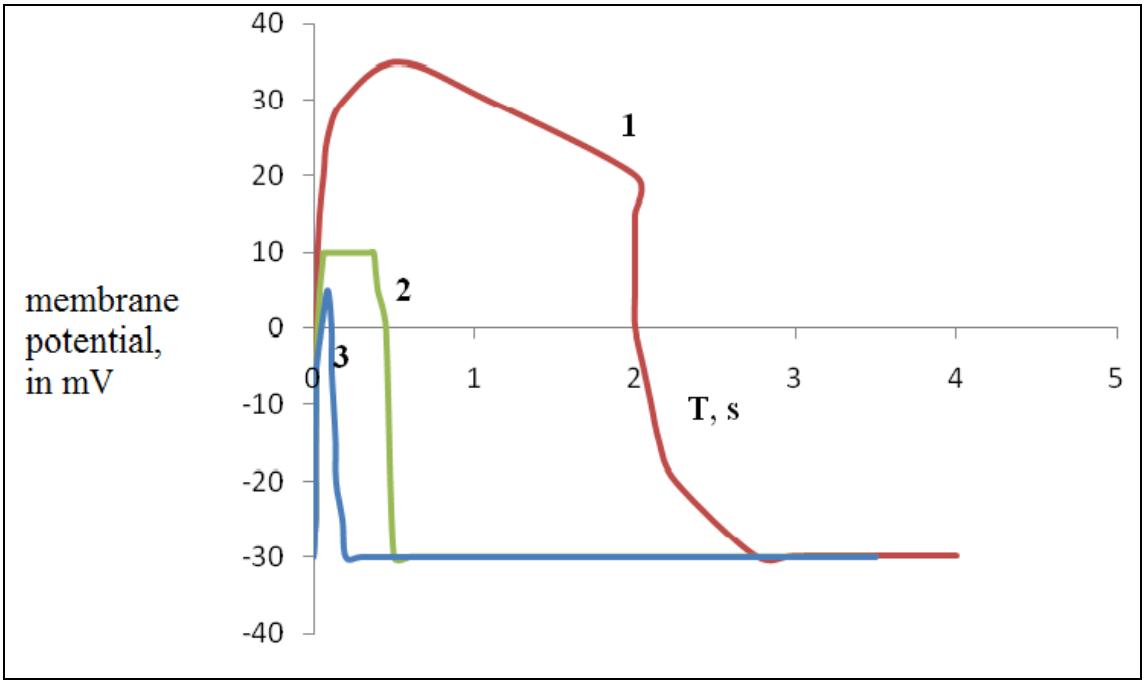

FIG. 1. Computed change in membrane potential in response to electric pulses. T is the time in seconds for depolarization of membrane potential (i.e., above 0 mV) and returning to steady – state level – 30 mV. a- Curve 1 is for a pulse of 80 mV and 0.6 ms. b – Curve 2 is for a pulse of 100 mV and 0.6 ms. c- Curve 3 is for a pulse of 65 mv and 0.6 ms

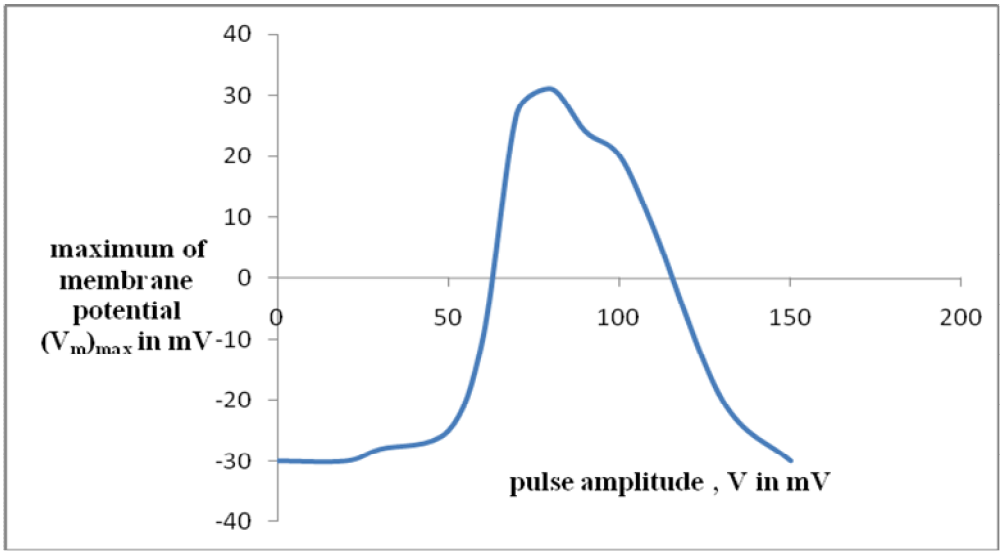

FIG. 2. Computed relationship between maximum membrane potential, $(V_m)_{max}$, in mV and pulse amplitude, V, in mV

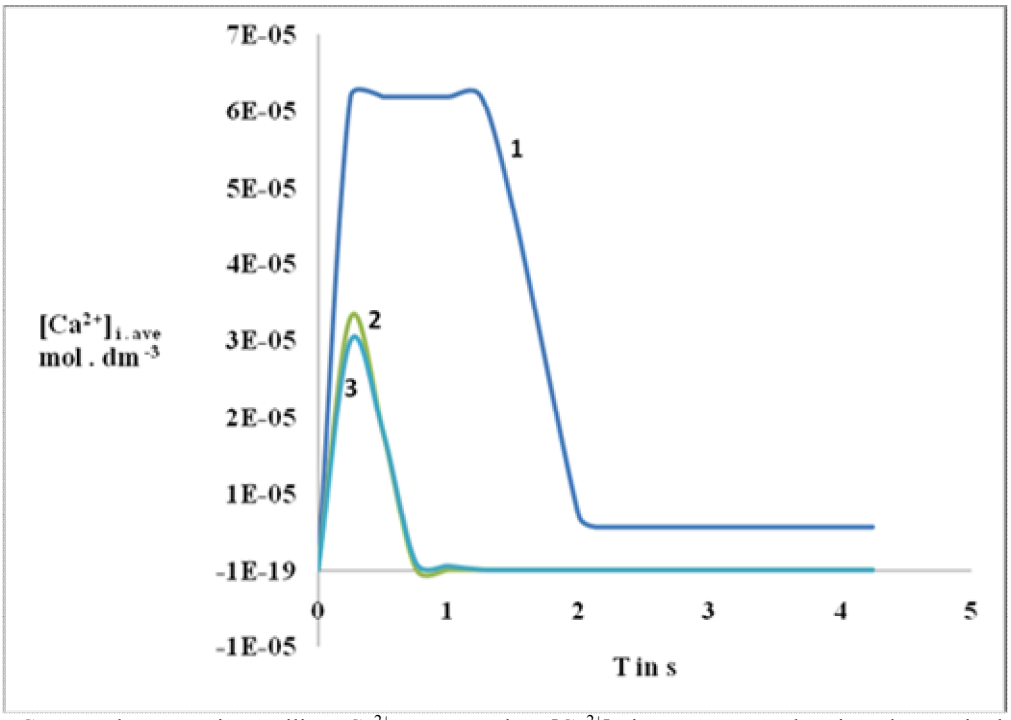

FIG. 3. Computed average interaciliary Ca^{2+} concentration, $[Ca^{2+}]_i$, in response to electric pulses. T is the time lasting for increasing Ca^{2+} within cilia and then returning to steady – state level. a – Curve 1 is for a pulse of 80 mV and 0.6 ms, b – Curve 2 is for a pulse of 100 mV and 0.6 ms, and c – Curve 3 is for a pulse of 65 mV and 0.6 ms

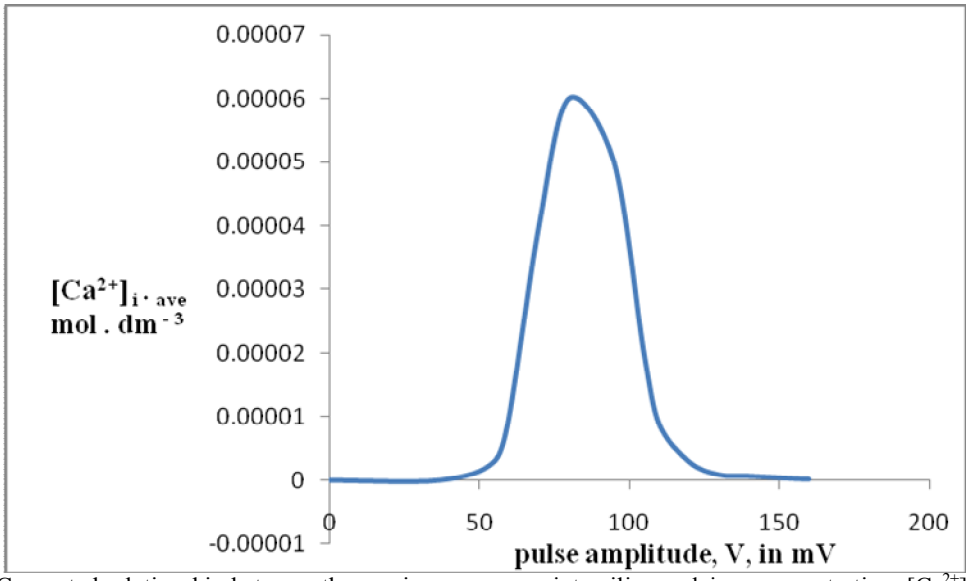

FIG. 4. Computed relationship between the maximum average intraciliray calcium concentration, $[Ca^{2+}]_{i.ave.}$, and the pulse amplitude,V

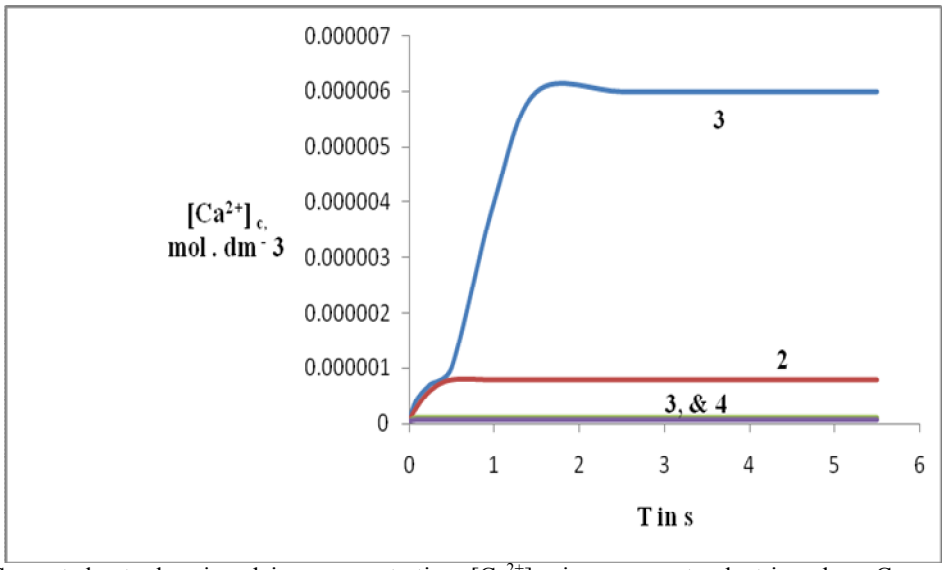

FIG. 5. Computed cytoplasmic calcium concentration, $[Ca^{2+}]_c$, in response to electric pulses. Curve 1 is for a pulse of 80 mV and 0.6 ms, Curve 2 is for a pulse of 100 mV and 0.6 ms, and Curves 3and4 coincide with each other because there are very little differences between their values. Curve 3 is for a pulse of 65 mV and 0.6 ms, and curve 4 is for a pulse of 130 mV and 0.6 ms. T is the time for $[Ca^{2+}]_c$ level in the cell due to a different pulses

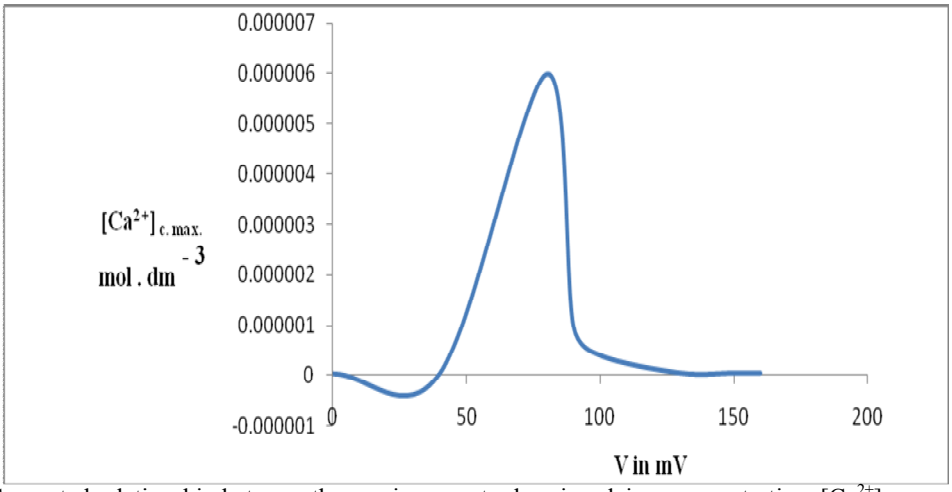

FIG. 6. Computed relationship between the maximum cytoplasmic calcium concentration, $[Ca^{2+}]_{c.\,max.}$, and pulse amplitude, V

Table 2 shows the relationship between pulses of varying amplitude and duration, and ciliary reversal time ($T_{s.r.;}$ i.e., the time during which the cilia beat forward opposite to normal backward beating).

The table was analyzed in the direction of fixed pulse duration (τ) and varying pulse amplitude (V). When τ is 0.2 and 0.4 ms, there is no reversal and very weak reversal, respectively.

H represents a ciliary reversal time, T_{cr}, greater than 20s, τ is the pulse duration in ms, and V is the pulse amplitude in mV.

At further increase in τ, the ciliary reversal time ($T_{cr.}$) reaches the maximum value immediately after the threshold where it remains on a plateau as long as the pulse amplitude increases. The plateau represents a long $T_{cr.}$of more than 20 s, as the cell needs more time to resume its forward swimming (i.e., the cilia return to normal beating) by pumping out the calcium to reach a level below $5x10^{-7}$ $mol.dm^{-3}$

(the suggested amount of $[Ca^{2+}]_i$ which causes a ciliary reversal). As the pulse amplitude (strength) increases further, the duration of ciliary reversal falls very sharply.

TABLE 2. Computed effects of varying duration and amplitude on the duration of ciliary reversal time, T_{cr}, in ms

V in mV	τ in ms 0.2	0.4	0.6	0.8	1.0	1.2
40	0	0	0	10	25	33
60	0	20	30	H	H	H
70	0	25	H	H	H	H
80	0	25	H	H	H	H
90	0	20	H	H	H	H
100	0	15	450	H	H	H
110	0	13	30	H	H	H
120	0	13	25	30	45	H
150	0	12	13	16	19	21

The Anterior Segment Facing the Cathode before the Application of Electric Pulses

We find that both the membrane potential, and the average intraciliary calcium concentration, $[Ca^{2+}]_{i.ave.}$, are responding very weakly to different pulses when the anterior segment lies toward the cathode before the electric pulses are applied. The overall membrane is depolarized very little and for a short time (about 20 ms) due to a pulse of 80 mV and 1.2 ms, whereas a pulse of 100 mV and 1.2 ms causes a slight hyperpolarization before returning to steady – state level of -30 mV (FIG. 7).

$[Ca^{2+}]_{i.ave.}$ increases above 5 x 10^{-7} mol. dm^{-3} for about the 20 ms following the pulse of 80 mV and 0.6 ms, and then drops sharply to the steady – state level of about 3.5 x 10^{-8} mol. dm^3, whereas a pulse of 100 mV and 0.6 ms causes no effect on the steady –state level of $[Ca^{2+}]_{i.ave.}$ (FIG. 8).

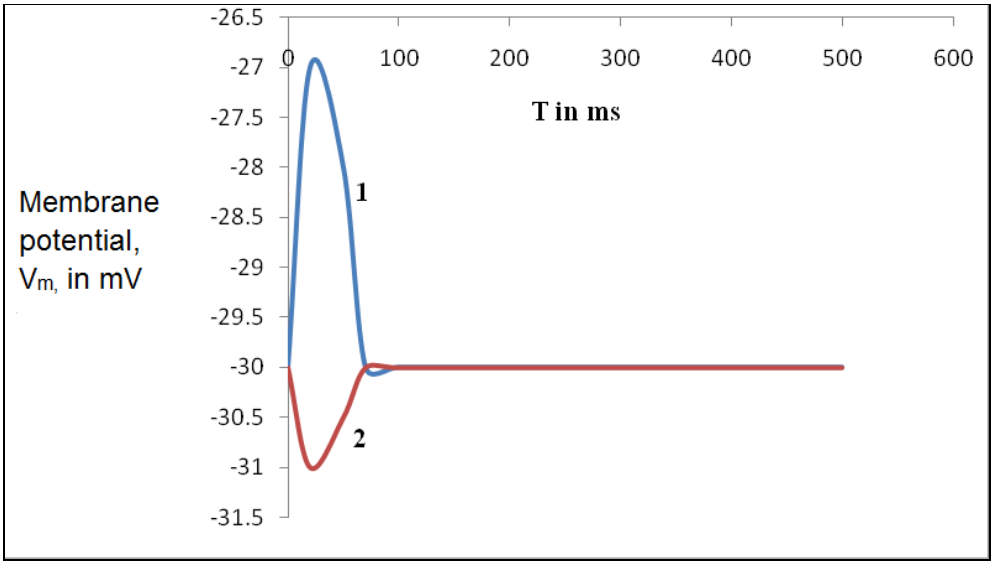

FIG. 7. Computed membrane potential responses to electric pulses when the anterior segment lies toward the cathode during the pulse. Curve 1 is for a pulse of 80 mV and 0.6 ms, and curve 2 is for a pulse of 100 mV and 0.6 ms. T is the time of membrane potential response in ms.

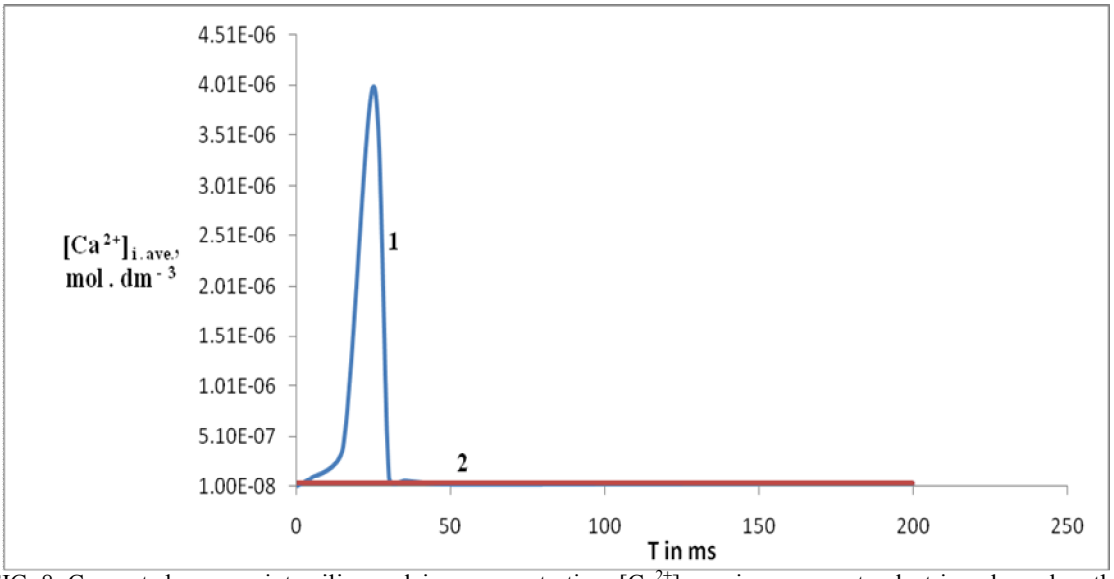

FIG. 8. Computed average intraciliray calcium concentration, $[Ca^{2+}]_{i\,ave.}$, in response to electric pulse, when the anterior segment lies toward the cathode during the pulse. Curve 1 is for a pulse of 80 mV and 0.6 ms, and curve 2 is for a pulse of 100 mv and 0.6 ms. T is the time of $[Ca^{2+}]_{i.ave.}$ after the application the electric pulses.

Discussion

The two – segment model is designed to simulate the reversal movement of the cilia on the anterior part of the *Paramecium* facing the anode before the application of electric pulses. This simulation is done by an uneven distribution for Ca^{2+} and K^{+} channels over the cell body. The ionic channel asymmetry (Ca^{2+} and K^{+} channels) implies that the posterior segment of the model plays the more important role in controlling ciliary reversal, because the majority of the Ca^{2+} - channels are assumed to be located there. According to the two – segment model, the cell is considered to be in a fully reversed state (i.e., the cilia beat toward the cell's anterior) as long as $[Ca^{2+}]_{i.\,ave.}$ – level in both segments is above 5×10^{2} n.ml. dm^{-3}.

The experimental observation that the *Paramecia* resume their forward swimming after a period of reverse swimming [4] is successfully interpreted by the two – segment model. The argument on this can be put as follows: As the level of the intraciliary calcium concentration, $[Ca^{2+}]_i$, falls below 5×10^{2} n.mol.dm^{-3} (the minimal level for initiating reversal), and the membrane potential repolarizes the steady – state level of -30 mV (FIG. 1 and FIG. 3), the cilia start beating in the normal direction (i.e., toward the posterior end), and cause the cell to swim forward. The cell reversal due to electric field pulses must be caused by perturbation of the membrane potential (depolarization) which then leads to an increase in calcium conductance, $g_{Ca,}$ and thereby allows more Ca^{2+} - ions rush into the cell. As a consequence, the intraciliary calcium concentration, $[Ca^{2+}]$, increases causing a ciliary reversal [22]. This sequence, leading to ciliary reversal, can be explained by comparing the membrane potential and $[Ca^{2+}]_{i.\,ave.}$ – level responses (FIG. 1 and FIG. 2). It is noticeable how these two responses have similarity in their shapes which implies that as the membrane depolarizes, $[Ca^{2+}]_i$ increases.

The two – segment model simulation shows that ciliary reversal time attains a plateau due to pulses of varying duration and amplitude (TABLE 2), which is in agreement with experimental results [4]. This may be interpreted as follows: For each pulse duration, there is an optimum pulse amplitude each one of which causes the same ciliary reversal time. This result can be used to explain the plateau which is formed by the percentage of cells reversing due to electric pulses of varying duration and amplitude [4].

The analysis of TABLE 2 in the direction of varying pulse in ciliary reversal time shows that there is no decrease in the ciliary reversal time following the plateau for further increase in pulse duration, because the intraciliary calcium

concentration, $[Ca^{2+}]_i$, in both segments remains above $5x10^2$ n.mol.dm^{-3} (FIG.5). In contrast, the experimental results show the existence of a decrease in ciliary reversal time as the pulse duration is increased further [4]. Analyzing TABLE 2 in the direction of varying amplitude and fixed duration of pulse shows the existence of a decrease in reversal time as the pulse amplitude increases, which agrees with experimental results.

References

[1] Al-Rudainy, A.A., Jordan Journal of Physics (JJP), 4(1) (2011) 43.

[2] Hook, C. and Hildebrand, E., J. Math. Biol., 8 (1979) 197.

[3] Hook, C. and Hildebrand, E., J. Math. Biol., 9 (1980) 347.

[4] Al-Rudainy, A.A., Dirasat Journal, University of Jordan, 36(2) (2009) 115.

[5] Sakane, A. et al., 2001 Nippon Kikai Gakkai Robotikusu, Mekatoronikusu Koenkai Koen Ronbunshu, 2001(Pt.5) (2001) 2P2.B9(1)-2P2.B9(2).

[6] Binge, V.N. et al., Biofizika, 49(4) (2004) 705–9.

[7] Bogacheva, N.V. and Deev, A.L., Biofizika, 47(1) (2002) 94 - 99.

[8] Hirano, A., Tsuji, T., Takiguchi, N. and Ohtake, H., Trans. of SICE, 41(4) (2005) 351 (in Japanese).

[9] Hirano, A., Tsuji, T., Takiguchi, N. and Ohtake, H., Trans. of SICE, 42(11) (2006) 1252 (in Japanese).

[10] Lisa, F.J. and Robert, D., Annu. Rev. Fluid Mech., 38 (2006) 371.

[11] Pedley, T.J. and Kessler, J.O., Annu. Rev. Mech., 24 (1992) 313.

[12] Gerasim, K.V. and Vladimir, T.P., Acta Bioengineering and Biomechanics, 13 (2011) 73.

[13] Hirano, A., Tsuji, T., Takiguchi, N. and Ohtake, H., Transactions of the Japan Society of Mechanical Engineering Series C; ISSN: 0387 – 5024, 73(734) (2007) 2757.

[14] Gueron, S. and Levit–Gurevich, K., Biophys. J., 74(4) (1998) 1658.

[15] Hirano, A., Soh, Z.U., Tsuji, T., Takiguchi, N. and Ohtake, H., The Thirteenth International Symposium on Artificial Life and Robotics, Japan (AROB 13th 08), B – Con Plaza, Beppu, Oita, January 31 – February 2 (2008).

[16] Ogawa, N., Oku, H., Hashimoto, K. and Ishikawa, M., Bio-mechanisms of Swimming an Flying, Springer, Japan, (2008) P. 29.

[17] Ogawa, N., Oku, H., Hashimoto, K. and Ishikawa, M., Journal of Theoretical Biology, 242 (2006) 314.

[18] Hirano, A., Tsuji, T., Takiguchi, N. and Ohtake, H., Systems, Man and Cybernetics, 2006. SMC'06. IEEE International Conference, Vol.5, (2006).

[19] Mogami, Y. and Baba, S.A., Adv. Space Res., 21(8–9) (1998) 291.

[20] Karine, G. and James, V.M.V.J., Biophysical Journal, 90(8) (2006) 3004.

[21] Roberto, M., Gianfranco, P. and Giuliano, C., Journal of Photochemistry and Photobiology B: Biology, 54(2–3) (2000) 18.

[22] Eckert, R., Science, 176 (1972) 473.

Volume 7, Number 2, 2014. pp. 73-83

Jordan Journal of Physics

ARTICLE

Particle Size Distributions Inside a University Office in Amman, Jordan

Tareq Hussein

Department of Physics, The University of Jordan, Amman 11942, Jordan.
Department of Physics, University of Helsinki, P. O. Box 48, FI-00014 UHEL, Helsinki, Finland.

Received on: 3/3/2014; Accepted on: 18/5/2014

Abstract: We studied the number based particle size distribution (diameter 0.3–10 μm with high time-resolution) inside an office (naturally ventilated) at a university building in Jordan during two weeks (18.09.2013 – 01.10.2013). We analyzed and investigated the particle number and mass concentrations, their differences between workdays and weekends and the effect of tobacco smoke and worker activities inside the office. We also focused on three scenarios of office conditions: totally closed, totally open and open window. The 24-hour means of the $PM_{10-0.3}$ were 16.4–43.2 μg/m^3 on workdays and 4.4–8.5 μg/m^3 on weekends. The concentrations ranged from 4.3 μg/m^3 to 7.7 μg/m^3 (30.0–42.1 cm^{-3}) when the office was kept closed at nighttime and weekends. They also ranged from 5.2 μg/m^3 to 25.8 μg/m^3 (50.0–83.2 cm^{-3}) when the window was open at night. The highest concentration ranged from 2.5 μg/m^3 to 261.9 μg/m^3 (15.5–906.4 cm^{-3}) during the daytime on workdays when the office was open. The variation of aerosol concentrations is believed to be caused by increased urban activities on daytime and workdays, enhanced ventilation rate and penetration factor when the office was open, and the resuspension of carpet-dust by the office occupants and visitors. Smoking inside the office increased the aerosol concentration to 3729.2 μg/m^3 (4854.5 cm^{-3}) and the tobacco smoke remained sensible inside the office for more than 40 minutes. Since the mass concentrations presented here were calculated by assuming spherical particles and unit density and the measured size-range was larger than 300 nm in diameter, the PM_{10} is expected to be at least double the numbers shown in this study, and thus the 24-hour PM_{10} in the office would exceed the maximum value recommended by the WHO guidelines, which is not to exceed 50 μg/m^3 for more than 35 days per year.

Keywords: Indoor air quality; Particulate matter; Re-suspension; Natural ventilation; University building.

Introduction

According to activity diary studies, offices and workplaces are the second indoor environments where people spend most of their time [1]. Therefore, work places ought to be comfortable, because workers' performance and health are affected by thermal discomfort and poor air quality inside their offices [2]. For example, a worker's task performance decreases when he feels hot. Feeling hot at office might increase the worker's heart rate, respiratory ventilation and end-tidal partial pressure of carbon dioxide; and on the other hand, his/her arterial oxygen saturation decreases [2]. Besides environmental factors, symptoms in office workers can be also associated with psychosocial stress or even poor psychosocial conditions [3–4].

Beside the outdoor air as the main source of aerosol particles inside offices, these are produced during operation of office appliances

Corresponding Author: Tareq Hussein **Email**: T.hussein@ju.edu.jo

such as printers [5–6]. Re-suspension can be also a significant source when occupants move intensively [7–10]. Smoking is another potential source of indoor aerosols when individuals violate smoking prohibition inside offices and public buildings. Slezakova et al. [11] confirmed that tobacco smoking significantly influences the composition of fine particles, and the particulate mass concentrations of five carcinogenic elements (Cr, Ni, As, Cd and Pb) were increased by one to three orders of magnitude. They also reported that S, K and Zn were predominantly present in the fine fraction and associated with tobacco smoking.

Recently, the Indoor Air Quality (IAQ) at workplace has been given increased attention. For instance, Fisk et al. [12] found out a large rate of submicron particles removal and a significant source/resuspension of micron particles inside mechanically ventilated office. Zuraimi and Tham [13] quantified the efficiency of dry-media and electrostatic precipitation filters used in mechanically ventilated offices; they reported that electrostatic precipitation filters are superior to media filters in removing fine particles with aerodynamic diameters >300 nm. Smolík et al. [14] evaluated fine and coarse particle deposition inside a naturally ventilated office. Among the main electrical machines used in offices, printers and photocopiers generate fine particles with high amounts that exceed several orders of magnitude what can be found in normal conditions [4–5, 15–16]. Hussein et al. [17–19] analyzed and modeled the fine particle number concentrations and size distributions inside mechanically ventilated offices; they showed that during the absence of indoor sources the indoor-to-outdoor relationship of fine aerosol particles is affected by three main parameters: ventilation, deposition and penetration. Quang et al. [20] also reported that $PM_{2.5}$ and number concentrations of particles smaller than 3 μm in diameter inside three mechanically ventilated urban offices are mainly from outdoor origin and that the ventilation and penetration are main factors controlling their transport from the outdoor air into the indoor air.

Industrially synthesized nanoparticles hold a big risk on workers [21–22], and therefore, Koivisto et al. [23] presented a concept to estimate the inhaled dose of industrially synthesized nanoparticles at workplace. Zitnik et al. [24] quantified the elemental composition of PM_{10} at a medium-sized mechanical workshop and a chemistry laboratory dealing with processing advanced nano-particulate materials; they recommended an hourly time-resolution to be used for elemental analysis because 24-hours is too coarse and high-time resolution contains large variability.

With respect to educational buildings and exposure of teachers and students, Buonanno et al. [8] and Branis and Safranek [9] showed that the dominant source of the coarse fraction inside school gyms is particle re-suspension due to exercising activities by pupils. Gaidajis and Angelakoglou [25] showed that PM_{10} and $PM_{2.5}$ concentrations were significantly higher in the open access meeting place of common use as a result of student trespassing and occasional smoking. Salma et al. [26] identified two classes of coarse particles inside university buildings: general indoor dust particles with a residence time ~35 min and chalk particles with a residence time more than 20 min. Tran et al. [27] reported that elemental analysis of PM_{10} in French classrooms is increased during children's activities, but the elemental distribution was unaltered.

However, the number of investigations regarding the indoor air quality (IAQ) at work place is still very small when compared to other indoor environments such as houses and apartments. Also, the focus of previous studies has been very sparse. Beside that, measurements of particle size distributions inside offices are very few and need more attention. Furthermore, measurements of aerosols and their size distributions have never been reported in Jordan. In this study, we aim at investigating the particle size distributions inside a naturally ventilated office in a university campus in Jordan. We measured particle number size distributions (diameter between 0.3–10 μm and 1 minute time-resolution) during two weeks in autumn 2013. We analyzed the particle number and mass concentration differences between workdays and weekends and the effect of tobacco smoke and worker activities inside the office. We also focused on three scenarios of office conditions: totally closed, totally open and open window. We utilized a simple indoor aerosol model to estimate the ventilation rate of the office. According to our knowledge, this is the first study of its own to be presented for the scientific community.

Materials and Methods

Measurement Location

The measurement campaign was performed during the autumn (18.09. – 01.10.2013) inside an office in the building of the Faculty of Science at the University of Jordan, Amman. The dimensions of the office are 3m×6m×3m. The whole building was naturally ventilated via the main gate and windows. The office was furnished with a desk, a working chair, a PC table, four chairs, a middle and two side coffee tables, a folder metal-cabin, a safe, shelves, window curtains and a carpet which covered the whole floor. The office was located on the south-western corner of the building. The southern and western walls of the office contained large windows to allow air exchange with the ambient air.

The building itself was a two storey construction situated at the middle of the university campus, which is located in a suburban area at about 15 km north-west the city center. The surrounding is a residential area mixed with an urban forest and main streets. The main entrance was in the middle of the first storey facing the west and leads to the stairs way that divided the building into two unequal halves.

Aerosol Measurements and Data Handling

We measured the number size distributions of particles between 300 nm and 10 μm in diameter with an Optical Particle Sizer (OPS 3330, TSI). The instrument was calibrated by the manufacturer two months prior to the start of the measurement campaign. The OPS measurement is based on the optical diameter of the aerosol particle. The instrument also records the ambient temperature and pressure. We setup the OPS to operate in "TSI default" mode and the dead-time correction was performed throughout the measurement campaign. The sampling was carried out directly without using additional tubing at a height of about 1.3 m from the ground. Sampling time-resolution was set to 1 minute and sampling flow rate was 1 L/min.

The particle number size distributions were routinely checked for quality assurance. 100% of the measured data was valid and processed further to be prepared for data analysis. We calculated the 5-minute average and illustrated the data with 30-minute average. We also calculated average concentrations during longer time periods such as daytime or nighttime.

In order to attain an indication of the PM concentration level inside the office, we generated the number size distributions into mass size distributions by assuming spherical particles with unit density.

Office Occupancy and Scenarios

The office was occupied by the worker during the working hours between 08:00 and 17:00. It was very seldom when there were visitors or students in the office. During working hours, the main door of the building as well as the office window and door were all opened. Although the main door and all offices in the building were totally closed outside the working hours, we believe that the building was leaking air across the window shells. In order to investigate a different condition, we left the office's window opened during the last three days of the measurement campaign; i.e. after 29.09.2013 for which we shall refer to as Period II and we shall denote Period I for the time period before that.

Even though smoking was not allowed inside the building, workers/visitors often smoked in other offices in the same floor. We also wanted to test the effect of smoking inside the office by performing a smoking event (three cigarettes during 10 minutes) by two persons on 26.09.2013. Another smoking event was performed with a single cigarette by a visitor on 19.09.2013.

Ventilation Rate Quantification

According to a previous model investigation for the indoor air by Molgaard et al. [28], it was evident that the ventilation rate can be quantified by considering the variation in the number concentration of aerosol particles within the diameter range 0.1–1.0 μm emitted indoors and causing significantly high concentrations. This condition was valid during the smoking event on 26.09.2013, when the building and the office were opened. It was also possible to estimate the ventilation rate when the office was totally closed on 24.09.2013 right after leaving the office.

The approach of the ventilation rate estimation was previously described in details elsewhere [29]. The principle is based on the fact that aerosol particles within the diameter range 0.1–1.0 μm have the lowest deposition velocity; and thus, they remain airborne for a long time.

Assuming that the indoor air is well mixed, the indoor particle concentration of a certain particle size follows the mass-balance equation:

$$\frac{d}{dt} I_i = P_i \lambda O_i - (\lambda + \lambda_{d,i}) I_i \quad (1)$$

where I_i and O_i [μg/m^3 or cm^{-3}] are the indoor and outdoor particle concentrations, respectively; P [--] is the penetration factor of aerosol particles into the office, λ [h^{-1}] is the ventilation rate and λ_d [h^{-1}] is the deposition rate of aerosol particles onto available indoor surfaces. According to the model application requirement, additional terms can be added to the right side of the equation to denote for the change rate due to other processes such as emissions, re-suspension, coagulation… etc. Here, the subscript i denotes that the equation is applied for a certain particle size-range having the same physical properties and dynamic behavior.

Assuming further that the outdoor particle concentration remains rather constant as well as the parameters P, λ and λ_d that define the indoor-to-outdoor relationship of aerosol particles, then a simple mathematical solution can be found for this mass-balance equation [30–31]:

$$I_i(t) = \frac{P_i \lambda O_i}{\lambda + \lambda_{d,i}} + \left[I_i(t_0) - \frac{P_i \lambda O_i}{\lambda + \lambda_{d,i}} \right] \cdot e^{-(\lambda + \lambda_{d,i})t} \quad (2)$$

where t [h] is time and $I_i(t_0)$ is the initial particle concentration at time t_0.

Generating a large amount of indoor aerosols (e.g. a smoking event) that increases their concentrations to values higher than those found outdoors can simplify this solution and allow for an estimation for the combined term ventilation rate and deposition rate:

$$\ln\left(\frac{I_i(t_0)}{I_i(t)} \right) = (\lambda + \lambda_{d,i}) t \ . \quad (3)$$

Therefore, the ventilation rate (λ) can be calculated by using Eq. 3 as the best-fit line to the variation of the particle number concentration within the diameter range 0.1–1.0 μm, which has a small deposition rate compared to the ventilation rate (i.e. $\lambda_\delta << \lambda$), right after an indoor source that generated the high concentrations of indoor particles with the initial condition at t_0 assigned at a time after turning off the indoor source. We have to keep in mind that the time period used to fit Eq. 3 requires one more assumption stating that we can neglect the change rate due to coagulation and other processes [32].

Results and Discussion

Indoor Ambient Conditions and Office Ventilation

Air temperature inside the office varied between 33.5 and 41 Celsius degrees. It showed a clear daily pattern with maxima in the afternoon and minima in the morning (FIG. 1e). That was mainly because the office orientation with respect to the sun; it is located in the south-western corner of the building. The ambient pressure varied between 90.1 and 90.9 kPa and also showed a clear daily pattern with two peaks: one around noon and one around midnight.

According to Eq. 3, the ventilation rate estimation (λ) requires an indoor source of aerosol particles that produces significantly high concentrations within a certain time. Once the source is terminated, it is possible to follow the concentration decay of particles within the diameter range 0.1–1.0 μm. This condition was satisfied during and after the smoking event that occurred during the working hours on 26.09.2013. This yields an estimated ventilation rate ~2 h^{-1} during the open office conditions.

We also checked the measured data and the marked information in the log-book looking for other situations that are valid to apply Eq. 3. We figured out that on Tuesday 24.09.2013 around 16:00 there were several persons in the nearby office smoking heavily causing an increase in the concentrations inside the office, where the measurement was performed. After closing the office (around 16:30), the concentrations inside the office started to decay; and from this situation we estimated the ventilation rate λ ~0.5 h^{-1} for the closed office condition.

According to these estimates, the ventilation rate would vary between 0.5 and 2 h^{-1} with low ventilation during the closed office situations and high values during the open office situations. These values compare rather well with available estimates for natural ventilation inside offices and dwellings [30–31].

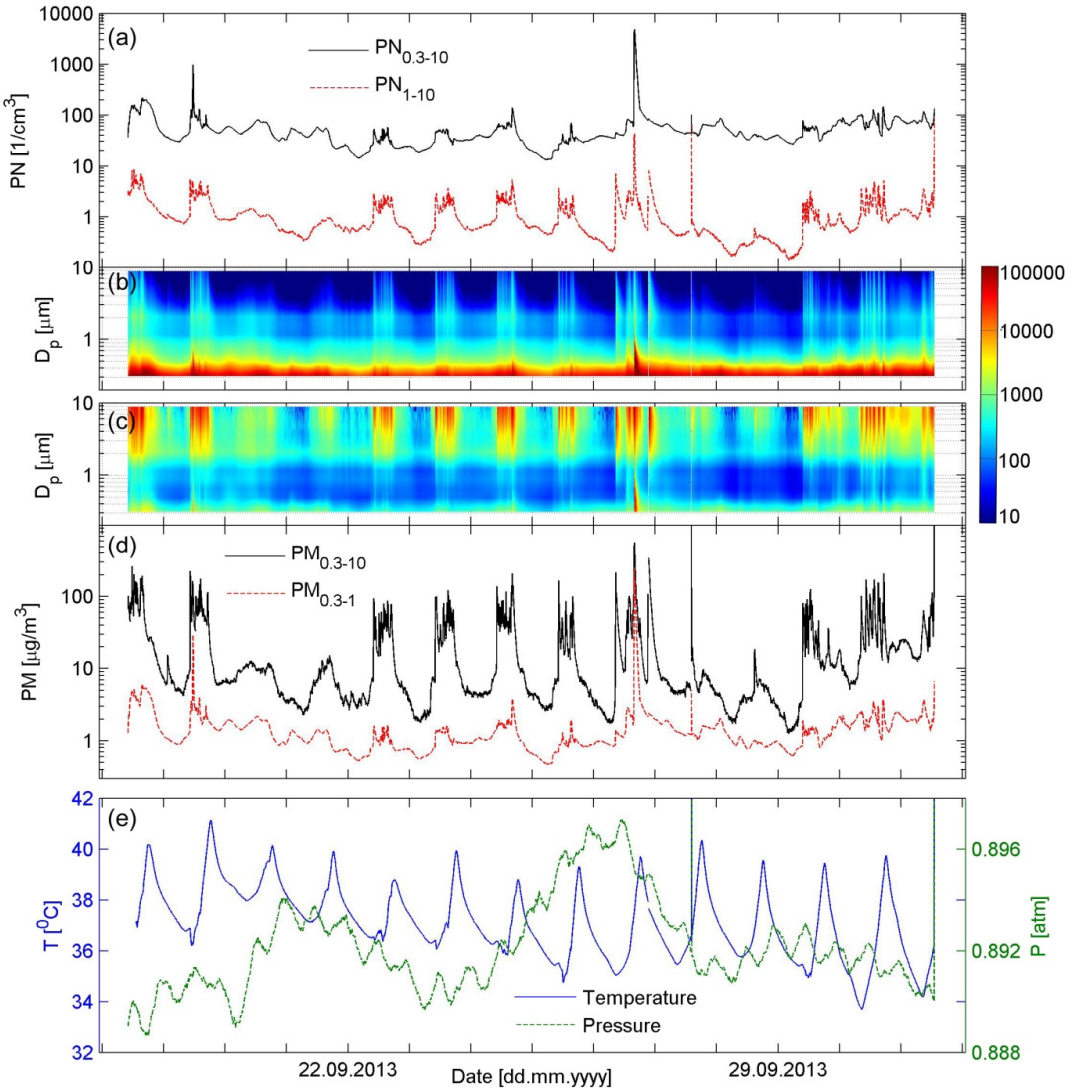

FIG. 1. Time series based on the 5-minute average: (a) integrated particle number concentrations, (b) particle number size distribution spectrum, (c) particle mass size distribution spectrum, (d) integrated particle mass concentrations and (e) indoor temperature and pressure

Average Concentrations and Size Distributions

The measured particle number size distributions and the calculated particle mass size distributions are presented in FIG. 1b and 1c, respectively. As mentioned in the methods section, we calculated the mass concentrations by assuming spherical particles and unit particle density. According to the measurement scenarios, the office (also the whole building) was open in the daytime (working hours) on workdays. The office was totally closed at night before 29.09.2013 and after that we left the window open overnight. These would be three different scenarios as: (1) totally closed office during weekends and nighttime, (2) open window at nighttime after 29.09.2013 and (3) open office during daytime on workdays. We considered daytime hours as 08:00 – 18:00, and nighttime hours starting from 22:00 and ending at 06:00 on the next morning.

During the weekends (totally closed office), the $PM_{10-0.3}$ inside the office was on average 5.7±2.9 µg/m^3 (37.0±13.3 cm^{-3}), and ranging between 1.3–15.2 µg/m^3 (12.1–74.3 cm^{-3}) with values higher than 2.5 µg/m^3 (20.9 cm^{-3}) recorded during the daytime (TABLE 1). The daytime values on weekends were on average

7.7±3.2 μg/m^3 (42.1±11.3 cm^{-3}), indicating that the concentrations of aerosol particles within the measured size range increase during the daytime due to urban activities (FIG. 1a and GIG.1d). The nighttime values inside the closed office were on average 4.3±1.9 μg/m^3 (30.0±12.7 cm^{-3}).

Obviously, the concentrations increased by opening the window and keeping the door closed (nighttime after 29.09.2013); in that case the nighttime values were on average 15.0±6.5 μg/m^3 (63.1±7.5 cm^{-3}) and ranging between 5.2–25.8 μg/m^3 (50.0 – 83.2 cm^{-3}). The highest concentrations were recorded during the daytime on workdays (open office); these ranged between 2.5–261.9 μg/m^3 (15.5–906.4 cm^{-3}) with an average value of 43.7±37.0 μg/m^3 (54.6±49.6 cm^{-3}). The high concentrations during the workdays' daytime period were mainly due to three reasons: First, the urban activities are expected to be more on workdays usually causing higher outdoor concentrations in the daytime than at night; second, both the ventilation rate and the penetration factor are enhanced during the daytime because the office was totally open; and third, the office was occupied by at least the worker himself, who can be considered as a cause of particle re-suspension from the carpet and other surfaces in the office as will be discussed in the next section. According to estimations, the ventilation rate (λ) was ~2 h^{-1} when the office was open and ~0.5 h^{-1} when the office was totally closed. In general, the higher the penetration factor is, the higher are the concentrations inside an office and an enhanced ventilation rate enhances the response in the change-rate of the indoor concentrations [29–33].

TABLE 1. Particulate mass and particulate number concentrations within the measured size-range

		$PM_{10\text{-}0.3}$ [μg/m^3]				$PN_{10\text{-}0.3}$ [1/cm^3]			
Office Condition	**Time Period**	**mean ± std.dev.**	**25%**	**median**	**75%**	**mean ± std.dev.**	**25%**	**median**	**75%**
Totally closed	Period I – Weekends[(a)]	5.7 ± 2.9	3.5	4.7	7.4	37.0 ± 13.3	27.5	36.7	45.9
Totally closed	Period I – Weekends (Daytime) [(b)]	7.7 ± 3.2	4.6	8.3	10.6	42.1 ± 11.3	33.8	40.3	47.6
Totally closed	Period I – Weekends and Workdays (Nighttime) [(c)]	4.3 ± 1.9	3.0	3.9	4.8	30.0 ± 12.7	19.9	28.8	37.3
Open door or/and window	Periods I and II – Workdays (Daytime) [(b)]	43.7 ± 37.0	17.4	34.2	58.4	54.6 ± 49.6	29.1	43.2	62.3
Open window	Period II – Workdays (nighttime) [(c)]	15.0 ± 6.5	9.0	14.7	20.6	63.1 ± 7.5	58.5	62.2	66.1

[(a)] This includes either weekends or workdays as specified by considering the time period 00:00 – 24:00.

[(b)] Daytime period was defined between 08:00 and 18:00.

[(c)] Nighttime period was defined before 06:00 or after 22:00.

Based on the particle number, the coarse fraction was uni-modal (FIG. 2a). The average particle mass size distributions showed that the coarse mode extends beyond 10 μm in diameter (FIG. 2b). The average concentration of the coarse fraction was 6.4±3.0 cm^{-3} μg/m^3 (0.7±0.4 cm^{-3}) during daytime on weekends and 3.3±1.7 μg/m^3 (0.5±0.3 cm^{-3}) during nighttime; during these two cases, the office was totally closed. The average concentrations were 41.4±35.7 μg/m^3 (1.9±1.2 cm^{-3}) when the office was open during the daytime on workdays. When the window was open, they were about 13.0±6.3 μg/m^3 (1.0±0.3 cm^{-3}). Hussein et al. [34] previously measured the total particle number concentrations (D_p > 10 nm) at the same location; they reported the 5-minute average to vary from 10^4 cm^{-3} in the nighttime to a value as high as 10^5 cm^{-3} in the daytime. This indicates that the majority of the aerosol particles are in the fine particle size-range.

Keeping in mind that we generated the mass concentrations by assuming spherical particles and unit density, the mass concentration of the coarse fraction is expected to be at least doubled. Furthermore, the measured particle size diameter was larger than 300 nm, and that suggests higher

values for the PM_{10}. It is, however, difficult to make a reasonable guess for the PM_{10} here, because we do not have enough information about the size distribution of the fine fraction. Based on these two facts, the 24-hour values reported (TABLE 2) here for this office easily exceed what is recommended by the WHO guidelines as 50 $\mu g/m^3$ for PM_{10} and 25 $\mu g/m^3$ for $PM_{2.5}$. The reported numbers are also higher than those found in the literature regarding university buildings. For example, Salma et al. [26] measured the PM_{10} concentrations in a lecture hall at a university in Hungary during a week. The day-to-day variation showed a rather similar trend as that observed here in this study reflecting the high concentrations on workdays' daytime and low concentration at nighttime and weekends. Their reported values for the PM_{10} were as high as 100 $\mu g/m^3$ with a median value of 15.3 $\mu g/m^3$. Gaidajis and Angelakoglou [25] showed that the 24-hour concentrations of PM_{10} and $PM_{2.5}$ varied between 59–220 $\mu g/m^3$ and 45–118 $\mu g/m^3$ in five classrooms, an office and a meeting room located within a university building in Greece. This indicates that the coarse fraction would be in the range 14–102 $\mu g/m^3$. Tran et al. [27] reported PM_{10} concentrations in French classrooms: The weekly averages of occupied classrooms ranged between 72.7 – 85.3 $\mu g/m^3$ and those of unoccupied classrooms ranged between 13.2 – 24.8 $\mu g/m^3$. The corresponding outdoor values were 29.6 – 51 $\mu g/m^3$ and 23.1 – 29.3 $\mu g/m^3$, respectively.

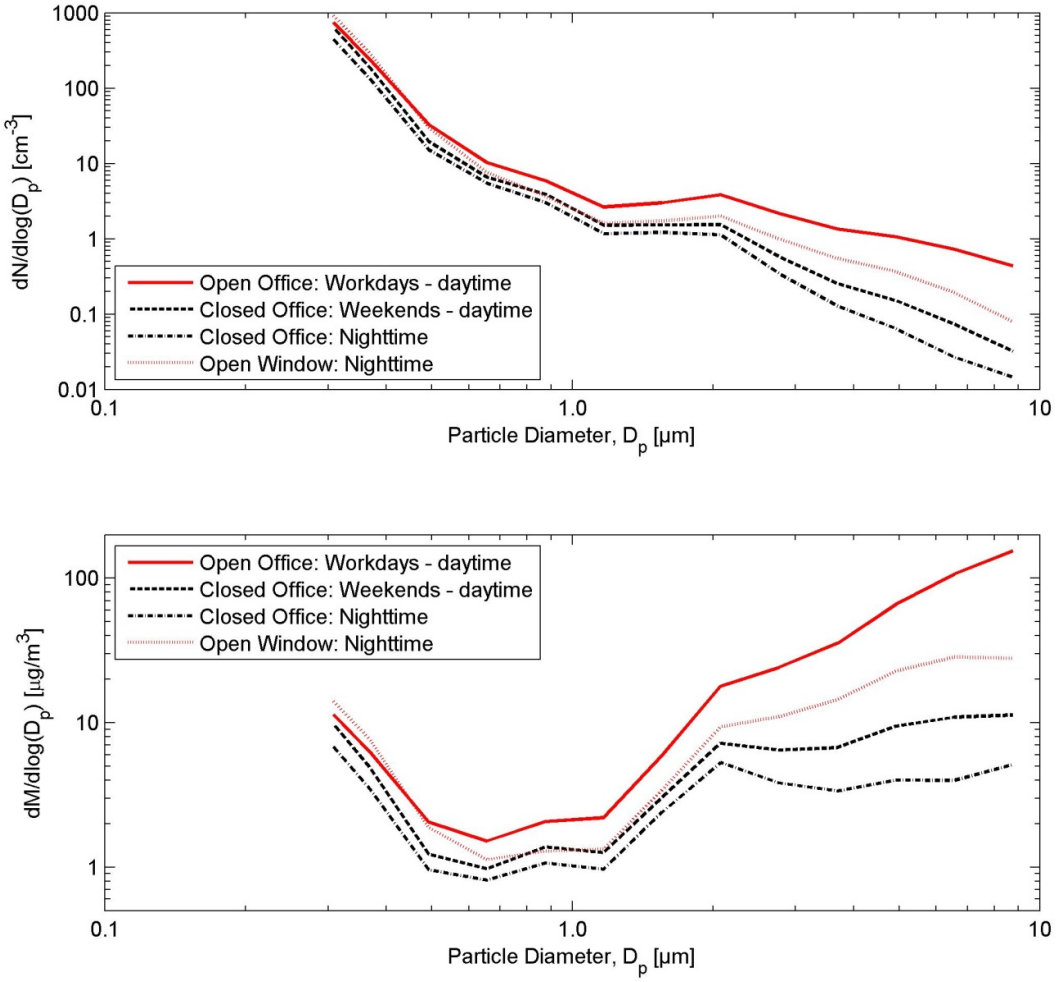

FIG. 2. (a) Average particle number size distributions and (b) the corresponding particle mass size distribution

TABLE 2. Daily averages of the particle mass [µg/m^3] and particle number concentrations [cm^{-3}] within different measured size-fractions

Date	$PM_{10-0.3}$	$PM_{1-0.3}$	PM_{10-1}	$PN_{10-0.3}$	$PN_{1-0.3}$	PN_{10-1}
19.09.2013	28.7	1.8	27.6	60.0	58.5	1.6
20.09.2013	8.5	1.6	7.0	52.4	51.4	1.0
21.09.2013	6.1	1.1	5.1	39.6	39.0	0.6
22.09.2013	16.4	0.8	16.0	24.9	24.0	1.0
23.09.2013	18.7	0.9	18.3	30.9	30.0	0.9
24.09.2013	24.1	1.3	23.4	45.1	43.9	1.2
25.09.2013	14.0	0.8	13.5	25.5	24.7	0.8
26.09.2013	43.2	6.6	37.3	181.8	180.1	1.9
27.09.2013	6.9	1.5	5.5	54.5	54.0	0.6
28.09.2013	4.4	1.1	3.4	44.0	43.7	0.3
29.09.2013	18.2	1.1	17.6	44.0	43.3	0.7
30.09.2013	29.6	2.0	28.1	75.6	74.3	1.3

Concentrations during Office Activities: Tobacco Smoke and Re-suspension

So far, we have not considered the unusual activities (such as smoking or more than two visitors/students) in the office. The concentrations were as high as 3729.2 µg/m^3 (4854.5 cm^{-3}) during the smoking event on Thursday 29.09.2013 (FIG. 1a and FIG. 1d). Another smoking event occurred in the nearby office on Tuesday 24.09.2013; that caused the concentrations to reach as high as 235 µg/m^3 (150 cm^{-3}). The coarse particle size fraction did not show any change due to these smoking events and the increase in the concentrations was mainly observed in the particles smaller than 1 µm in diameter (FIG. 3). It is very well noticed that the tobacco smoke remained in the office for longer than 40 minutes.

Afshari et al. [35] considered cigarette smoking during 10 minutes and showed that the fine particle number concentration and also particles larger than 1 µm suddenly increased to more than 10^5 cm^{-3} and stayed airborne for more than 100 minutes. Hussein et al. [31] reported that smoking a cigarette in a living room increased the fine particle number concentrations from the background level (6×10^3 cm^{-3}) to about 3.6×10^4 cm^{-3} with a well-distinguished fine mode extending up to 600 nm. He et al. [36] also measured the fine particle number concentrations of tobacco smoke to be 2.7×10^4 cm^{-3}, which was about 1.5 the background level. Morawska et al. [37] reported even concentrations as high as 3.5×10^6 cm^{-3} during tobacco smoking.

The concentrations during the daytime on workdays were significantly higher than those observed during the same time period on weekends. Entering the office when it was totally closed caused the concentrations of coarse particles to increase suddenly. For example, the routine check-up visit on Saturday 28.09.2013 (around 14:00) increased the PM_{10-1} from 5 µg/m^3 to about 20 µg/m^3 (PN_{10-1} from 0.3 cm^{-3} to about 1 cm^{-3}) (FIG. 1a and FIG. 1d). The size fraction below 1 µm did not show changes in concentration (FIG. 4). This is a strong indication of the re-suspension process by walking over the carpet and also probably disturbing the dust layer accumulated on other surfaces.

At school gyms, Branis and Safranek [9] reported that the indoor-to-outdoor (I/O) ratio of the coarse particle fraction on workdays was higher than two, where the indoor $PM_{10-2.5}$ varied between 1.2–29.4 µg/m^3. During weekends and holidays, the I/O ratio was below 0.5 with the indoor $PM_{10-2.5}$ varied between 0.5–4.9 µg/m^3. According to Branis and Safranek [9], the differences were explained by sport activities in the gyms that enhance re-suspension of particulate matter. In another study about school gyms, Buonanno et al. [8] confirmed that the I/O ratio of the $PM_{10-2.5}$ was 4.8±2.0 with the dominant indoor source being the particle re-suspension due to exercising activities of pupils. Buonanno et al. [8] estimated the $PM_{10-2.5}$ emission factors in the range of 1.5–8.9 mg/min. These re-suspension rates were slightly higher than those presented by Ferro et al. [7] as 0.03–0.5 mg/min for $PM_{2.5}$ and 0.1–1.4 mg/min for PM_5. The differences between Buonanno et al. [8] and Ferro et al. [7] are possibly due to the difference in the considered particle size range.

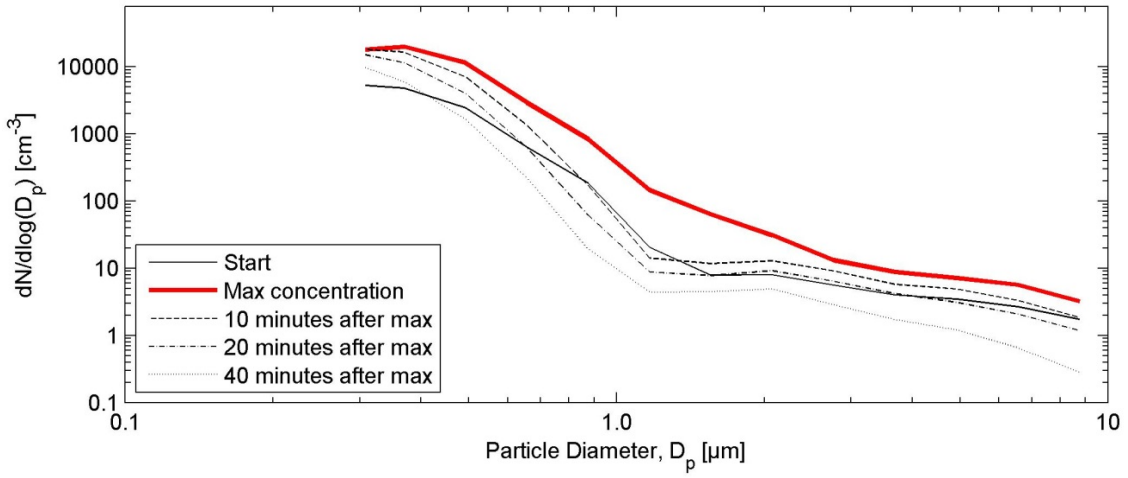

FIG. 3. Evolution of the particle number size distribution during the smoking event on Thursday 26.09.2013. The office was open

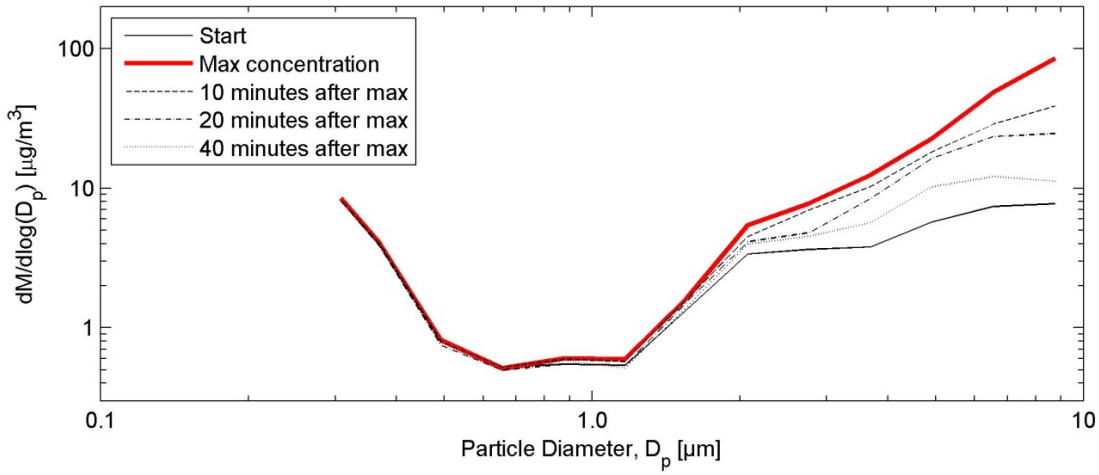

FIG. 4. Evolution of the particle mass size distribution as an example of particle re-suspension due to walking into the office on Saturday 28.09.2013. The office was totally closed

Conclusions

We measured the particle number size distribution (diameter 0.3–10 µm and one minute time-resolution) inside a naturally ventilated office located at a university building in Jordan. The measurement campaign covered a time period of two weeks (18.09.2013 – 01.10.2013) with 100% valid data. We focused on the variation of the particle number and particle mass (assuming spherical particles with unit density) concentrations, their differences between workdays and weekends and the effect of special activities inside the office (tobacco smoking and re-suspension). We also focused on three scenarios of office conditions: totally closed, totally open and open window. The ventilation rate was estimated by utilizing a simple indoor aerosol model.

The 24-hour means of the $PM_{10-0.3}$ ranged between 16.4–43.2 µg/m^3 and 4.4 – 8.5 µg/m^3 on workdays and weekends, respectively. They ranged between 7.7±3.2 µg/m^3 (42.1±11.3 cm^{-3}) and 4.3±1.9 µg/m^3 (30.0±12.7 cm^{-3}) when the office was totally closed at daytime (weekends) and nighttime, respectively. The $PM_{10-0.3}$ ranged between 5.2–25.8 µg/m^3 (50.0 – 83.2 cm^{-3}) when the window was open at night. The highest concentrations were observed during the daytime on workdays (open office); these ranged between 2.5–261.9 µg/m^3 (15.5–906.4 cm^{-3}). The

differences in the closed office conditions between daytime and nighttime are simply explained by higher concentrations outdoors during the time reflecting the increased urban activities in the city. Opening the window caused an increase in the concentrations as a result of enhanced ventilation rate and penetration factor. The highest concentrations on workdays daytime are believed to be the result of several factors: (1) increased urban activities on workdays' daytime, (2) enhanced ventilation rate and penetration factor, because the office was open and (3) the office was occupied by at least the worker himself who can be considered as a cause of particle re-suspension from the carpet and other surfaces. The concentrations were as high as 3729.2 $\mu g/m^3$ (4854.5 cm^{-3}) during the smoking events inside the office, where the tobacco smoke effect remained for more than 40 minutes.

The particle number size distribution of the coarse fraction was uni-modal, whereas the particle mass size distributions showed that the uni-mode extends beyond 10 µm in diameter. The average concentration of the coarse fraction was about 3.3±1.7 $\mu g/m^3$ (0.5±0.3 cm^{-3}) during nighttime, whereas during workdays' daytime it was 41.4±35.7 $\mu g/m^3$ (1.9±1.2 cm^{-3}).

It should be emphasized that the mass concentrations presented here were calculated by assuming spherical particles and unit density and the measured size-range was larger than 300 nm in diameter. Therefore, the PM_{10} is expected to be at least double the numbers shown in this study, which implies that the 24-hour PM_{10} in this office likely exceeds what is recommended by the WHO guidelines.

Acknowledgement

This study was fully sponsored by the Faculty of Scientific Research at the University of Jordan.

References

[1] Hussein, T., Paasonen, P. and Kulmala, M., Sci. Total Environ., 425 (2012) 289.

[2] Lan, L., Wargocki, P., Wyon, D.P. and Lian, Z., Indoor Air, 21 (2011) 376.

[3] Mendell, M.J. and Fisk, W.J., Occup. Environ. Med., 64 (2007) 69.

[4] Marmot, A.F., Eley, J., Stafford, M., Stansfeld, S.A., Warwick, E. and Marmot, M.G., Occup. Environ. Med., 63 (2006) 283.

[5] Morawska, L., He, C., Johnson, G., Jayaratne, R., Salthammer, T., Wang, H., Uhde, E., Bostrom, T., Modini, R., Ayoko, G., McGarry, P. and Wensing, M., Environ. Sci. Technol., 43 (2009) 1015.

[6] Koivisto, J., Hussein, T., Niemelä, R., Tuomi, T. and Hämeri, K., Atmos. Environ., 44 (2010) 2140.

[7] Ferro, A.R., Kopperund, R.J. and Hildemann, L.M., Environ. Sci. Technol., 38 (2004) 1759.

[8] Buonanno, G., Fuoco, F.C., Marini, S. and Stabile, L., Aerosol Air Qual. Resear., 12 (2012) 803.

[9] Branis, M. and Safranek, J., Environ. Resear., 111 (2011) 485.

[10] Kubota, Y. and Higuchi, H., Aerosol Sci. Technol., 47 (2013) 208.

[11] Slezakova, K., Pereira, M.C. and Alvim-Ferraz, M.C., Atmos. Environ., 43 (2009) 486.

[12] Fisk, W.J., Faulkner, D., Sullivan, D. and Mendell, M.J., Aerosol Sci. Technol., 32 (2000) 527.

[13] Zuraimi, M.S. and Tham, K.W., Build. Environ., 44 (2009) 2475.

[14] Smolík, J., Lazaridis, M., Moravec, P., Schwarz, J., Zaripov, S.K. and Zdímal, V., Water Air Soil Poll., 165 (2005) 301.

[15] Kagi, N., Fujii, S., Horiba, Y., Namiki, N., Ohtani, Y., Emi, H., Tamura, H. and Kim, Y.S., Build.Environ., 42 (2007) 1949.

[16] Lee, C. W. and Hsu, D. J., Atmos. Environ., 41 (2007) 6598.

[17] Hussein, T., Hämeri, K. and Kulmala, M., Boreal Environ. Resear., 7 (2002) 141.

[18] Hussein, T., Hämeri, K., Aalto, P., Asmi, A., Kakko, L. and Kulmala, M., Scand. J. Work Health Environ., 30(2) (2004) 54.

[19] Hussein, T., Korhonen, H., Herrmann, E., Hämeri, K., Lehtinen, K. and Kulmala, M., Aerosol Sci. Technol., 39 (2005b) 1111.

[20] Quang, T.N., He, C., Morawska, L. and Knibbs, L.D., Atmos. Environ., 79 (2013) 41.

[21] Koivisto, A.J., Mäkinen, M., Rossi, E.M., Lindberg, H.K., Miettinen, M., Falck, G.C.M., Norppa, H., Alenius, H., Korpi, A., Riikonen, J., Vanhala, E., Vippola, M., Pasanen, P., Lehto, V.P., Savolainen, K., Jokiniemi, J. and Hämeri, K., J. Nanoparticle Resear., 13 (2011) 2949.

[22] Koivisto, A.J., Lyyränen, J., Auvinen, A., Vanhala, E., Hämeri, K., Tuomi, T. and Jokiniemi, J., Inhal. Toxicol., 24 (2012) 839.

[23] Koivisto, A.J., Mikko, A., Mäkelä, J., Pasanen, P., Hussein, T. and Hämeri, K., Am. Chem. Soc. Nano, 6 (2012) 1195.

[24] Zitnik, M., Kastelic, A., Rupnik, Z., Pelicon, P., Vaupetic, P., Bucar, K., Novak, S., Samardzija, Z., Matsuyama, S., Catella, G. and Ishii, K., Atmos. Environ., 44 (2010) 4954.

[25] Gaidajis, G. and Angelakoglou, K., J. Environ. Sci. Health – Part A, 44 (2009) 1227.

[26] Salma, I., Dosztály, K., Borsós, T., Söveges, B., Weidinger, T., Kristóf, G., Péter, N. and Kertész, Z., Atmos. Environ., 64 (2013) 219.

[27] Tran, D.T., Alleman, L.Y., Coddeville, P. and Galloo, J. C., Atmos. Environ., 54 (2012) 0250.

[28] Mølgaard, B., Ondráček, J., Šťávová, P., Džumbová, L., Barták, M., Hussein, T. and Smolík, J., Indoor Built Environ., (2013) (doi: 10.1177/1420326X13481484).

[29] Hussein, T. and Kulmala, M., Water Air Soil Pollut.: Focus, 8 (2008) 23.

[30] Hussein, T., Hämeri, K., Heikkinen, M.S.A. and Kulmala, M., Atmos. Environ., 39 (2005a) 3697.

[31] Hussein, T., Glytsos, T., Ondráček, J., Ždímal, V., Hämeri, K., Lazaridis, M., Smolik, J. and Kulmala, M., Atmos. Environ., 40 (2006) 4285.

[32] Hussein, T., Hruška, A., Dohányosová, P., Džumbová, L., Hemerka, J., Kulmala, M. and Smolik, J., Atmos. Environ., 43 (2009) 905.

[33] Hussein, T., Mølgaard, B. and Hämeri, K., Aerosol Air Qual. Resear., 11 (2011) 309.

[34] Hussein, T., Abu Al-Ruz, R., Petäjä, T., Junninen, H., Arafah, D.E., Hämeri, K. and Kulmala, M., Aerosol Air Qual. Resear., 11 (2011) 109.

[35] Afshari, A., Matson, U. and Ekberg, L.E., Indoor Air, 15 (2005) 141.

[36] He, C., Morawska, L., Hitchins, J. and Gilbert, D., Atmos. Environ., 38 (2004) 3405.

[37] Morawska, L., He, C., Hitchins, J., Mengersen, K. and Gilbert, D., Atmos. Environ., 37 (2003) 4195.

Volume 7, Number 2, 2014. pp. 85-98

Jordan Journal of Physics

ARTICLE

Structural and Mössbauer Studies of Ball Milled Co-Zn Y-type Hexaferrites

M. A. Awawdeh[a], **R.N. Al-Bashaireh**[a], **A-F. Lehlooh**[a] and **S.H. Mahmood**[b]

[a] *Department of Physics, Yarmouk University, Irbid, Jordan.*
[b] *Department of Physics, The University of Jordan, Amman, 119-42, Jordan.*

Received on: 31/5/2014; Accepted on: 22/7/2014

Abstract: Y-type hexaferrite samples $Ba_2Zn_xCo_{2-x}Fe_{12}O_{22}$ with x = 0, 1 and 2 were prepared from precursors synthesized by the citrate sol-gel auto combustion method. The powders were sintered at 1100° C for four hours. X-ray diffraction, scanning electron microscopy and Mössbauer spectroscopy were used to investigate the effect of ball milling on the structure, microstructure and on the hyperfine parameters. X-ray diffraction revealed the presence of a single Y-type hexaferrite in all sintered samples. This phase persisted in samples milled for periods up to four hours. Scanning electron microscopy images indicated that the particles changed shape, and their sizes reduced by a factor of 10 for milling times of four hours. Room temperature Mössbauer spectra of the hexaferrites elucidated the distribution of the various cations at the various sites of the hexaferrite lattice. The hyperfine field (B_{hf}) associated with each component was found to decrease almost exponentially with increasing milling time. The reduction in hyperfine field was associated with the weakening of the superexchange interactions between the spin-up and spin-down sublattices as a consequence of replacing Co^{2+} magnetic ions by non-magnetic Zn^{2+} ions and with the microstructure in the milled samples.
Keywords: Y-type hexaferrites; Ball-milling; Sintering; XRD; Mössbauer spectroscopy.

Introduction

The fabrication and characterization of different types of hexagonal ferrites and their modification by selected types of cationic substitutions had attracted the interest of a large community of scientists and technologists in the past few decades. Interest in these materials was stimulated by their potential for a wide range of technological and industrial applications, specifically, in permanent magnets, high density magnetic recording, high frequency telecommunication devices and multi-layer electronic components [1 - 6].

Hexaferrites can be classified as M-, W-, X-, Y-, Z- and U-type ferrites depending on their chemical formula and crystal structure [4, 6, 7]. The Y-type hexaferrite (also called ferroxplana), with the chemical formula $Ba_2Me_2Fe_{12}O_{22}$, has a unit cell TST'S'T"S", where the primes indicate rotation by 120° about the c-axis. The Ba ions in the structure could be replaced completely or partially by other cations such as Sr or Pb, and Me are divalent ions. This structure has an easy plane perpendicular to the *c*-axis (thus the name ferroxplana) with space group ($R\bar{3}m$) and lattice parameters: a = 5.89 Å and c = 43.56 Å [4]. The metallic cations (Me) and iron ions are distributed in six crystallographic sites: two tetrahedral sites ($6c_{IV}$ and $6c_{IV}$*) and four octahedral sites ($3a_{VI}$, $18h_{VI}$, $6c_{VI}$ and $3b_{VI}$) as indicated in Table 1 [2, 8, 9].

Corresponding Author: M. A. Awawdeh **Email**: amufeed@yu.edu.jo.

TABLE 1. Metallic sublattices of Y structures and their properties

Sublattices	Coordination	Block	Number of ions per unit cell	Spin
$6c_{IV}$	Tetra	S	6	Down
$3a_{VI}$	Octa	S	3	Up
$18h_{VI}$	Octa	S-T	18	Up
$6c_{VI}$	Octa	T	6	Down
$6c_{IV*}$	Tetra	T	6	Down
$3b_{VI}$	Octa	T	3	Up

Recent Mössbauer and magnetic studies on BaM and SrM hexaferrites have demonstrated the importance of the type and concentration of metal substitutions for Fe on the magnetic anisotropy and saturation magnetization of the prepared systems [10-15]. However, little had been reported in the literature concerning the preferential site occupation of the metal cations in Y-type hexaferrites, with conflicting reports in some cases [16-18].

It is well known that the grain size of a magnetic powder has a significant influence on the magnetic properties of the substance. Hexaferrites prepared by the solid state reaction method have typical grain size exceeding the critical single domain size of about 0.5 μm. In such grains, magnetization processes are influenced by domain wall motion, which leads to significant reduction in the coercivity of the powder sample. However, if the grain size is reduced below this value, the grains become single-domain and the coercivity improves significantly. Further reduction of the grain size below 100 nm leads to the development of a superparamagnetic powder, with significantly reduced coercivity and remanance magnetization which approach zero at a grain size of 10 – 20 nm. Although such systems are of no importance to applications requiring high coercivity and remanence, they are still of great importance for magnetic switching applications [4]. Further, magnetic nano-particles have promising biomedical applications such as MRI contrast agents, hyperthermia, target drug delivery and cellular imaging [4]. The range of grain size of the magnetic material is therefore of critical importance to the type of the required application.

The present work is concerned with the synthesis of Co-Zn Y-type hexaferrite powders with reduced particle size. The samples were prepared using sol-gel method and appropriate sintering. To reduce the particle size, the prepared compounds were ball milled for different milling times, then characterized using X-ray diffraction and Mössbauer spectroscopy to have an understanding of the effect of milling on the hyperfine parameters of the system.

Experimental Procedures

A series of samples $Ba_2Zn_xCo_{2-x}Fe_{12}O_{22}$ with x = 0.0, 1.0 and 2.0 were prepared using the citrate sol-gel auto combustion method explained in a previous publication [17]. Appropriate amounts of high purity Fe $(NO_3)_3$ _ $9H_2O$, $Ba(NO_3)_2$, $Zn(NO_3)_2$ _ $6H_2O$ and $Co(NO_3)_2$ were dissolved in distilled water, and an aqueous solution of citric acid was then added at 80 ^oC to chelate Ba^{+2} and Fe^{+3} ions in the solution. The pH of the solution was maintained at 7 by dropwise addition of ammonia. The solution was then slowly heated until the water evaporated resulting in a viscous gel, which has subsequently undergone a self-propagating combustion resulting in a loose powder. The resulting powder was preheated at 450 ^oC for 1 h and then sintered in air at 1100 ^oC for 4 h using a heating rate of 10 ^oC /min.

Planetary ball mill is a useful tool for reducing the particle size of a powder to an order of 100 nm, and thus obtaining single-domain particles [19]. The samples were ball-milled at different times using a Fritch type planetary ball mill. The rotating speed of the mill was set to 400 rpm. The bowls and balls of the mill are made of Tungsten Carbide and the powder-ball ratio was 1:20.

Mössbauer samples were prepared as a thin circular layer of the system powder pressed gently between two Teflon disks with a diameter of 2 cm, which is small compared with the distance between the source and the sample in order to avoid angular broadening of the spectrum. Mössbauer spectra were collected using a standard constant acceleration Mössbauer spectrometer over 1024 channels. The Mössbauer spectra were analyzed using

standard fitting routines to obtain the hyperfine parameters.

The samples for the structural studies were prepared by sprinkling the powders on a microscope glass that has no structural peaks. The crystalline structure of each sample was investigated using (θ-2θ) X-ray diffractometer (Philips PW1729).

The morphology of the prepared samples was examined by scanning electron microscope (SEM FEI Quanta 200) equipped with energy dispersive X-ray spectroscopy (EDAX) facility for elemental analysis.

Results and Discussion

XRD Measurements

The XRD patterns were obtained for the samples milled at different times. It is obvious that milling for relatively short time periods (≤ 4 h) does not change the patterns appreciably as sown in Fig.1 – Fig. 3 for the samples with different *x* values. All patterns show single-phase, and the pattern for the sample with x = 0 is consistent with the standard pattern for Co_2Y hexaferrite (JCPDS 00-044-0206), while the pattern for the sample with x = 2 is consistent with the standard pattern for Zn_2Y hexaferrite phase (JCPDS: 00-044-0207). However, the XRD peaks broaden, and the intensities reduce with increasing milling time, indicating the reduction in crystallite size.

The average crystallite sizes for the samples were calculated using Scherrer formula:

$$D = k\lambda/\beta\cos\theta$$

where; D is the crystallite size, k is the Scherrer constant (0.94), λ is the wavelength of radiation (1.542 Å), β is the peak width at half maximum measured in radians and θ is the peak position. Table 2 shows the crystallite sizes for samples milled at 4 h to be compared with those for the un-milled samples.

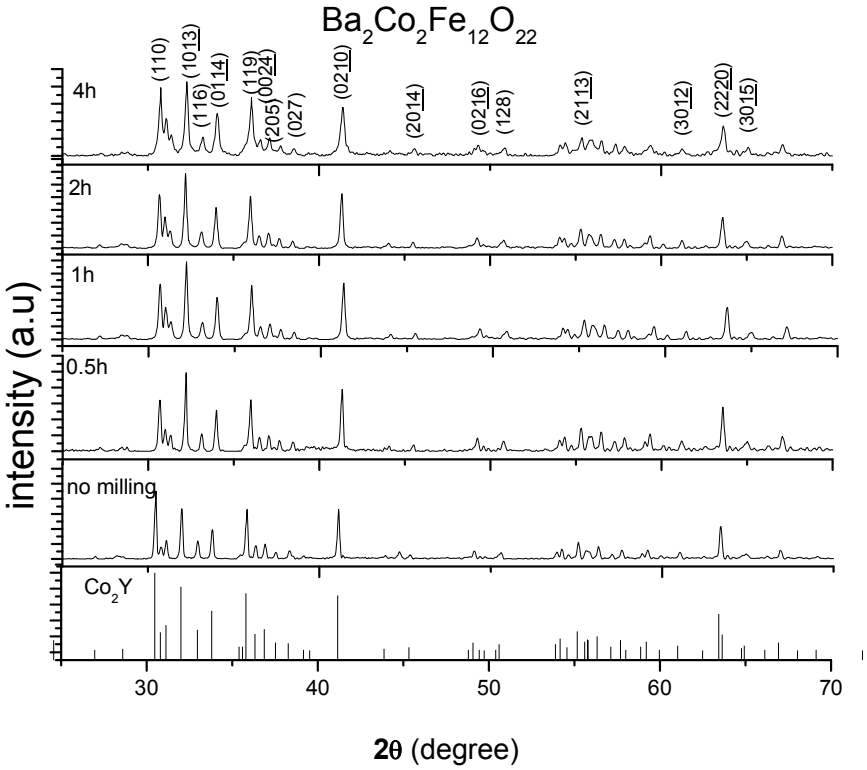

FIG. 1. XRD pattern for Ba_2 $Co_2Fe_{12}O_{22}$ with different milling times

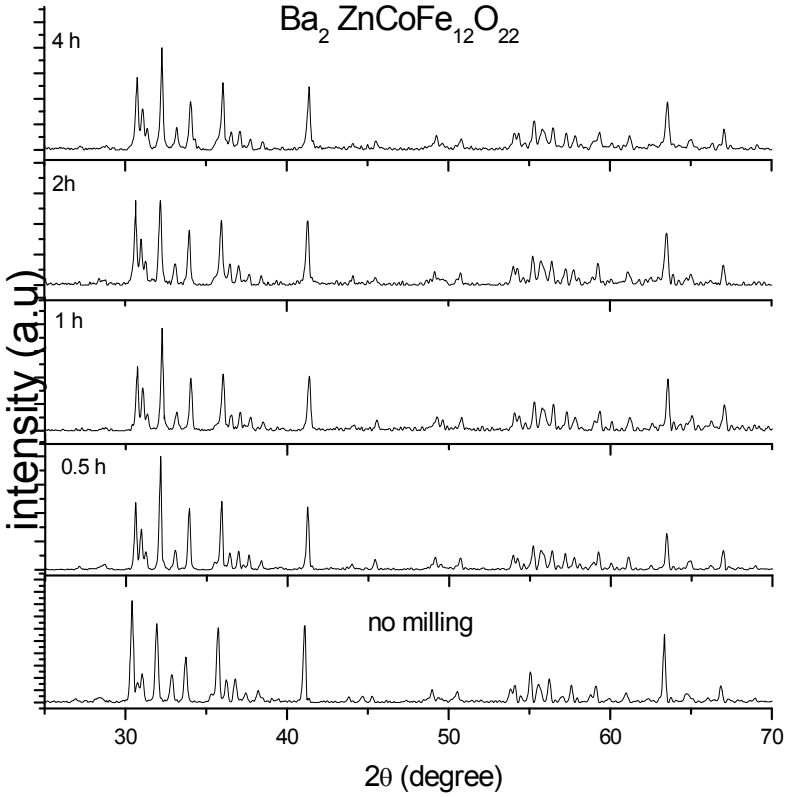

FIG. 2. XRD pattern for Ba_2 $ZnCoFe_{12}O_{22}$ with different milling time

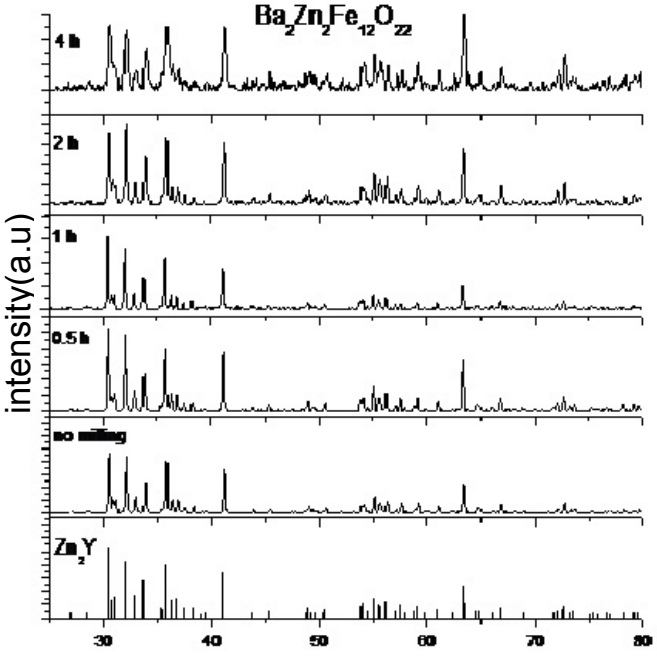

FIG. 3. XRD pattern for Ba_2 $Zn_2Fe_{12}O_{22}$ with different milling times

TABLE 2. Average crystallite size for $Ba_2Zn_xCo_{2-x}Fe_{12}O_{22}$ powders milled for 4 hours

Zn concentration (x)	Crystallite size before milling (nm)	Crystallite size after 4 h milling (nm)
0.0	61 ± 5	32 ± 2
1.0	47 ± 5	35 ± 2
2.0	41 ± 5	35 ± 2

Milling the samples for longer milling times resulted in an appreciable broadening of the reflections and a reduction of the diffracted intensity while maintaining the general hexaferrite structure as shown in Fig. 4a for the sample with x = 2. The average crystallite size for this sample was reduced down to (27 nm) for the sample milled for 8 h, and to (21 nm) for that milled for 16 h. The variation of the crystallite size with milling time for x = 2 sample is shown in Fig. 4b. Similar behavior was also observed for the other samples with x = 0 and x = 1.

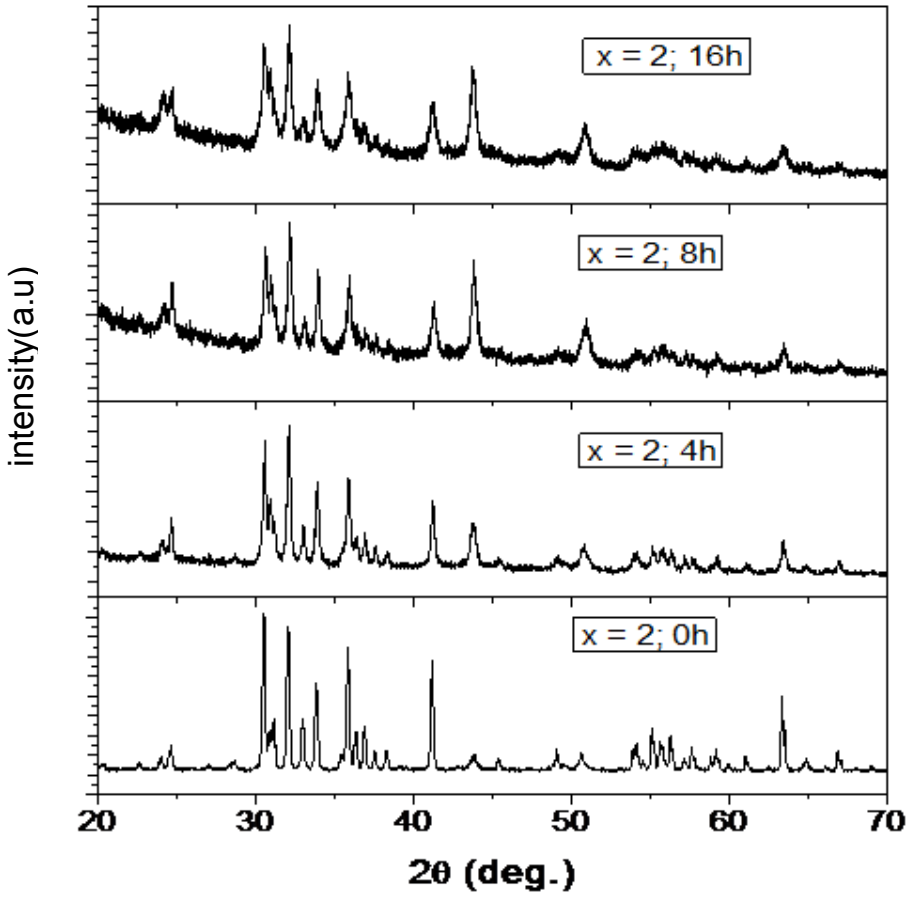

FIG. 4a. XRD pattern for $Ba_2 Zn_2Fe_{12}O_{22}$ with longer milling times for crystallite size analysis

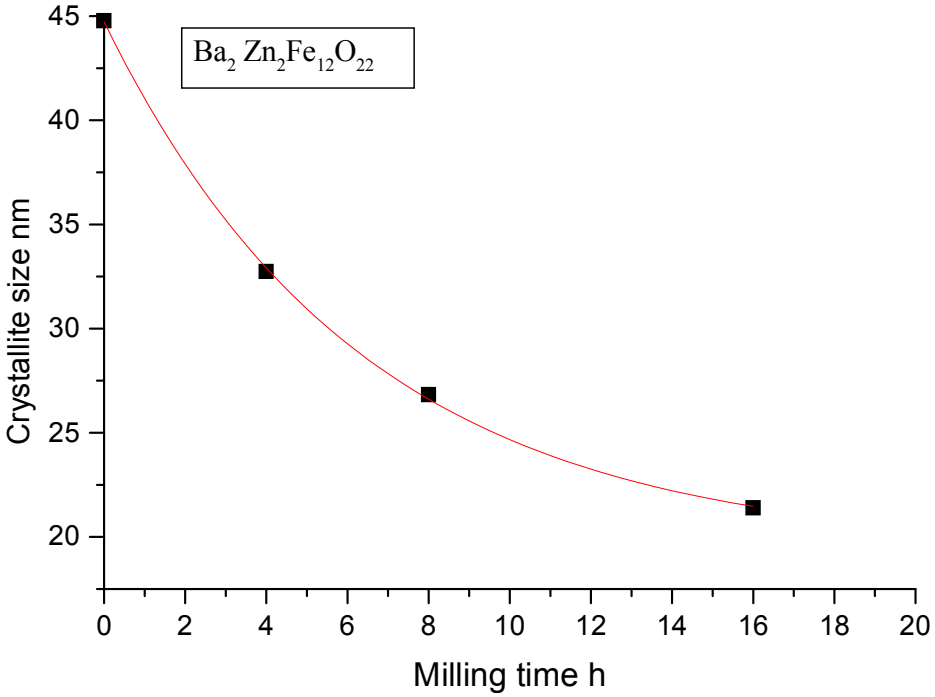

FIG. 4b. The variation of crystallite size for $Ba_2\ Zn_2Fe_{12}O_{22}$ with milling time

Scanning Electron Microscopy (SEM)

SEM photos for the un-milled and milled ferrite samples (4 h milling time) are shown in Figs. 5, 6 and 7 for x = 0, 1and 2, respectively. The images indicate that the milling process resulted in a change of the shape of the particles from platelet-like to a more or less spherical shape. In addition, the milled samples are composed of small particles which are about an order of magnitude smaller than the original particles. The particles in the un-milled samples have diameters ranging between 1 and 4 μm, while the samples milled for 4 h show that the majority of the particles have diameters in the range between 150 and 250 nm, with a small fraction of larger platelet-like particles, which indicates that the milling time was not sufficient for the production of a homogeneous powder. The physical particle size determined by SEM imaging is significantly larger than the crystallite size determined from the analysis of the XRD line profiles. This is indicative of the presence of crystal defects resulting in the formation of poly-crystalline particles.

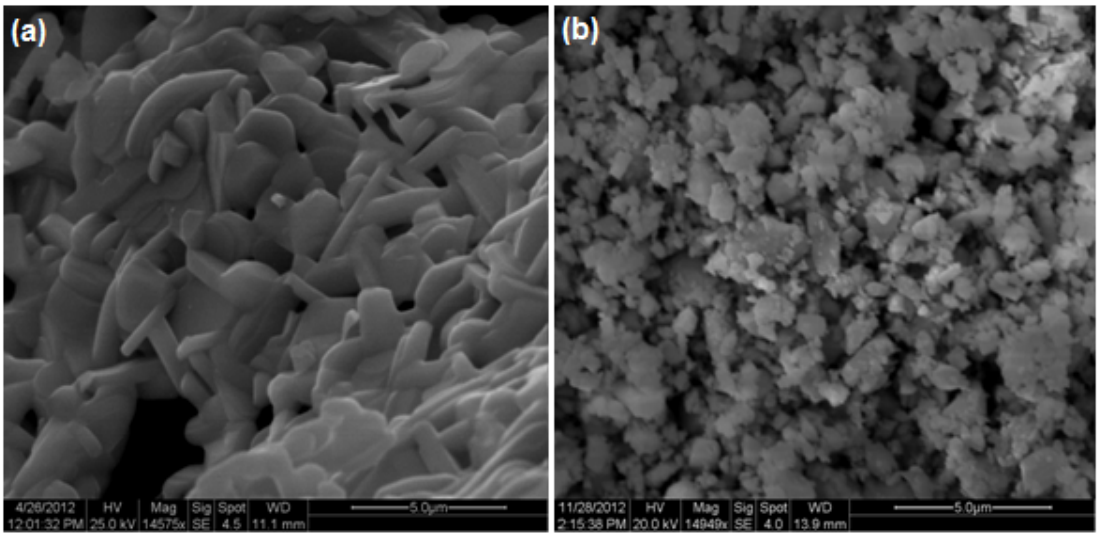

FIG. 5. SEM images for the sample with x = 0. (a) The un-milled sample, and (b) The sample milled for 4 h

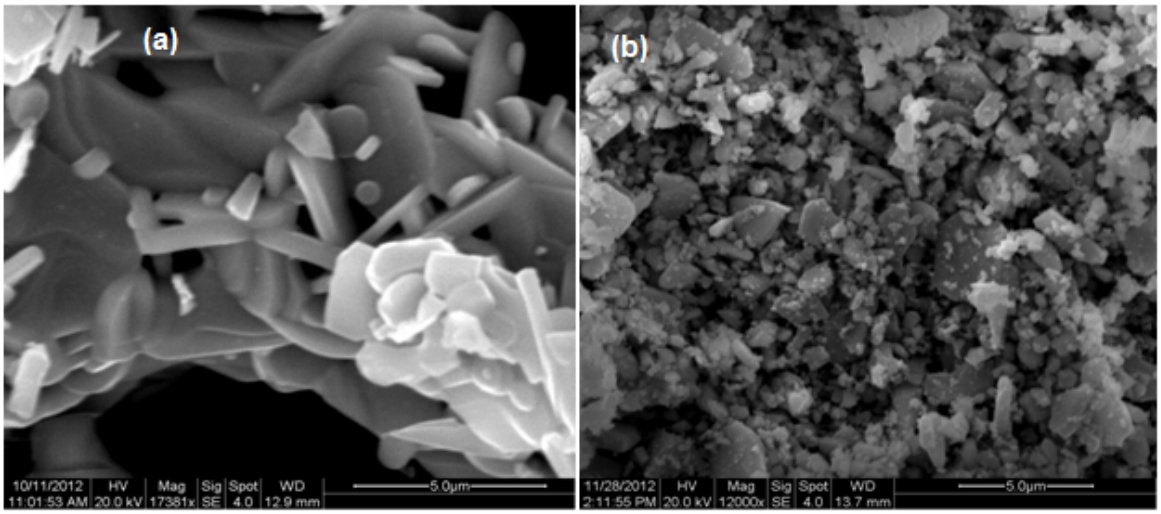

FIG. 6. SEM images for the sample with $x = 1$. (a) The un-milled sample, and (b) The sample milled for 4 h

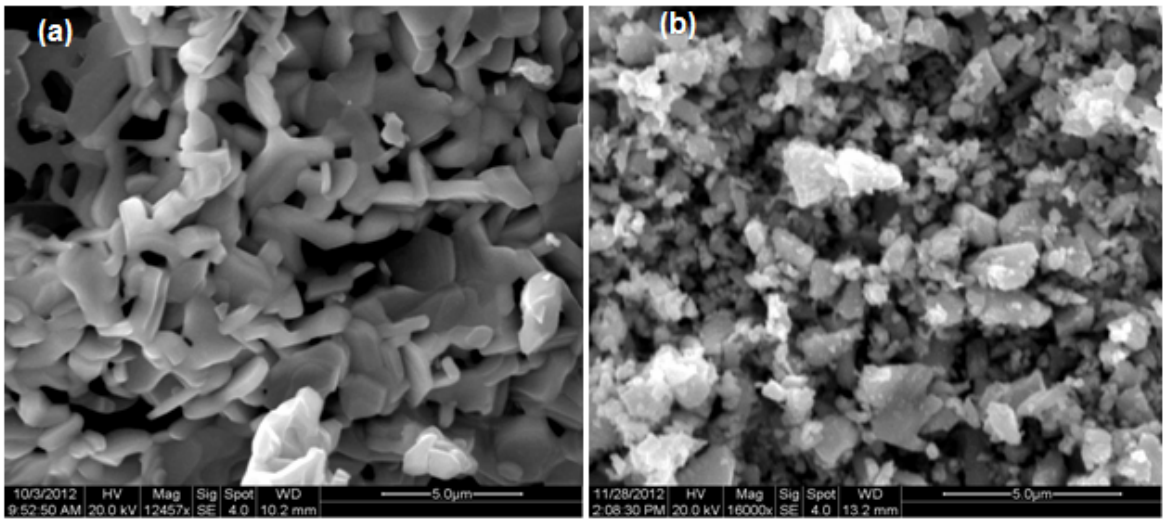

FIG. 7. SEM images for the sample with $x = 2$. (a) The un-milled sample, and (b) The sample milled for 4 h

Mössbauer Spectroscopy

Room temperature Mössbauer spectra of the samples of $Ba_2Zn_xCo_{2-x}Fe_{12}O_{22}$ (x = 0, 1 and 2) with different milling times (T = 0, 0.5, 1, 2, 4 and 8 h) were recorded and then fitted using dedicated component fit routines. The spectra for the samples with x = 0 with different milling times are shown in Fig. 8. The figure shows similar spectral structure with slightly different spectral characteristics for the sample milled for different times. This is consistent with the results of XRD measurements which indicate that the Y-type hexaferrite phase does not change at four hour milling and is still a pure phase. Mössbauer spectra for the samples milled up to 4 h were fitted with three sextet components. The high field component (I) is associated with Fe^{3+} ions at the ($6c_{IV}^{*}$ + $3b_{VI}$) sites, the middle component (II) with the $18h_{VI}$ sites and the low field component (III) with the ($3a_{VI}$ + $6c_{VI}$ + $6c_{IV}$) sites in accordance with the assignment adopted in [17]. The spectrum of the sample milled for 8h was best fitted with the three above mentioned magnetic sextets and a broad, central paramagnetic component. This component could be an indication of the presence of small superparamagnetic particles in the powder, which were produced by virtue of the excessive grinding.

The values of the hyperfine parameters for the three-component fit are listed in Table 3 (T = 0 h). From the spectrum of the un-milled sample,

the first component (I) with B_{hf} = 49.0 T and a relative intensity of 20 % is associated with the ($6c_{IV}$* + $3b_{VI}$) sites as indicated above. The second component (II) with B_{hf} = 46.4 T and a relative intensity of 45 % is associated with the $18h_{VI}$ sublattice, while the third component (III) with B_{hf} = 42.9 T and a relative intensity of 35 % is attributed to the combination ($3a_{VI}$ + $6c_{VI}$ + $6c_{IV}$) sites.

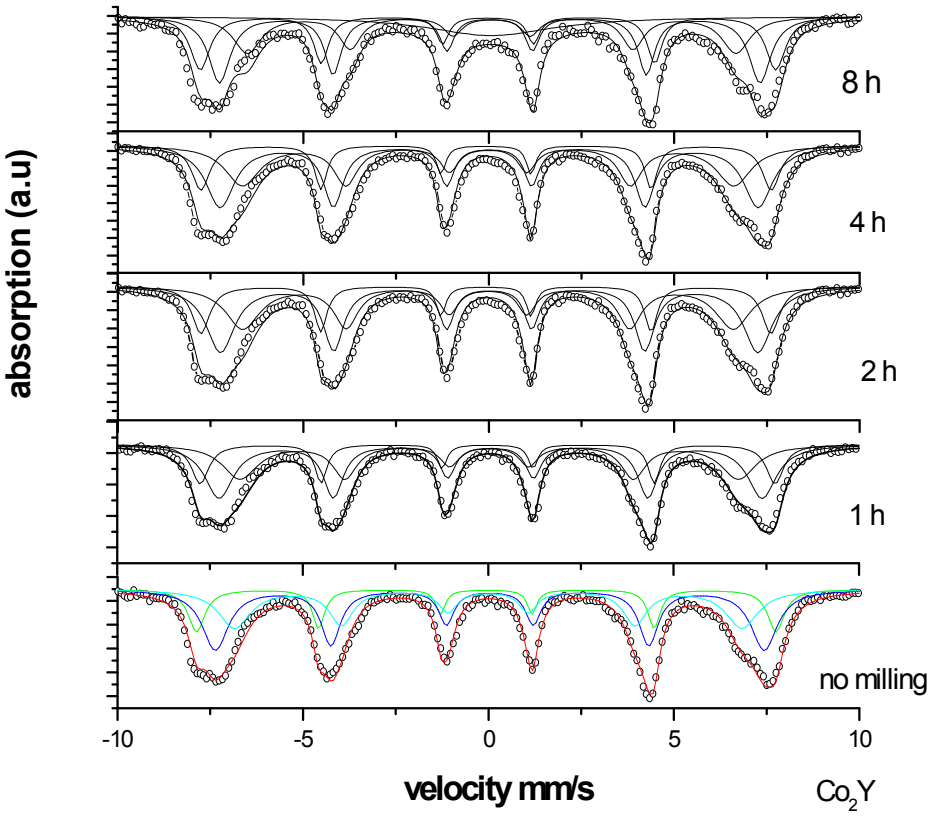

FIG. 8. Room temperature Mössbauer spectra of the sample $Ba_2Co_2Fe_{12}O_{22}$ sintered at temperature T = 1100° C and different milling times (T = 0, 1, 2, 4 and 8 h)

TABLE 3. Room temperature Mössbauer parameters of $Ba_2Co_2Fe_{12}O_{22}$ sintered at T = 1100° C, hyperfine field B_{hf}, center shift CS, relative intensity of the spectral component and line width (W) for inner lines

Mössbauer Parameters	**T = 0 h**	**T = 1 h**	**T = 2 h**	**T = 4 h**	**T = 8 h**
B_{hf}I(T) ± 0.5 T	49.0	48.6	48.4	48.2	48.3
B_{hf}II(T) ± 0.5 T	46.4	45.9	45.5	45.5	45.4
B_{hf}III(T) ± 0.5 T	42.9	42.1	41.4	41.5	41.2
QQ(mm/s) ± 0.04 mm/s					0.06
CS I (mm/s) ± 0.02 mm/s	0.3	0.34	0.28	0.32	0.31
CS II (mm/s) ± 0.02 mm/s	0.39	0.42	0.36	0.31	0.38
CS III (mm/s) ± 0.02 mm/s	0.34	0.37	0.33	0.33	0.10
CS QQ(mm/s) ± 0.02 mm/s					0.41
Relative Intensity I (%)	20	20	20	20	25
Relative Intensity II (%)	45	45	45	45	35
Relative Intensity III (%)	35	35	35	35	25
Relative Intensity QQ (%)					15
Width I (W) (mm/s)	0.31	0.3	0.30	0.29	0.39
Width II (W) (mm/s)	0.50	0.50	0.48	0.49	0.46
Width III (W) (mm/s)	0.61	0.61	0.58	0.59	0.62
Width QQ (W) (mm/s)					4.74

For no milling time of x = 0, the maximum capacity of the ($6c_{IV}^{*}$ + $3b_{VI}$) sites for Fe^{3+} ions is 3 ions per formula (25% of the 12 iron ions in a formula unit), and the maximum capacity of the $18h_{VI}$ site is 6 ions (50%), while the maximum capacity of the ($3a_{VI}$ + $6c_{VI}$ + $6c_{IV}$) sites is 5 ions (41.7%). The relative intensity of 45% of the middle component suggests that 5.4 Fe^{3+} ions per formula occupy the $18h_{VI}$ sites and the relative intensity of 20% and 35% of the low and high field components are consistent with 2.4 Fe^{3+} ions occupying the ($6c_{IV}^{*}$ + $3b_{VI}$) sites and 4.2 Fe^{3+} ions occupying and the ($3a_{VI}$ + $6c_{VI}$ + $6c_{IV}$) sites, respectively.

It was previously reported that Co^{2+} ions prefer to reside in face sharing octahedral sites in the T block ($6c_{VI}$ and $3b_{VI}$) [2]. However, it was reported by others that Co^{2+} ions occupy $18h_{VI}$ and $6c_{IV}$ sites with marked preference for the $18h_{VI}$ octahedral sites [20]. Our results on the relative sub-spectral intensities of the three components indicate that the Co^{2+} ions are distributed almost randomly over the sites corresponding to these components. The relatively higher Co^{2+} ions for sites corresponding to the low field component could be interpreted as due to the preference of face-sharing sites due to the lower charge of this ion, which leads to lowering the electrostatic energy of the crystal structure.

Upon milling for 8 h, the relative intensities deviate appreciably from the above values and indicate that Co^{2+} ions are almost randomly distributed over octahedral sites in the T block and at the S-T interface.

Mössbauer spectra at room temperature for the samples with x = 1.0 ($Ba_2ZnCoFe_{12}O_{22}$) milled for different milling times are shown in Fig. 9. The spectra for the samples milled up to 4h were fitted with three sextet components as in the previous case, with the high field component (I) associated with Fe^{3+} ions at the ($6c_{IV}^{*}$ + $3b_{VI}$) sites, the middle component (II) with the $18h_{VI}$ site and the low field component (III) with the ($3a_{VI}$, $6c_{VI}$ and $6c_{IV}$) sites. The values of the hyperfine parameters for the samples are listed in Table 4. The appreciable drop in hyperfine field with Zn substitution is consistent with Zn^{2+} ions occupying $6c_{IV}^{*}$, thus weakening the $3b_{VI}$ - $6c_{IV}^{*}$ and $18h_{VI}$ - $6c_{IV}^{*}$ antiferromagnetic interactions. The relative intensities for the un-milled and milled samples are the same as in the previous samples with x = 0. This is an indication that a fraction of Zn^{2+} ions (with preference for tetrahedral coordination) occupy $6c_{IV}$* sites as an equal fraction of Co^{2+} ions were removed from $3b_{VI}$ sites and replaced by Fe^{3+} ions, maintaining the original relative intensity for the high field component. Similarly, a fraction of Zn^{2+} ions occupy $6c_{IV}$ tetrahedral sites as an equal fraction of Co^{2+} ions were removed from $6c_{VI}$ octahedral sites and replaced by Fe^{3+} ions [20], maintaining the relative intensity of the low field component.

TABLE 4. Room temperature Mössbauer parameters of $Ba_2ZnCoFe_{12}O_{22}$ sintered at T = 1100° C, hyperfine field B_{hf}, center shift CS, relative intensity of the spectral component and line width (W) for inner lines

Mössbauer Parameters	**T = 0.0 h**	**T = 1h**	**T = 2 h**	**T = 4h**	**T = 8h**
B_{hf} I(T) ± 0.5 T	46.1	45.7	45.2	45.4	45.2
B_{hf} II(T) ± 0.5 T	42.2	41.4	41.2	41.3	41.0
B_{hf} III(T) ± 0.5 T	38.7	38. 8	38.3	37.8	37.8
QQ(mm/s) ± 0.04 mm/s					0.08
CS I (mm/s) ± 0.02 mm/s	0.36	0.33	0.35	0.34	0.38
CS II (mm/s) ± 0.02 mm/s	0.4	0.24	0.33	0.33	0.36
CS III (mm/s) ± 0.02 mm/s	0.4	0.22	0.38	0.38	0.41
CS QQ(mm/s) ± 0.02 mm/s					0.42
Relative Intensity I (%)	20	20	20	20	25
Relative Intensity II (%)	45	45	45	45	35
Relative Intensity III (%)	35	35	35	35	25
Relative Intensity QQ (%)					15
Width I (W) (mm/s)	0.33	0.31	0.35	0.35	0.41
Width II (W) (mm/s)	0.51	0.43	0.50	0.50	0.46
Width III (W) (mm/s)	0.61	0.48	0.76	0.77	0.60
Width QQ (W) (mm/s)					3.06

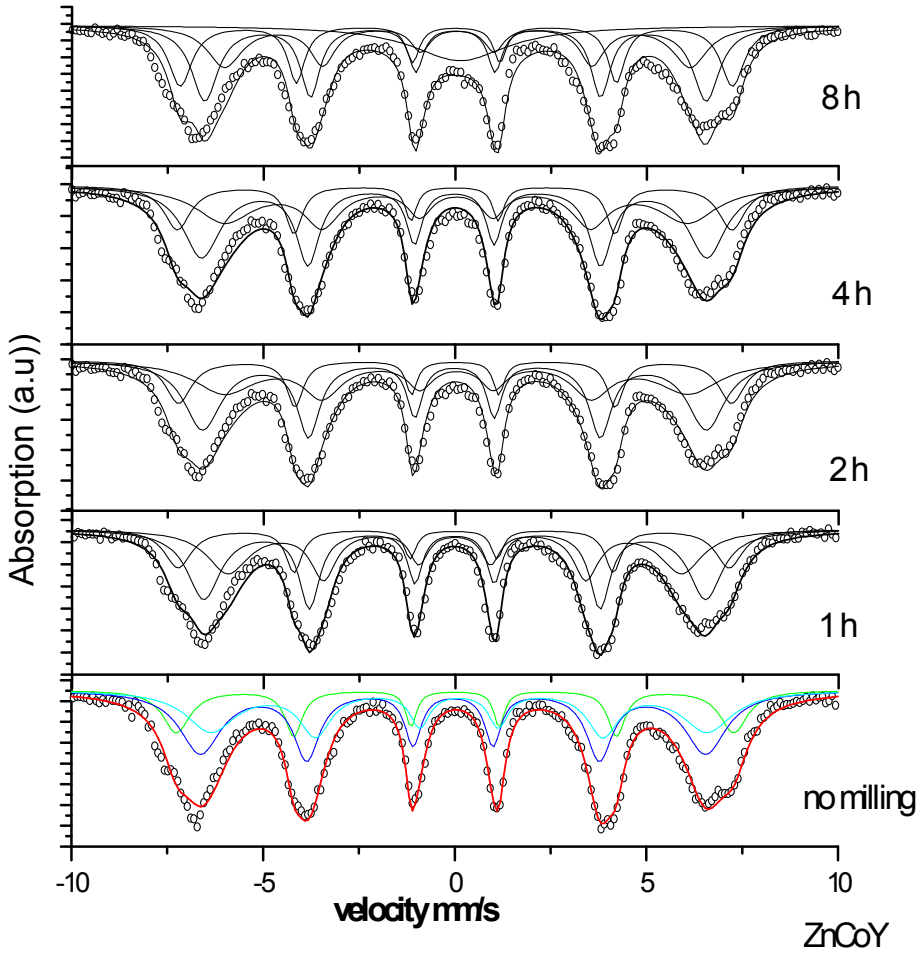

FIG. 9. Room temperature Mössbauer spectra of the sample $Ba_2ZnCoFe_{12}O_{22}$ sintered at temperature T = 1100°C and different milling times (T = 0, 1, 2, 4 and 8 h)

Mössbauer spectra at room temperature for the sample with x = 2 ($Ba_2Zn_2Fe_{12}O_{22}$) milled at different milling times (T = 0, 1, 2, 4 and 8 h) are shown in Fig. 9. The spectra were fitted with three magnetic sextets (except for the 8h milled sample which was fitted with three magnetic sextets and one quadrupole doublet). The corresponding hyperfine parameters are listed in Table 5. The relative intensity of 50% of the middle component indicates a complete filling of the $18h_{VI}$ sites by Fe^{3+} ions. However, the relative intensities (23% and 27%) of the other two components suggest that 0.24 Zn^{2+} ions in this sample occupy the $6c_{IV}$ sites and 1.76 ions occupy the $6c_{IV}^{*}$ sites resulting in the observed large drop of the intensity of the corresponding component down to 27%.

The values of B_{hf} for the three components (I, II and III) are plotted *versus* milling time for the samples with three Zn^{2+} concentrations (x = 0, 1 and 2) as shown in Figs. 11-13.

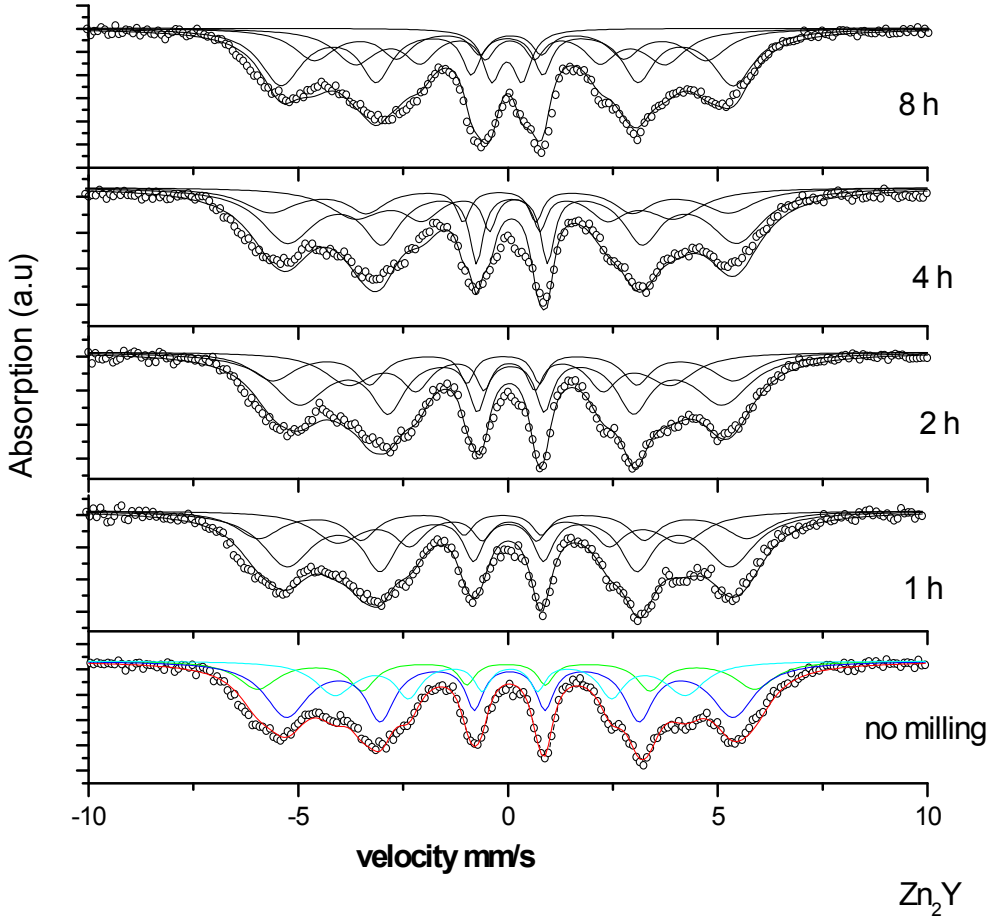

FIG. 10: Room temperature Mössbauer spectra of the sample $Ba_2Zn_2Fe_{12}O_{22}$ sintered at temperature T = 1100° C and different milling times (T = 0, 1, 2, 4 and 8 h)

Table 5: Room temperature Mössbauer parameters of $Ba_2Zn_2Fe_{12}O_{22}$ sintered at T = 1100 °C, hyperfine field B_{hf}, center shift CS, relative intensity of the spectral component and line width (W) for inner lines

Mössbauer Parameters	**T = 0.0 h**	**T = 1h**	**T = 2 h**	**T = 4h**	**T = 8h**
B_{hf} I(T) ± 0.5 T	37.1	36.5	34.4	34.3	33.8
B_{hf} II(T) ± 0.5 T	33.4	33.1	31.6	30.6	29.3
B_{hf} III(T) ± 0.5 T	26.2	25.7	24.1	23.9	23.2
QQ(mm/s) ± 0.04 mm/s					0.7
CS I (mm/s) ± 0.02 mm/s	0.31	0.23	0.24	0.25	0.33
CS II (mm/s) ± 0.02 mm/s	0.39	0.36	0.42	0.35	0.41
CS III (mm/s) ± 0.02 mm/s	0.4	0.38	0.39	0.41	0.4
CS QQ (mm/s) ± 0.02 mm/s					0.01
Relative Intensity I (%)	23	23	23	23	24
Relative Intensity II (%)	50	50	50	50	38
Relative Intensity III (%)	27	27	27	27	22
Relative Intensity (QQ) (%)					16
Width I (W) (mm/s)	0.45	0.53	0.42	0.39	0.51
Width II (W) (mm/s)	0.51	0.57	0.52	0.39	0.51
Width III (W) (mm/s)	0.46	0.55	0.44	0.39	0.51
Width QQ (W) (mm/s)					0.51

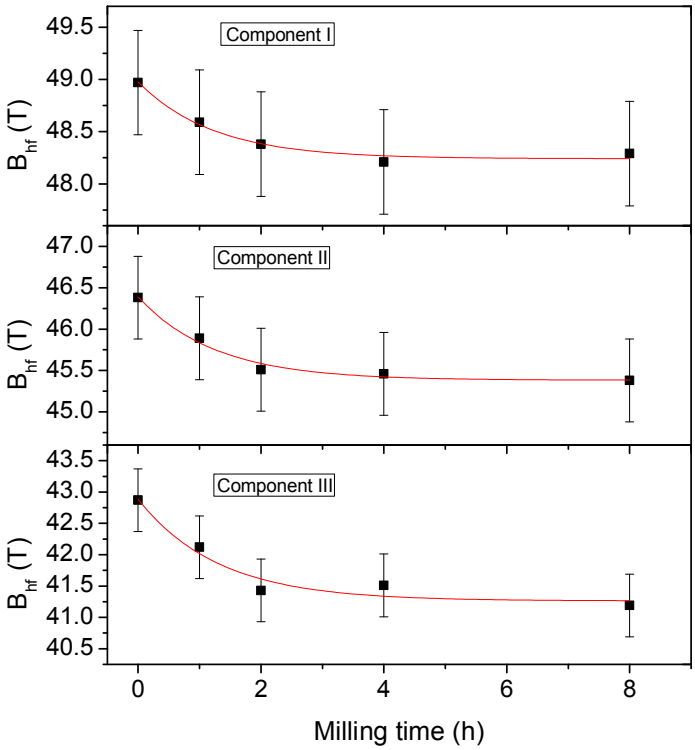

FIG. 11. The distribution of hyperfine parameters of $Ba_2Co_2Fe_{12}O_{22}$ with different milling times (T = 0, 1, 2, 4 and 8 h)

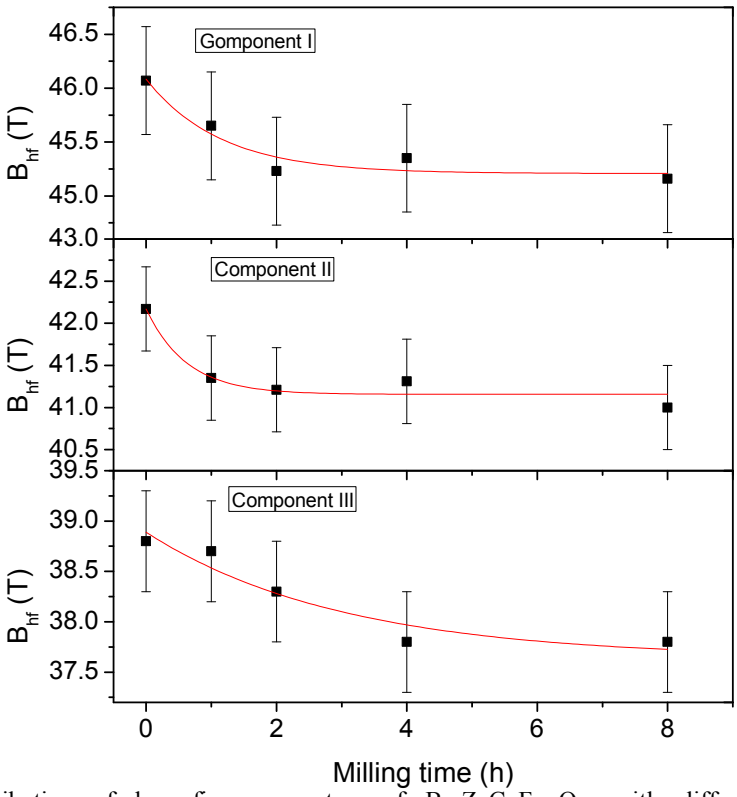

FIG.12. The distribution of hyperfine parameters of $Ba_2ZnCoFe_{12}O_{22}$ with different milling times (T = 0, 1, 2, 4 and 8 h)

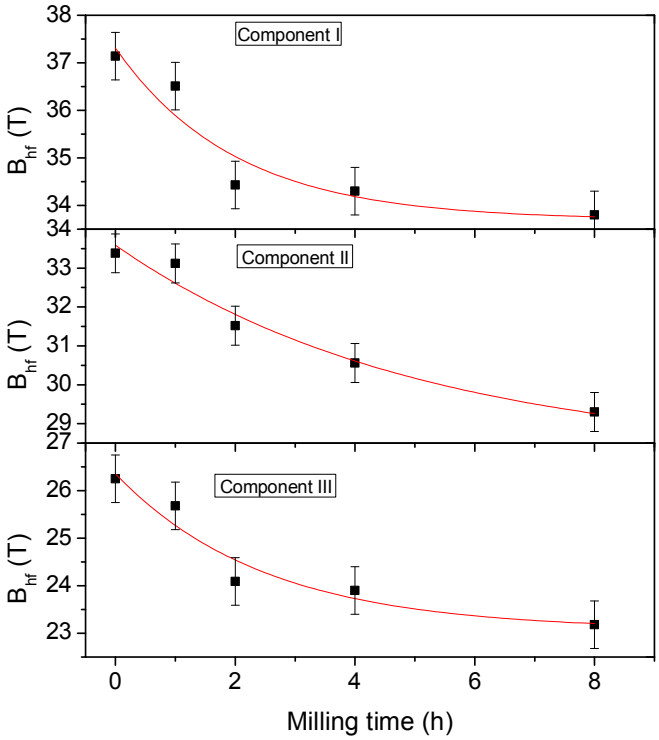

FIG. 13. The distribution of hyperfine parameters of $Ba_2Zn_2Fe_{12}O_{22}$ with different milling times (T = 0, 1, 2, 4 and 8 h)

The values of the hyperfine parameters for (x= 0, 1 and 2) are decreasing exponentially with increasing milling time. The spectrum broadening is due to the presence of distributions of hyperfine fields which is partially attributed to the statistical distribution of neighbors around the iron sites in the lattice. This effect is a consequence of the mechanical milling which results in crystal defects and could change the distribution of Fe^{3+} ions over the different sites of the hexaferrite lattice. Further, the increasing in milling time leads to the increase of the ratio of surface atoms to volume atoms. This results in the reduction of the hyperfine field of the magnetic components corresponding to surface atoms, resulting in asymmetric broadened lines. The new component represented with the quadrupole doublet in the spectrum of the 8 h milled sample is associated with small superparamgnetic grains resulting from the relatively long ball-milling time, as confirmed by XRD and SEM results.

Conclusions

The system $Ba_2Zn_xCo_{2-x}Fe_{12}O_{22}$ with (x = 0, 1 and 2) was prepared by sol-gel method. Milling in different parts of time (T = 0, 1, 2, 4 and 8h), XRD patterns indicate that the information and the analyses show that the system $Ba_2Zn_xCo_{2-x}Fe_{12}O_{22}$ with (x = 0, 1 and 2) is a Y-type hexaferrite and it maintains the pure Y-type with milling up to 8 h.

Mössbauer spectra at room temperature for all the samples $Ba_2Zn_xCo_{2-x}Fe_{12}O_{22}$ with x= 0, 1 and 2 sintered at T = 1100° C show a gradual change in the relative intensities and a drop in the hyperfine field as Zn^{2+} ions replacing Co^{2+} ions increase. The variations in relative intensities are consistent with Co^{2+} ions occupying octahedral sites and Zn^{2+} ions occupying tetrahedral sites.

The spectra of $Ba_2Zn_xCo_{2-x}Fe_{12}O_{22}$ with (x = 0, 1 and 2) were fitted by 3 sextet components up to 4 h milling. After milling for 8 h, Mössbauer spectra were best fitted with three magnetic sextets and a quadrupole component; which indicates the presence of superparamagnetic particles with largely reduced particle size in these samples. The B_{hf} values decrease gradually with milling time, which is a consequence of the decrease in particle sizes with increasing the milling time.

Acknowledgement

This work was supported by a generous grant from the Scientific Research Fund (SRF) in Jordan.

References

[1] Bai, Y., Zhou, J., Gui, Z. and Li, L., J. Magn. Magn. Mater., 250 (2002) 364.

[2] Albanese, G., J. Phys. C, 38 (1977) C1.

[3] Elahi, A., Ahmad, M., Ali, I. and Rana, M.U., Ceramics International, 39 (2013) 983.

[4] Pullar, R.C., Progress in Materials Science, 57 (2012) 1191.

[5] Ozgur, U., Alivov, Y. and Morkoc, H., J. Mater. Sci.: Mater. Electron, 20 (2009) 789.

[6] Ozgur, U., Alivov, Y. and Morkoc, H., J. Mater. Sci.: Mater. Electron, 20 (2009) 911.

[7] Khanduri, H., Chandra Dimri, M., Kooskora, H., Heinmaa, I., Viola, G., Ning, H., Reece, M.J., Krustok, J. and Stem, R., J. Appl. Phys., 112 (2012) 073903.

[8] Albanese, G., Asti, G. and Lamborizio, C., J. Appl. Phys., 39 (1968) 1198.

[9] Smit, J. Wijn, H.P.J., Ferrites. Phillips Technical Library, Eindhoven; 1959.

[10] Awawdeh, M., Bsoul, I. and Mahmood, S.H., J. Alloys Compd., 585 (2014) 465.

[11] Bsoul, I., Mahmood, S.H., Lehlooh, A. and Al-Jamel, A., J. Alloys Compd., 551 (2013) 490.

[12] Alsmadi, A.M., Bsoul, I., Mahmood, S.H., Alnawashi, G., Prokes, K., Seimensmeyer, K., Klemke, B. and Nakotte, H., J. Appl. Phys., 114 (2013) 243910.

[13] Mahmood, S., Dushaq, G., Bsoul, I., Awawdeh, M., Juwhari, H., Lahlouh, B. and AlDamen, M., J. Appl. Math. Phys., 2 (2014) 77.

[14] Bsoul, I. and Mahmood, S.H., Jordan J. Phys., 2 (2009) 171.

[15] Zhang, W., Bai, Y., Han, X., Wang, L., Lu, X. and Qiao, L., J. Alloys Compd., 546 (2013) 234.

[16] Deriu, A., Licci, F., Rinaldi, S. and Besagni T., J. Magn. Magn. Mater., 22 (1981) 257.

[17] Mahmood, S.H., Jaradat, F.S., Lehlooh, A. and Hammoudeh, A., Ceram. Int., 40 (2014) 5231.

[18] Nakamura, S., Tsunoda, Y. and Fuwa, A., Hyperfine Interact. (2011) (doi: 10.1007/s10751-011-0486-2).

[19] Campbell, S.J., Wu, E., Kaczmarek, W.A. and Jayasuriya, K.D., Hyperfine Interact., 92 (1994) 933.

[20] Bierlich, S. and Topfer, J., J. Magn. Magn. Mater.,(2012)(doi:10.1016/j.mmm.2012.01.006.)

الخلاصة

مما سبق، نستخلص أن عدد الجسيمات المنبعثة في الاتجاه الأمامي يزداد مع زيادة كتلة القذيفة وطاقتها، كما أن انبعاث الهادرونات النسبية في الاتجاه الخلفي نصف الكروي مستقل عن طاقة القذيفة. أما توزيعة التعددية للجسيمات الرذاذية المشحونة فستصبح أعرض في حالة الاتجاه الامامي نصف الكروي من الاتجاه الخلفي.

وعند دراسة قيم النسبة (N_S^F/N_S^B)، فقد وجدنا أنها تزداد مع زيادة كتلة المقذوف عند طاقة المقذوف نفسها.

وأخيراً فعلاقات التعددية في الاتجاهين خطية، ودراسة هذه العلاقات يوضح اعتماد N_S^F القوي على N_h, N_g, N_b.

المراجع

[1] Khan, M.S., Khushnood, H., Ansari, A.R., Nasr, M.A. and Irfan, M., 109A(12) (1996) 1623.

[2] Dong-Hai, Z., Hui-Hua, Z., Fang, L., Chun-Le, H., Hui-Ming, J., Xue-Qin, L., Zhen-Yu, L. and Jun-Sheng, L., J. Chin. Phys., 09 (2006) 1987.

[3] El-Nadi, M., Abdesalam, A., El-Nagdy, M.S., Shaat, E.A., Ali-Mossa, N., Abou-Moussa, Z., Kamel, S., Rashed, N., Hafiz, M.E. and Badawy, B., Proceedings of ICRC. (2001) 1366.

[4] Ahmad, N., Ahmad, S., Khan, M.M., Zafar, M. and Irfan, M., International Journal of Modren Physics E, (2005) 895.

[5] Abdelsalam, A., Shaat, E.A., Ali-Mossa, N., Abou-Mousa, Z., Osman, O.M., Rashed, N., Osman, W., Badawy, B.M. and El-Falaky, E., J. Phys. G: Nucl. Part. Phys., 28 (2002) 1375.

[6] El-Nadi, M., Abdelsalam, A. and Ali-Mosa, N. et al., Euro. J. Phys., (1998) 183.

[7] El-Naghy, A., Sadek, N.N. and Mohery, Nuovo Cim. A, 110 (1997) 125.

[8] Dipak, G., Jaya, R. and Ranjan, S., Can. J. Phys., 67 (1989) 115.

[9] Tauseef, A. and Irfan, M., Phys. Rev. C, 46 (1992) 1483.

[10] EI-Nadi, M., Ali-Mossa, N. and Abdelsalam, A., Nuovo Cimento, 110 (1998) 1255.

[11] El-Nadi, M., Abdelsalam, A. and Ali-Mossa, N., Int. J. Mod. Phys. E, 3 (1994) 811.

[12] El-Nadi, M., Abdelsalam, A. and Ali-Mossa, N., Radiat. Phys. Chem., 47 (1996) 681.

3. النسب الأمامية والخلفية

في جدول (6) تتضح نسبة الجسيمات الأمامية إلى الخلفية لكل من الجسيمات الرذاذية والرمادية $(F/B)_{s,g}$، عند حجوم مختلفة للهدف N_h (1-7)، (8-17)، (18-27) و$N_h \geq 28$)، لتفاعلات الكربون مع نوى المستحلب,بالإضافة لعدة قذائف اخرى (^{28}Si,^{22}Ne,^{32}S) عند الطاقة نفسها [12,11,10,5].

نرى من البيانات أن قيم $(F/B)_s$ تتناقص بسرعة مع زيادة حجم الهدف (قيم N_h)، أما الجسيمات الرمادية فتتثبت هذه النسبة لها في المنطقة (N_h> 7) عند القيمة (3.3). كذلك تتضح في هذا الجدول حقيقة زيادة الجسيمات الامامية الناتجة مع زيادة العدد الكتلي للمقذوف، كما تزداد النسبة $(F/B)_s$ كذلك، وهذا نتيجة لزيادة عدد الجسيمات الرذاذية مع حجم القذيفة.

الشكل (6)، رسمت العلاقة لنسبة الإتجاهين للجسيمات الرذاذية كدالة للجسيمات كثيفة التأين (N_h)، ويبدو جليا أن النسبة (N_s^B/N_s^F) تتناقص مع زيادة قيم (N_h) للجسيمات الرذاذية. وقد توصل (khan, M.S. et al.)[1] إلى هذه النتيجة أيضاً.

الجدول (6): النسب الأمامية-الخلفية لقذائف مختلفة عند فترات N_h مختلفة

Projectile		$N_h \geq 28$	N_h(18-27)	N_h (8-17)	N_h (1-7)	Ref
	$(F/B)_s$	49.57	22.41	15.09	6.47	Present Work
^{12}C	$(F/B)_s$	44.20	27.00	22.50	18.5	[5]
	$(F/B)_g$	4.08	3.41	3.20	3.30	[10]
^{22}Ne	$(F/B)_s$	48.04	27.54	21.21	16.58	[11]
	$(F/B)_g$	4.80	3.30	3.10	2.90	
^{28}Si	$(F/B)_s$	62.04	44.04	23.64	17.88	[12]
	$(F/B)_g$	4.40	3.50	2.90	3.10	
^{32}S	$(F/B)_s$	95.50	32.53	20.20	21.47	[5]
	$(F/B)_g$	6.70	3.51	3.06	4.13	

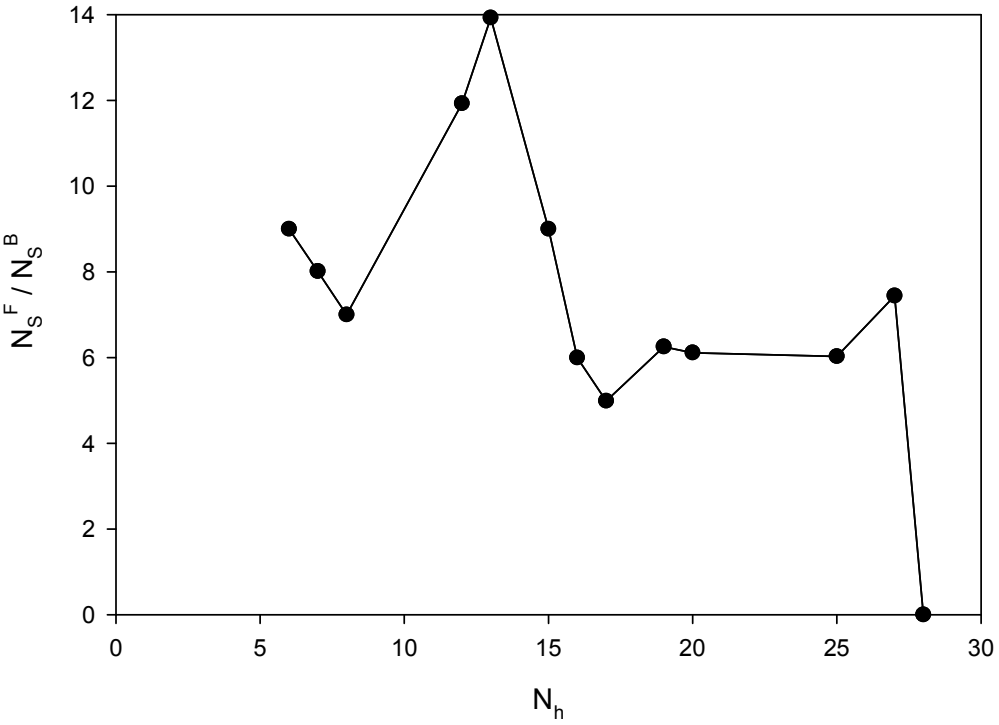

الشكل (6): نسبة الاتجاهين للجسيمات الرذاذية كدالة للجسيمات كثيفة التأين

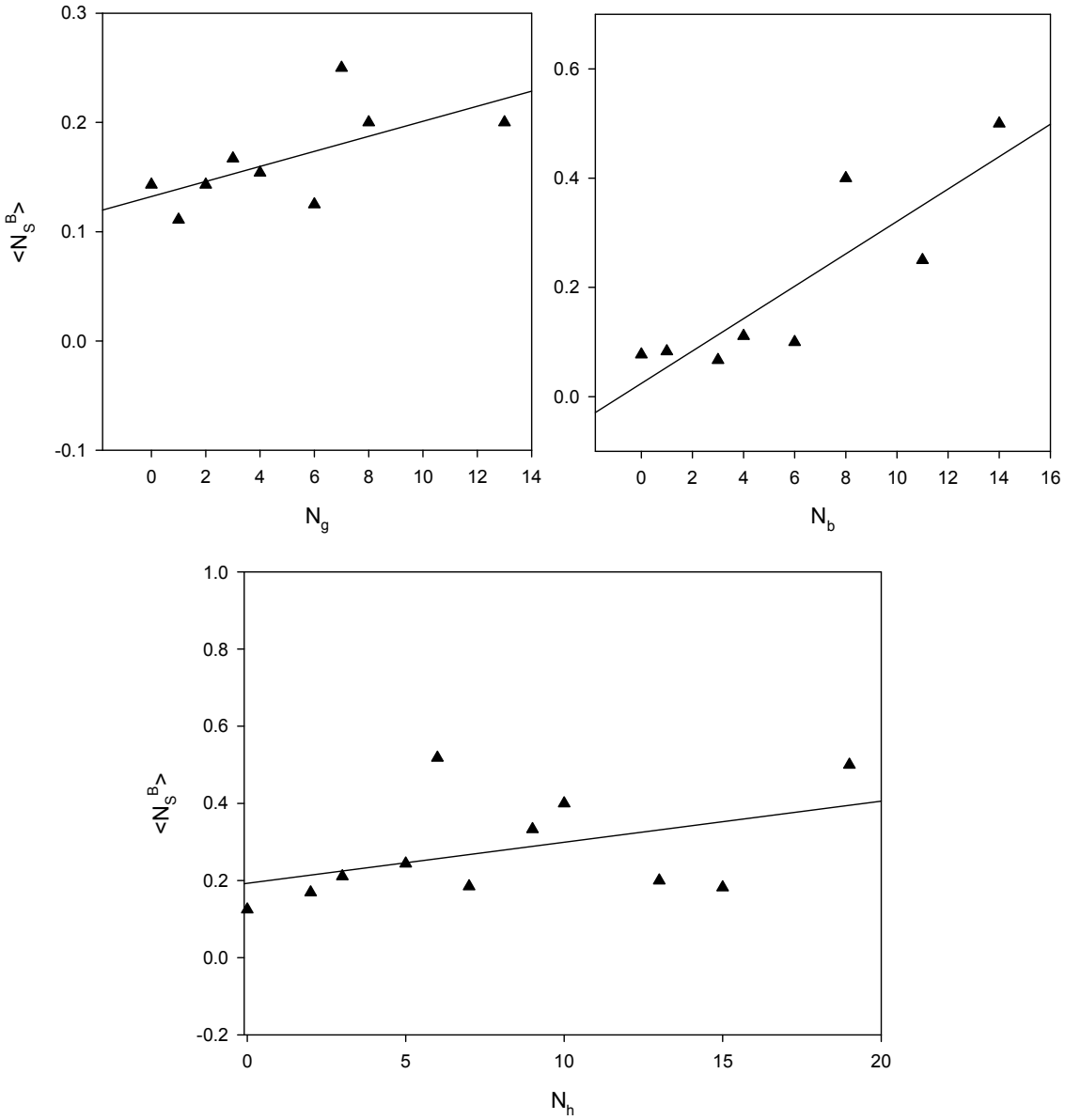

الشكل (5): العلاقة بين متوسط تعددية الجسيمات الرذاذية في الاتجاه الخلفي والتعدديات المختلفة

الجدول (5): قيم البارامترين a وb لتفاعلات الكربون مع المستحلب عند كمية حركة للشعاع قدرها 4.5 $AGeV/c$

$Corelations$	b	a
$< N_S^F > \ vs \ N_b$	0.79	0.0076
$< N_S^F > \ vs \ N_g$	0.69	0.022
$< N_S^F > \ vs \ N_h$	0.73	0.0082
$< N_S^B > \ vs \ N_b$	0.024	0.029
$< N_S^B > \ vs \ N_g$	0.132	0.0069
$< N_S^B > \ vs \ N_h$	0.193	0.0106

ارتباطات التعددية في الإتجاهين موضحة في الشكلين (4) و (5). وقد تمت ملاءمة البيانات التجريبية للشكلين السابقين بالمعادلة:

$$N_s^i = aN_j + b, i \neq j \quad (3)$$

حيث i ترمز إلى الاتجاه الخلفي (B)، أو الأمامي (F)، بينما تشير (j)إلى الجسيمات الرمادية أو السوداء أو كثيفة التأين. كما أن قيم البارامترين a وb موضحة في الجدول (5). ويتضح من هذين الشكلين أن معدل تعددية الجسيمات الرذاذية في الاتجاهين يزداد مع زيادة قيم (N_h, N_b, N_g)، مع اعتماد أقوى لهذه الجسيمات للاتجاه الأمامي بشكل خاص.

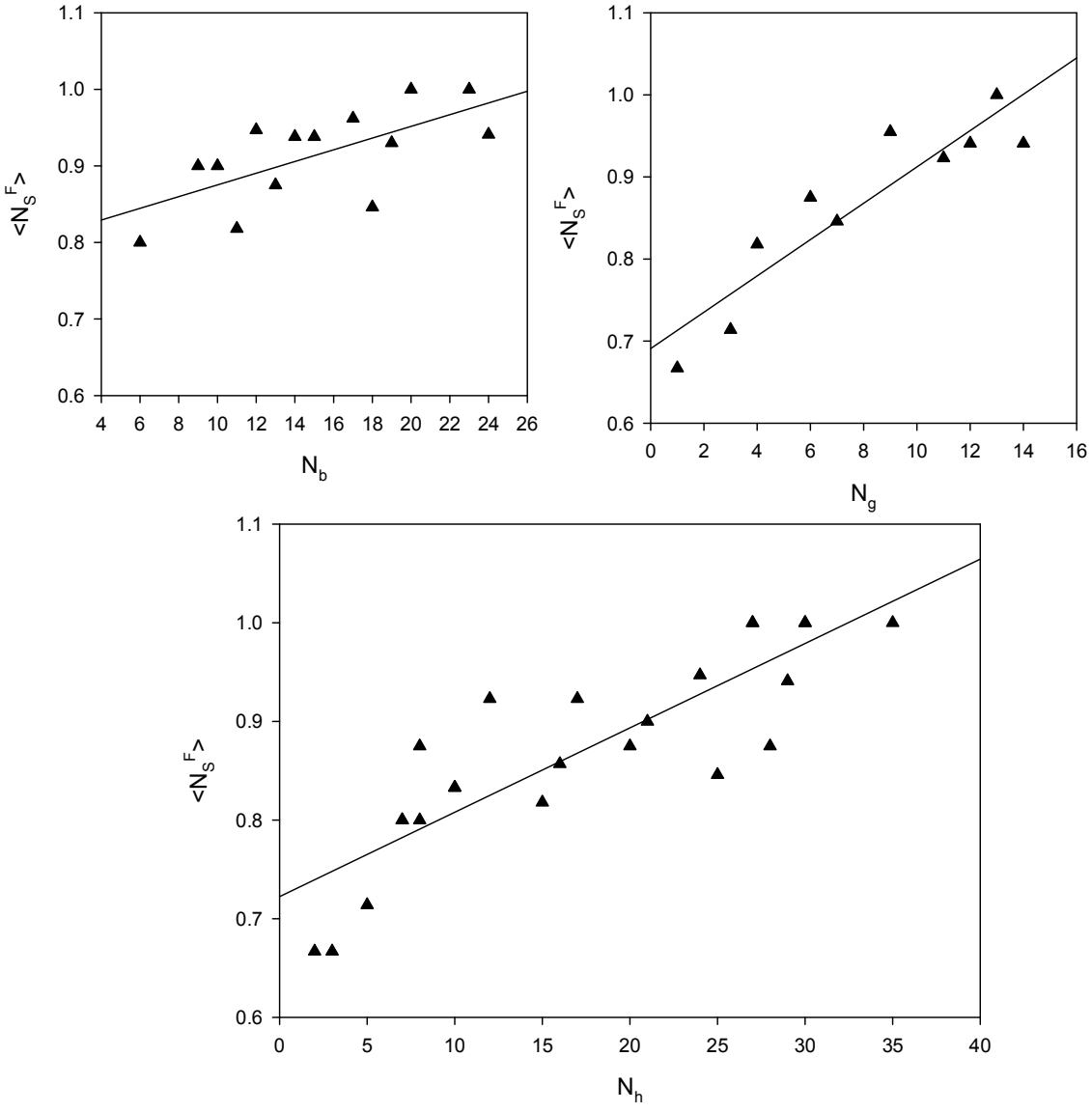

الشكل (4): متوسط تعددية الجسيمات الرذاذية في الاتجاه الأمامي وتعدديات الجسيمات المختلفة

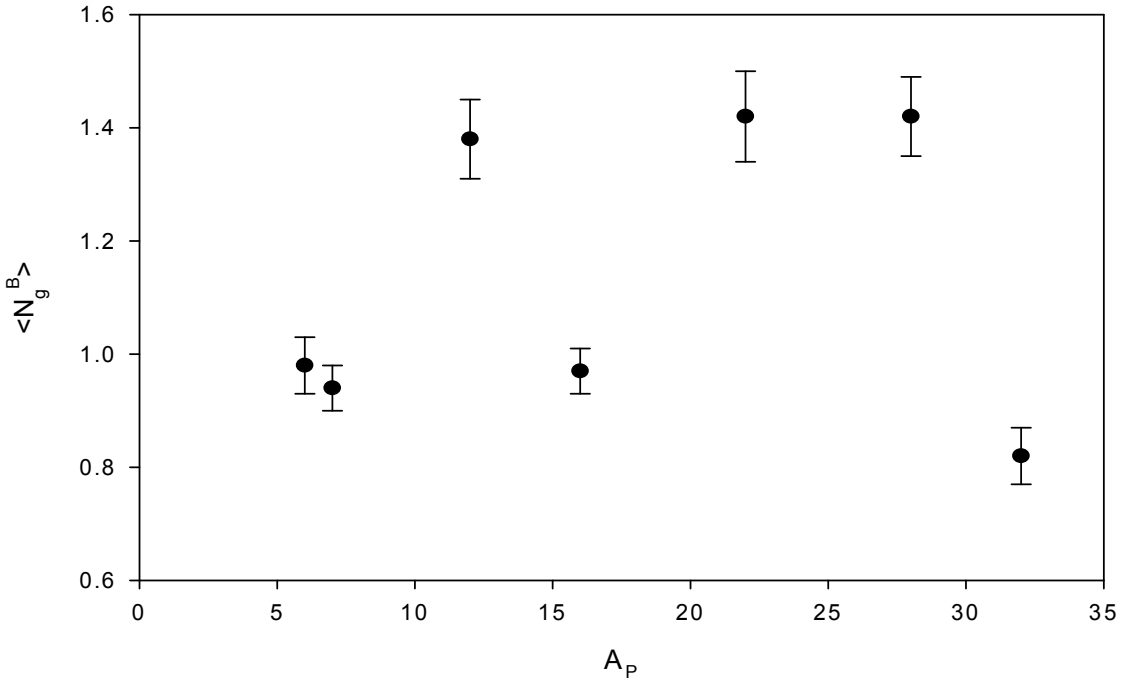

الشكل (3- ب): العلاقة بين العدد الكتلي للقذيفة ومتوسط عدد الجسيمات الرمادية في الاتجاه الخلفي

2 ـ ارتباطات التعددية

تعتبر دراسة العلاقة بين تعدديات الأنواع المختلفة من الجسيمات الأمامية والخلفية من أهم مصادر المعلومات عن ميكانيكية إنتاج الجسيمات في الاتجاهين. الجدول (4) يوضح قيم متوسط عدد الجسيمات الرذاذية المشحونة في الاتجاهين، والنسب الامامية والخلفية وبارامتر التماثل (A) المعرف بالمعادلة:

$$A = \frac{N_S^F - N_S^B}{N_S^F + N_S^B} \qquad (2)$$

الجدول (4): قيم متوسطات تعددية الجسيمات الرذاذية المشحونة في الاتجاهين والنسب المختلفة لها

	$^{12}C(8)$	$^{12}C(9)$	$^{28}C(8)$	$^{12}C(Present\ work)$
$< N_S^F >$	7.38	7.10	10.95	8.62
$< N_S^B >$	0.29	0.5	0.29	0.61
N_S^F / N_S^B	25.39	14.20	37.76	14.24
A	0.92	0.86	0.95	0.87
$< N_S^B > N_S^F >$	0.039	—	0.026	0.070
$< N_S^B > / < N_S >$	0.038	0.067	0.026	0.066
$< N_S^F > / < N_S >$	0.962	0.934	0.971	0.934

كما أدرجنا ضمن هذا الجدول القيم المناظرة لدراسات اخرى [9,8]، ونلاحظ التوافق الجيد بين النتائج.ونلاحظ منها جميعاً أن معدل تعدديات الجسيمات الرذاذية في الإتجاه الأمامي أكبر منها في الاتجاه الخلفي، وهذا يعني أن احتمالية الانبعاث الأمامي أعلى وأوفر حظاً من احتمالية الانبعاث الخلفي. كما نلاحظ أن قيمة البارامتر(A) لا تعتمد على كتلة القذيفة.

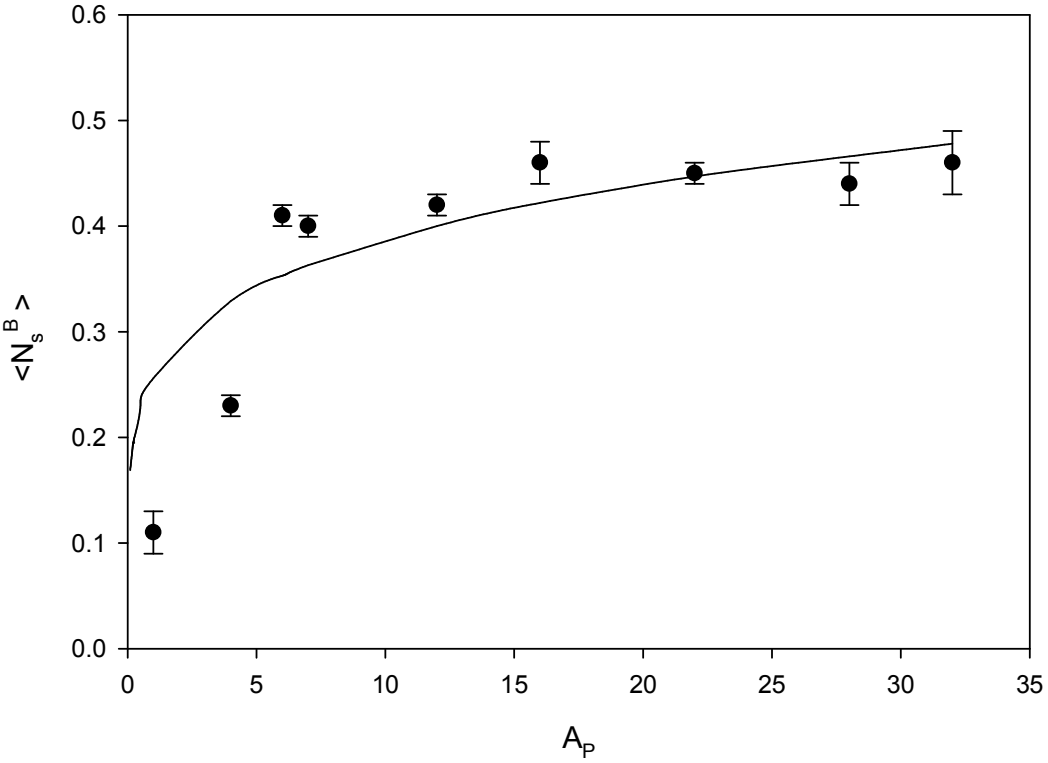

الشكل (2- ب): العلاقة بين العدد الكتلي للقذيفة ومتوسط عدد الجسيمات الرذاذية في الاتجاه الخلفي

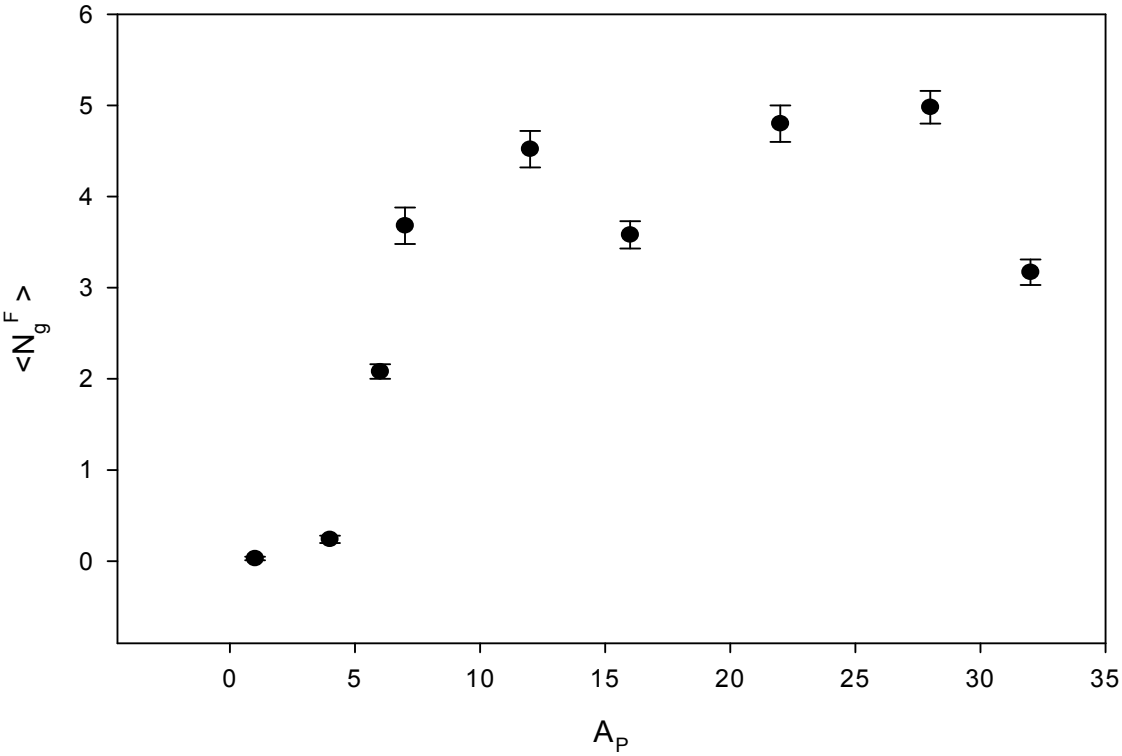

الشكل (3- أ): العلاقة بين العدد الكتلي للقذيفة ومتوسط عدد الجسيمات الرمادية الاتجاه الأمامي

حيث B,F تعني الاتجاهين الأمامي والخلفي على الترتيب، j=s,g.

تم حساب قيم α, β في الاتجاهين للجسيمات الرذاذية والرمادية بواسطة طريقة المربعات الصغرى، وكانت القيم كما هي موضحة في الجدول (3)، ومن ذلك يلاحظ أن $\langle N_S^F \rangle$ تزداد مع كتلة القذيفة بشكل اوضح مما هو عليه في $\langle N_S^B \rangle$.وقد لوحظ هذا أيضاً من (M.El-nadi)[3].

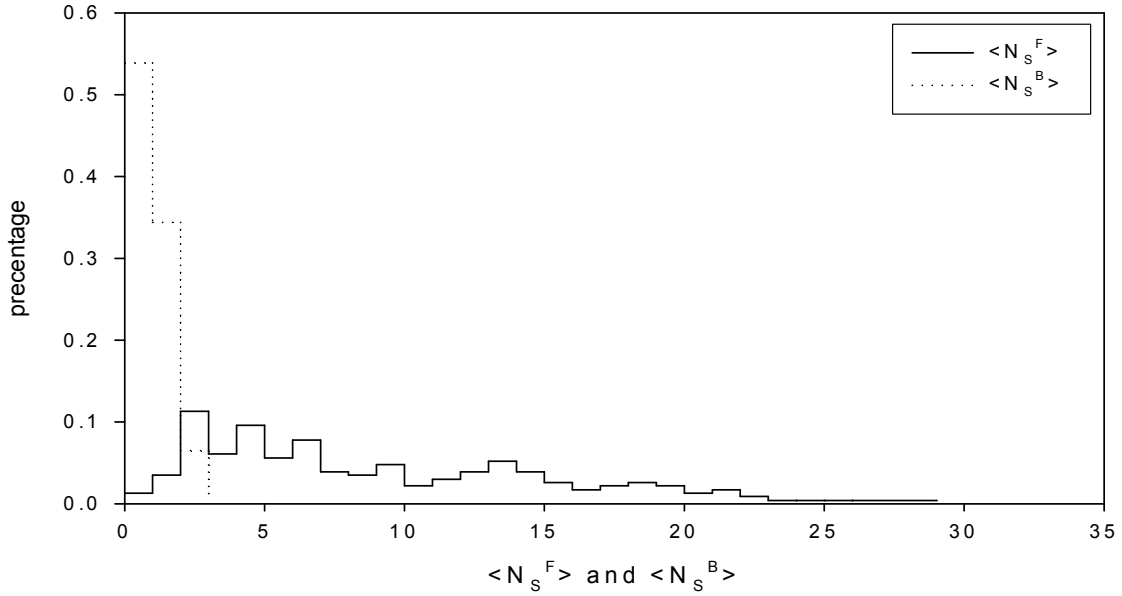

الشكل (1): تعددية الجسيمات الرذاذية في الاتجاهين الأمامي والخلفي في تفاعلات الكربون - المستحلب عند طاقة4.5 AGeV/c .

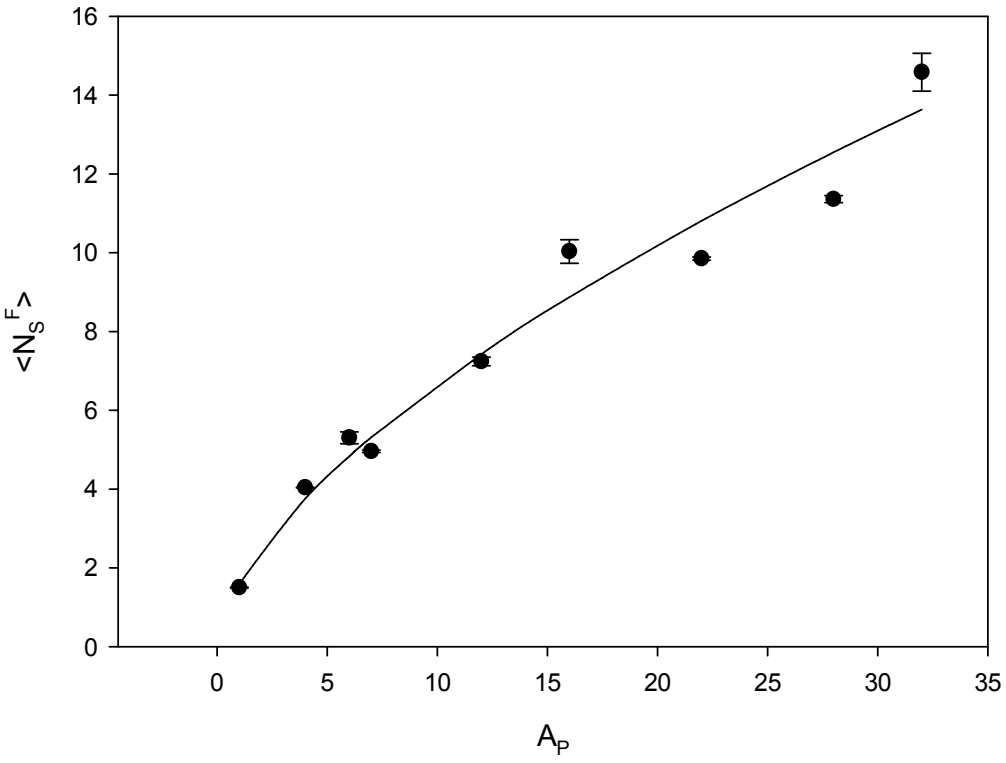

الشكل (2- ا): العلاقة بين متوسط الجسيمات الرذاذية في الاتجاه الامامي والعدد الكتلي للقذيفة

أما تمييز الجسيمات الأمامية والخلفية فيكون بالشكل $N_s = N_s^F + N_s^B$

للجسيمات الرذاذية، حيث N_s^F هي عدد الجسيمات الرذاذية، في الاتجاه الأمامي، وN_s^B عددها في الاتجاه الخلفي، وكذلك $N_g = N_g^F + N_g^B$, $N_b = N_b^F + N_b^B$ للجسيمات الرمادية والسوداء بالكيفية نفسها وعلى التوالي.

النتائج التجريبية والمناقشة

1. متوسط التعددية للجسيمات المشحونة النسبية الناتجة في الاتجاهين الأمامي والخلفي

وضحنا هذه المتوسطات في الجدول (2) لقذائف مختلفة. وواضح أن قيمة $< N_s^B >$ تبقى ثابتة عند قيمة (0.4) تقريباً مع أخطاء تجريبية صغيرة بغض النظر عن كتلة القذيفة، وهذا نتيجة لأن الهادرونات المنبعثة في الاتجاه الخلفي تعتمد على عدد النيوكليونات المتفاعلة من القذيفة، بينما تزداد $< N_s^F >$ مع زيادة العدد الكتلي للقذيفة (A_p). ويتضح من الجدول تطابق نتائج الدراسة الحالية بشكل جيد مع نتائج الابحاث الاخرى [7,6,4]. أما للقذيفة الواحدة، فمن الواضح من الجدول أن إنتاج الجسيمات في الاتجاه الامامي يزداد بزيادة طاقة القذيفة ولا تأثير يذكر على الجسيمات في الاتجاه الخلفي.

الجدول (2): متوسطات التعددية للجسيمات الرذاذية في الاتجاهين الأمامي والخلفي لقذائف مختلفة

Type of interaction	Incident energy per nucleon(GeV)	$< N_s^B >$	$< N_s^F >$	Ref.
$^6Li - Em$	2.2	0.29±0.01	3.86±0.10	
$^6Li - Em$	3.7	0.41±0.02	——	[6]
$^{12}C - Em$	3.7	0.42±0.01	7.11±0.22	
$^{12}C - Em$	4.5	0.69±0.04	7.24±0.11	Present Work
$^{22}Ne - Em$	3.3	0.45±0.01	9.85±0.04	[6]
$^{22}Ne - Em$	4.1	0.40±0.02	9.71±0.23	[7]
$^{28}Si - Em$	3.7	0.44±0.02	11.36±0.09	[6]
$^{28}Si \quad Em$	14.5	0.38±0.06	20.50±0.52	[4]
$^{28}Si - Em$	4.5	0.35±0.02	11.43±0.09	[7]

الجدول (3): قيم α وβ في الاتجاهين الأمامي والخلفي للجسيمات الرذاذية والرمادية

Particles	s particlec		g particles	
	F	B	F	B
α	0.62	0.18	1.42	0.009
β	1.59	0.26	0.066	0.94

في الشكل (1)، رسمنا التعددية للجسيمات الرذاذية في الاتجاهين، لتصادمات الكربون مع المستحلب. ونلاحظ فيه أن توزيعة الجسيمات الأمامية أكثر انبساطاً من الجسيمات الخلفية. وقد لوحظ هذا السلوك أيضاً من (N.Ahmad)[4].

وفي الشكلين (2) و (3)، رسمت العلاقات بين A_p وكل من متوسط التعددية للجسيمات الرذاذية والرمادية في كلا الاتجاهين لعدة قذائف نووية، حيث تمت ملاءمة البيانات بواسطة العلاقة:

$$< N_j^{F,B} > = \beta_j^{F,B} A_p^{\alpha_j^{F,B}} \qquad (1)$$

أما انبعاث الهادرونات السريعة والنسبية (البايونات) من النواة في الاتجاه الخلفي نصف الكروي (Backward Hemisphere,BHS)، فيعد من أهم الخواص في تفاعلات نواة- نواة (A-A) وهادرون – نواة (h-A)، وتنبعث هذه الأهمية من أن إنتاج الهادرون في الاتجاه الخلفي في التصادمات الحرة لنيوكليون - نيوكليون غير ممكن كينماتيكياً، وتبدو ميكانيكية هذا الإنتاج الغريب أشبه بما ينتج عن التعنقد (Clustering).

دراسة هذا الانبعاث تزودنا بمعلومات عن تأثيرات نووية أخرى كتفاعلات الهادرونات من منطقة التفاعل الابتدائية مع المادة النووية المحيطة، وحركة النيوكليونات الداخلية بداخل النواة وارتباطها بالمدى القصير بين النيوكليونات [2].

اقترح بالدن وآخرون (Baldin et al. 1978) أن حركة فيرمي البسيطة لايمكن حسابها لإنتاج هذه الهادرونات في الإتجاه الخلفي، وذكروا أن الميكانيكية السائدة لهذا الإنتاج هي تفاعل بين النيوكليونات الناتجة من القذيفة وكتل النيوكليونات المتعددة في الهدف، وأن هذه الميكانيكية ترجع إلى إنتاج تراكمي (Cumulative production) (Baldin, 1980)[3]؛ إذ تبدو نواة الهدف كجسم ممتد معطية فرصة استثنائية لنشوء فضاء زمني(Time-Space) لعمليات انتاج الجسيم المتعدد [2]. وحتى الآن لا توجد نظرية واضحة تشرح خصائص انبعاث الهادرون في الاتجاه الخلفي، بينما تنجح بعض النماذج في شرح كيفية إنتاج الجسيم المتعدد وفهم ظاهرة التدفق (Cascading) وإعادة الاستطارة (Rescattaring) للجسيمات في الجزء المساهم (Participant Part) من النواة في تصادمات (A-A) النسبية [4].

مصدر البيانات التجريبية وطريقة تحليل

في هذه الورقة البحثية، قمنا بتحليل (490) حدثاً، نتجت من تعريض كومة المستحلب النووي، من نوع (NIKFI-BR-2)، لشعاع عمودي من نوى الكربون، بطاقة $4.5 GeV/c$ لكل نواة. والجدول (1) يوضح التركيب الكيميائي لهذا النوع من المستحلب.

الجدول (1): التركيب الكيميائي لشريحة المستحلب من النوع NIKFI-BR-2

$Element$	^{1}H	^{12}C	^{22}Ne	^{16}O	^{80}Br	^{108}Ag
$No\ of \frac{atoms}{cc} x10^{22}$	3.150	1.410	0.395	0.956	1.028	1.028

مصدر هذه البيانات هومعجل دوبنا في روسيا (Dubna Synchrophastron,Russia). وباستخدام (Nikon Microscope) متحرك بقوة تكبير 40 x Objective وEye-piece15x، التقطت الآثار الابتدائية على مسافة 3 mm من حافة الدخول إلى الكومة وجرى تتبعها للخلف للتأكد من أنها لم تكن ناتجة من تفاعل سابق.

تم فحص الأحداث باستخدام عدسات ذات قوة تكبير(15xEye-pieces) و (95xoil Immersion objectives)، وبواسطة نظرية المسح السريع على طول الأثر في اتجاه القذيفة والمسح البطيْ في الاتجاه المعاكس. كما تم اختيار الأحداث وفق المعيار الآتي: 1. كل آثار الشعاع بزوايا قذف أقل من 3° مع الإتجاه الرئيسي الإبتدائي، تم استبعادها. 2- الأحداث الناتجة لمسافة $30 \mu m$ من قمة شرائح المستحلب أو قاعها ، لم تؤخذ في التحليل.

كما صنفت الآثار كلاسيكياً،طبقاً للمعايير المستخدمة في طريقة المستحلب النووي إلى الأصناف الآتية:

1- الآثار الرذاذية (Shower Tracks) وهي بايونات مشحونة بسرعة نسبية $(\beta \geq 0.7)$ وتاين نسبي $(I/I_0<1.4)$.

2- الآثار الرمادية (Grey Tracks)، وهي على الأغلب بروتونات ذات طاقة حركية (26-400MeV) وتأين نسبي $(I/I_0 > 1.4)$.

3. الآثار السوداء (Black Tracks)، وهي جسيمات ذات مدى قصير في المستحلب ($R\leq 3mm$) وطاقاتها الحركية اقل من ($26\ MeV$).

تعدديات الآثار السابقة هي على التوالي: (N_s, N_g, N_b)، كما تعرف الآثار كثيفة التأين بأنها مجموع $(N_h=N_g+N_b)$.

المجلد 7، العدد 2، 2014. ص ص. 111- 120

المجلة الأردنية للفيزياء

ARTICLE

خصائص الجسيمات المنبعثة في الاتجاهين الامامي والخلفي في تصادمات الكربون مع المستحلب النووي عند الطاقة العالية

حليمة الهادي الجمل ومصطفى عبد السلام بن نصر بعيو
قسم الفيزياء، كلية العلوم، جامعة مصراتة، مصراتة، ليبيا.

Received on: 17/7/2013; *Accepted on: 30/3/2014*

الملخص: أجريت هذه الدراسة لمعرفة خصائص الجسيمات النسبية المنبعثة في الاتجاهين الأمامي ($\theta_{lab} < 90°$) والخلفي ($\theta_{lab} \geq 90°$) لتفاعل نوى الكربون مع المستحلب النووي عند كمية حركة شعاع قدرها $4.5\frac{GeV}{c}$ لكل نيوكليون.
تمت مناقشة النتائج المتعلقة بمتوسطات الجسيمات الرذاذية والرمادية، وارتباطات هذه التعدديات. ووجد أن متوسط القيم لتعدديات الجسيمات الأمامية تعتمد اعتماداً قوياً على العدد الكتلي للقذيفة وطاقتها. كما وجد أن النسبة (N_s^F/N_s^B) للجسيمات الرذاذية تزداد مع زيادة كتلة القذيفة وتتناقص مع زيادة حجم الهدف. أما النسبة نفسها للجسيمات الرمادية (N_g^F/N_g^B) فهي تقريباً ثابتة في المنطقة ($N_h > 7$).

Features of the Forward-Backward Particles in the Collisions of Carbon with Nuclear Emulsion at High Energy

Halima Al-Jamal and Mustafa Bayio
Physics Department, Faculty of Science, Misrata University, Misrata, Libya.

Abstract: Experimental data on relativistic (shower) and fast (grey) hadrons emitted in the forward and backward hemispheres ($\vartheta < 90°, \theta \geq 90°$), (FHS,BHS), in the collision of ^{12}C beam with emulsion nuclei at 4.5A*GeV/c* are presented and analyzed. The correlations between multiplicities of shower particles are also investigated. The mean values of the multiplicities of the produced forward particles are strongly dependent on the projectile mass number, A_p, and its energy while those of the backward ones are nearly independent of A_p. Finally, the ratio (N_s^F/N_s^B) is found to increase with increasing the projectile mass and decrease rapidly with increasing the target size (N_h-value), while (N_g^F/N_g^B) seems to exhibit a limited behavior in the region of $N_h > 7$.
Keywords: Forward hemisphere; Backward hemisphere; Nuclear emulsion; Collisions at high energy.
PACS: 25.75.-q

المقدمة

عند اصطدام النوى المعجلة لطاقات عالية، يصعب التكهن بما ستؤول إليه هذه النوى بعد الاصطدام. فقد تفقد هذه النوى هويتها تماماً، وغالباً ما تنتج جسيمات جديدة بطاقات مختلفة وزخم مختلف، وبزوايا انبعاث متعددة.

ومن الظواهر الشيقة انبعاث الجسيمات في مثل هذه التفاعلات في الاتجاهين الأمامي والخلفي. وخصائص هذا الانبعاث توضح الميكانيكية التي يتأين بها الهادرون للحالة النهائية للجسيمات الرذاذية المشحونة في الاتجاهين [1].

Corresponding Author: Halima Al-Jamal **Email**: mahasen.alhadi@yahoo.com

المراجع

[1] Bhanjo, R. et al., Nuclear Physics A, 411 (1983) 507.

[2] Mocsy, A., Petreczky, P. and Strickland, M., arXiv:1302. 2180vl[hep-ph]8 Feb. 2013.

[3] Gosset, J., Gutbrod, H.H., Meyer, W.G., Poskanzer, A.M., Sandval, A., Stock, R. and West, G.D., Fall. Phys. Rev. C, 16 (1977) 629.

[4] Bjorken, J.D., Phys. Rev. D, 27 (1983) 140.

[5] Adamovich, M.I. et al., Sov. J. Nucl. Phys., 29 (1979) 42.

[6] Rosu, H.C., Acta Physica Polonica B, 25(10) (1994).

[7] Bradt and Peters 1950, Daniel and Durgaprusad 1962, Cleghorn et al. 1972.

[8] H. Khushnood, A. R. Ansari, M. Irfan, U. Ali, Canadian J. Phys. 68,67 (1990).

[9] Muller, A.H., Phys. Rev. D, 4 (1971) 150.

[10] Bhanja, R., Devi, N.A.L., Joseph, Z.R.R., Ojha, I.D., Shyan, M. and Tuli, S.K., Nucl. Phys. A, 411 (1983) 507.

[11] Jakobsson, B. and Kullberg, R., Phys. Scr., 13 (1976) 327.

[12] El-Sharkawy, S., Hegab, M.K., Osman, O.M. and Jilany, M.A., Physica Scripta, 47 (1993) 513.

[13] Joseph, R.R., Ojiha, I.D., Singh, B.K. and Tuli, S.K., J. Phys. G: Nucl. Part. Phys. 18.

[14] Dudkin, V.E. et al., Phys. A, 509 (1990) 783.

[15] El-Nadi, M., MSEL-Nagdy, Ali-Mossa, N., Abdelsalam, A., Abdalla, A.M. and Hamed, A.A., J. Phys. G: Nucl. Part. Phys., 25 (1999) 1169.

[16] Firu, E., Bradnova, V., Haiduc, M., Kovalenko, A.D., Akhov, A.I.M., Neagu, A.T., Rukoyatkin, P.A., Rusakov, A.V.V. Vokal, S. and Zarubin P. I., Res., Under Pn II-P4, No 81-044.

[17] Chernov, G.N., Gulamov, K.G., Gulyamov, U.G., Navotny, V.Sh., Petrov, N.V. and Svechnikova, L.N., Nuclear Physics A, 412 (1984) 534.

[18] Badawy, B.M., Journal of Nuclear and Radiation Physics, 3(1) (2008) 31.

[19] El- Nadi, M. et al., J. Phys. G, 19 (1993) 2027.

[20] Fakhraddin, S., Turk. J. Phys., 29 (2005) 79.

[21] Abdallah, N.N., et al., Can. J. Phys., 80 (2002) 119.

[22] Ali, S. S. and Khushnood, H., ISC, 1 (2012) 232.

[23] Khan, S. et al., M. J. Phys. Soc. Jpn., 65 (1996) 801.

[24] Adamovich, M.I. et al., Z. Phys. A, 351 (1995) 311 (EL-92-569).

[25] Adamovich, M.I. et al., Phys. Rev. C, 40 (1989) 66.

[26] Singh, G., Ismail, A.Z.M. and Jail, P.L., Phys. Rev. C, 43 (1991) 2417. Singh, G., Sengupta, K. and Jain, P.L. Phys. Rev. C, 42 (1991) 1757. Singh, G., Sengupta, K. and Jain, P.L., Phys. Len. B, 222 (1989) 301.

[27] EL-Nadi, M., Sherif, M.M., EL-Nagdy, M.S., Abdelsalam, A., Yasin, M.N., Jilany, M.A. and Baker, A. Int. J. Mod. Phys., 2 (1993) 381.

[28] EL-Nadi, M., Hussien, A., Shaat, E.A., Abu-Mousa, Z. and Hamed, A.A., Nuovo Cimento, 108A (1995) 935.

[29] El-Nadi, M., El-Nagdy, M.S., Ali-Mossa, N., Abdelsalam, A., Abdalla, A.M. and Abdel-Halim, S.M., J. Phys., 28 (2002) 1251.

الجدول (7): القيم المتوسطة لجسيمات $\alpha-$ المنتجة، والزخوم العيارية C_q، وزخم مولر الثاني F_2 لنوى مختلفة وطاقات مختلفة

Energy (GeV)	C^{12}	O^{16}			Ne^{22}	Mg^{24}	Si^{20}			S^{32}
	3.7	14.6	60	200	3.7	3.7	3.7	4.5	14.6	200
$< N_\alpha >$	1.5 ± 0.1^d	1.7 ± 0.1^b	1.7 ± 0.1^b 1.6 ± 0.1^c	1.7 ± 0.1^b 1.6 ± 0.2^c	1.6 ± 0.1^d	1.8 ± 0.1^e	1.8 ± 0.1^a 1.9 ± 0.1^d	$1.8 \pm 0.2^*$	1.7 ± 0.1^f 1.8 ± 0.1^a 1.9 ± 0.1^c	1.8 ± 0.1^a 1.7 ± 0.1^c
C_2	1.2 ± 0.1^d	1.2 ± 0.1^b	1.2 ± 0.1^b 1.2 ± 0.1^c	1.2 ± 0.1^b 1.2 ± 0.1^c	1.3 ± 0.1^d	1.3 ± 0.1^e	1.3 ± 0.1^a 1.3 ± 0.1^d	$1.3 \pm 0.2^*$	1.3 ± 0.1^f 1.3 ± 0.1^a 1.3 ± 0.1^c	1.3 ± 0.1^a 1.3 ± 0.1^c
C_3	1.7 ± 0.2^d	1.7 ± 0.1^b	1.7 ± 0.1^b 1.8 ± 0.1^c	1.7 ± 0.1^b 1.7 ± 0.1^c	2.1 ± 0.1^d	2.1 ± 0.1^e	2.1 ± 0.1^a 2.2 ± 0.1^d	$1.9 \pm 0.2^*$	2.3 ± 0.1^f 2.1 ± 0.1^a 2.3 ± 0.1^c	2.4 ± 0.1^f 2.3 ± 0.1^c
C_4	2.7 ± 0.2^d	2.6 ± 0.2^b	2.8 ± 0.1^b 2.9 ± 0.2^c	2.6 ± 0.1^b 2.8 ± 0.5^c	4.0 ± 0.1^d	3.9 ± 0.2^e	4.2 ± 0.1^a 4.4 ± 0.2^d	$3.8 \pm 0.2^*$	4.6 ± 0.2^f 4.7 ± 0.2^a 4.0 ± 0.2^c	5.0 ± 0.3^a 4.7 ± 0.2^c
C_5	4.7 ± 0.4^d	4.3 ± 0.1^b	4.7 ± 0.2^b 4.9 ± 0.3^c	4.3 ± 0.2^b 4.6 ± 0.4^c	8.5 ± 0.2^d	7.9 ± 0.5^e	9.3 ± 0.3^a 8.9 ± 0.3^d	$.85 \pm 0.6^*$	10.6 ± 0.5^f 10.6 ± 0.5^a 8.2 ± 0.4^c	11.9 ± 0.6^a 11.0 ± 0.4^c
F_2	1.0 ± 0.1^d	1.1 ± 0.1^b	1.1 ± 0.1^b 1.0 ± 0.1^c	1.1 ± 0.1^b 1.0 ± 0.1^c	0.9 ± 0.1^d	0.8 ± 0.1^e	0.8 ± 0.1^a 0.8 ± 0.1^d	$0.8 \pm 0.1^*$	0.8 ± 0.1^f 0.8 ± 0.1^a $0.8 + 0.1^c$	0.7 ± 0.1^a 0.7 ± 0.1^c

[24][a][25][b][26][c][27][d][28][e][29][f] [Present Work][*]

لتوضيح عدم اعتماد الزخوم العيارية على الطاقة، حسبت الزخوم العيارية لإنتاج شظايا الهيليوم (n_α) في تفاعل $Si^{28} - Em$ عند طاقة 4.5GeV/c،ومقارنتها مع نتائج تفاعلات نوى ($C.Ne.O.Mg.Si.S$) مع المستحلب عند طاقات مختلفة.

يوضح الجدول (7) الزخوم العيارية $C_2 \rightarrow C_5$ لنوى ($C.Ne.O.Mg.Si.S$)، ويتضمن زخم مولر (Muller) [9] الثاني الذي يعطى بالمعادلة:

$$F_2 = (C_2 - 1)(< n_\alpha >^2 - < n_\alpha >) \qquad (7)$$

يتضح من الجدول أن C_2،C_3 غير معتمدة تقريباً على الطاقة ورقم الكتلة، بينما تزداد قيم الزخوم الأعلى بزيادة رقم الكتلة.

كما نلاحظ أن قيمة زخم مولر الثاني لا يعتمد على الطاقة بينما يختلف باختلاف رقم الكتلة.

الاستنتاجات

استناداً على نتائج الدراسة الحالية نستنتج ما يلي:

1- عند تصادمات نوى السيلكون مع نوى المستحلب النووي، نجد أن نسبة كبيرة من التفاعلات تحدث مع النوى الثقيلة للمستحلب ($Ag.Br$) وباقي التفاعلات تحدث مع النوى الخفيفة ($C.N.O$) ونواة الهيدروجين(H).

2- يزداد متوسط المسار الحر (λ) لتفاعلات القذيفة مع كل مجموعات الهدف بزيادة طاقة القذيفة ويتناقص بزيادة كتلة القذيفة.

3- القيم التجريبية للمقطع العرضي النووي لقذائف مختلفة مع أهداف المستحلب النووي عند طاقة 4.5AGeV على اتفاق جيد مع القيم المحسوبة باستخدام علاقة Bradt - Peters كما أن المقطع العرضي النووي يزداد بزيادة كتلة القذيفة.

4- المقطع العرضي النووي لإنتاج جسيمات ألفا المنبعثة من مصادر مختلفة مستقل عن طاقة القذيفة في مدى طاقة AGeV(3.7-200) لقذائف تمتلك الكتلة نفسها.

5- تم تقدير كثافة الطاقة (ε) الناتجة من التصادمات المركزية لنوى السيلكون مع المستحلب النووي باستخدام نموذج بجوركن ($Bjorken$)، ووجد انها تساوي $\varepsilon \sim 2.4\varepsilon_0$، وهذه القيمة لا يمكن اعتبارها كثافة كافية لحدوث الانتقال من الطور الهادروني إلى حالة QGP .

6- قيم الزخوم العيارية (C_k)تبقى تقريباً ثابتة مع ثبات الحدود الإحصائية لقذائف مختلفة؛ أي أنها لاتعتمد على كتلة القذيفة، وإنما تعتمد على كتلة الهدف. كما أن قيمة هذا البارامتر تزداد بزيادة قيمة الثابت k.

7- بمقارنة النتائج التي تم الحصول عليها عند إيجاد الزخوم العيارية في تفاعلات نواة- نواة مع النتائج المتحصل عليها في تصادمات نواة – هادرون عالية الطاقة، نستنتج أن النتائج في تفاعلات نواة – نواة وتفاعلات نواة – هادرون متماثلة تقريباً، وأن آلية (Hadronization) للمرحلة النهائية للجسيمات المشحونة تكون نفسها.

شكر وتقدير

أقدم كل الشكر والعرفان الى كل من مد لي يد العون والمساندة في إنجاز هذا العمل. وأخص بالذكر الأستاذ الدكتور مصطفى عبد السلام بن نصر بعيو على نصائحه وإرشاداته وتوفير كل ما يلزم لإنجاز هذا العمل، علماً بأن هذه الورقة هي جزء من بحث متطلبات الإجازة العالية (الماجستير) في الفيزياء.

ومن الله العون والسداد، ونحن له من الذاكرين ولنعمائه من الشاكرين .

الجدول (5): كثافة الطاقه ε لتصادمات قذائف مختلفة مع أهداف مختلفة عند كميات حركة متقاربة

Interaction	Particles Multiplicity	Momentum AGeV/c	Energy Density(ε)	$dn/d\eta$	Ref.
$N_e^{22} - A_g$	$n_s = 35, n_h = 37$	4.1	$2.5\varepsilon_0$	14	[19]
$M_g^{24} - pb$	$n_s = 51, n_h = 77$	4.5	$2.25\varepsilon_0$	21	[20]
$S_i^{28} - Em$	$n_s - 53, n_h - 23$	4.5	$2.4\varepsilon_0$	21.67	Present Work

3. الزخوم العيارية

الزخوم العيارية (*Normalized Moments*) للتوزيعات التعددية للجسيمات المشحونة النسبية الناتجة في تصادمات نواة-هادرون عالية الطاقة درست من (Khushnood) وآخرين في مدى طاقة (50-400)AGeV[8]. في هذا العمل تمت دراسة الزخوم العيارية للتوزيعات التعددية للجسيمات المشحونة النسبية الناتجة في تفاعلات نواة-نواة، واعتمادها على كتلة القذيفة وطاقتها.

تعطى الزخوم العيارية للتوزيعات التعددية للجسيمات المشحونة النسبية بالمعادلة:

$$C_K = < n_s^k > / < n_s >^k \quad (6)$$

حيث k ثابت ويأخذ قيماً مختلفة: 2، 3، 4، 5، ...وهكذا.

لدراسة اعتماد C_K على حجم نواة الهدف، تم حساب قيم C_2, C_3, C_4 لمجموعات مختلفة لنوى المستحلب في تفاعلات $Si^{28} - N$ عند طاقة 4.5AGeV/c، وقيم C_K التي تم الحصول عليها في هذه التفاعلات موضحة في الجدول (6) مع نتائج تم الحصول عليها سابقاً في تفاعلات $C^{12} - N$ عند طاقة القذيفة نفسها.

الجدول (6): قيم الزخوم العيارية C_2, C_3, C_4 في تصادمات نواة-نواة عند كمية حركة شعاع 4.5GeV/c لكل نيوكليون

Type of Interaction	C_2	C_3	C_4	Ref.
$C^{12} - CNO$	1.41 ± 0.10	2.42 ± 0.23	4.73 ± 0.58	[21]
$Si^{28} - CNO$	1.41 ± 0.01	2.44 ± 0.007	4.41 ± 0.003	[22]
$S_i^{28} - CNO$	1.45 ± 0.02	2.62 ± 0.005	5.48 ± 0.001	Present Work
$C^{12} - Em$	1.43 ± 0.05	2.51 ± 0.12	5.15 ± 0.33	[21]
$C^{12} - Em$	$1.58 + 0.07$	$2.67 + 0.13$	-	[23]
$Si^{28} - Em$	1.53 ± 0.01	3.06 ± 0.013	7.19 ± 0.01	[22]
$S_i^{28} - Em$	1.6 ± 0.04	3.32 ± 0.02	7.9 ± 0.03	Present Work
$C^{12} - A_gB_r$	$1.27 \perp 0.06$	$2.20 \perp 0.13$	$3.09 \perp 0.24$	[21]
$C^{12} - A_gB_r$	1.29 ± 0.26	2.48 ± 0.08	-	[23]
$Si^{28} - AgBr$	1.31 ± 0.007	4.56 ± 0.004	3.55 ± 0.35	[22]
$S_i^{28}\ A_gB_r$	1.25 ± 0.002	1.82 ± 0.001	2.9 ± 0.5	Present Work
$Si^{28} - H$	1.45 ± 0.03	3.11 ± 0.02	10.04 ± 0.01	Present Work

من الملاحظ أن قيم C_K في تصادمات $Si^{28} - N$ وتفاعلات $C^{12} - N$ عند طاقة 4.5GeV/c، ثابتة تقريباً مع ثبات الحدود الإحصائية، وهذا واضح بشكل كبير في الجدول (6)، حيث نلاحظ أن البارامترات C_K تزداد بزيادة قيمة k. بمقارنة نتائج العمل الحالي مع النتائج التي تم الحصول عليها في تصادمات نواة – هادرون عند طاقات $(50AGeV, 400AGeV)$، نلاحظ أن قيمة C_K متماثلة جداً في أنواع التفاعلات كلها.

حيث A تمثل رقم الكتلة لنواة السيلكون ويساوي 28.

في حالة التصادمات المركزية لـ $Si^{28}-Em$ عند كمية حركة شعاع $4.5AGeV/c$ وعند حدث مفرد $n_s=53$،$n_h=23$ تم الحصول على أعلى تعددية لهذا التفاعل: $\left(\frac{dn_s}{d\eta}\right)_{max}=20.67$ كما هو موضح في الشكل (3)، حيث η تمثل الاسراع الزائف العياري (Normalized Pseudorapidity):

$$\eta=(\eta-\eta_{min})/(\eta_{max}-\eta_{min})$$

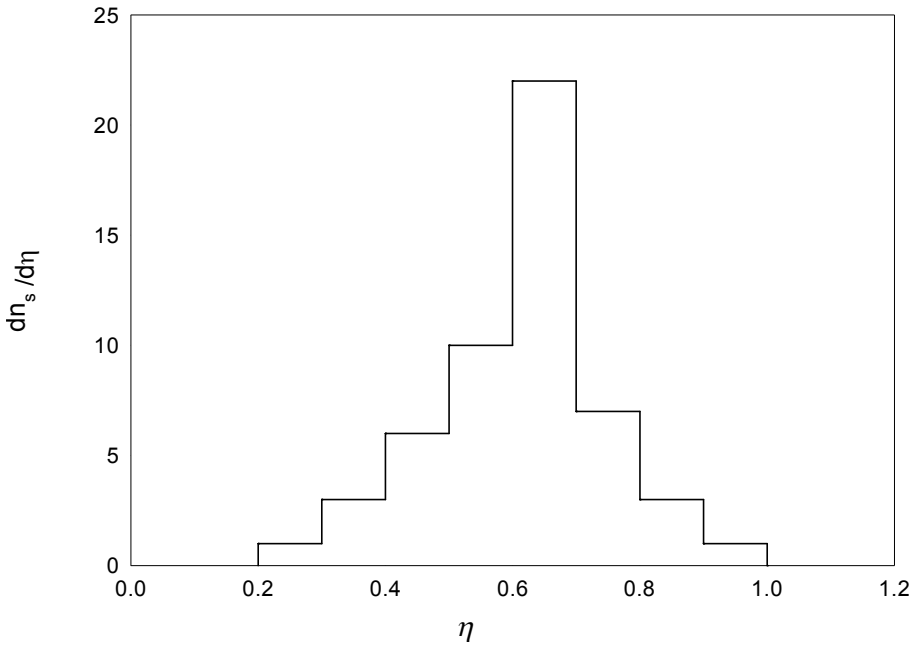

الشكل (3): توزيعات الإسراع الزائف العياري للجسيمات الرذاذية الناتجة في حدث مفرد عند $\eta_s=53$ و$\eta_h=23$ لتفاعلات السيلكون مع المستحلب النووي عند كمية حركة شعاع 4.5AGeV/c

حيث متوسط الزخم المستعرض $\langle P_T \rangle$ يساوي $(0.350\frac{GeV}{c})$ وm_π (كتلة البايون) تساوي $\frac{0.140GeV}{c^2}$.

وبالتعويض في المعادلة (4) نحصل على:

$$\varepsilon=0.31\frac{GeV}{fm^3}=2.4\varepsilon_0,\ \varepsilon_0=0.13\ GeV/fm^3$$

وهي كثافة الطاقة الناتجة من تحليل البيانات التي تم الحصول عليها من معجل دوبنا بروسيا، وهي غير كافية لحدوث الانتقال في الطور إلى حالة QGP، حيث تصل كثافة الطاقة عند QGP إلى كثافة عالية قدرت بحوالي $\varepsilon\sim(15-25)\varepsilon_0\sim(2-3)GeV/fm^3$

وللمقارنة، وجد أنه في معجل AGS (Alternating Gradient Synchrotron) الموجود في دوبنا وبروكهيفن (Dubna and Brookhaven)، أجريت تجربة لتصادم مركزي لـ $Au-Au$، وتم تقدير كثافة الطاقة طبقاً لنموذج $Bjorken$. وقد وجد أن كثافة الطاقة $\varepsilon=1.3GeV/fm^3$، وهي أيضاً كثافة طاقة غير كافية لإحداث انتقال في الطور.

كما قدرت كثافة الطاقة أيضاً للتصادم المركزي لـ $pb-pb$ في معجل SPS (Super Proton Synchrotron) الموجود في سيرن (CERN)، وكانت كثافة الطاقة $\varepsilon=3GeV/fm^3$ اعتماداً على خاصية الإسراع الزائف للجسيمات الناتجة [4]، وهذه الكثافة من الطاقة من الممكن أن يحدث فيها انتقال في الطور. الجدير بالملاحظة أنه لحدوث انتقال في الطور لابد من إحداث تصادم جسيمات ثقيلة بطاقة عالية جداً.

يوضح الجدول (5) مقارنة القيمة التي تم الحصول عليها ببعض النتائج التي حصل عليها باحثون آخرون لتصادمات قذائف وأهداف مختلفة.

أن المقطع العرضي للتفاعل النووي يزداد بزيادة كتلة القذيفة.

الجدول (4): القيم التجريبيه للمقطع العرضي للتفاعل النووي غير المرن ومقارنتها بالقيم التي تم الحصول عليها بواسطة صيغة Bradt - Peters لقذائف مختلفة مع أهداف المستحلب النووي، عند كمية حركة 4.5AGeV/c

Projectile	σ_H mb	σ_{CNO} mb	σ_{Em} mb	σ_{AgBr} mb	Ref.
p	37.70 (32.3)	291.36 (249.79)	415.52 (357.03)	1161.37 (998.67)	
He^3	89.72 (84.10)	527.05 (489.77)	635.70 (591.76)	1618.57 (1506.62)	
He^4	100.67 (103.42)	533.89 (546.64)	629.64 (644.54)	1568.97 (1605.15)	[18]
Li^6	162.53 (138.42)	755.74 (641.52)	861.26 (732.51)	2074.12 (1765.00)	
Si^{28}	284.900 (182.753)	371.474 (445.710)	804.6 (1521.394)	2575.327 (2227.045)	Present Work

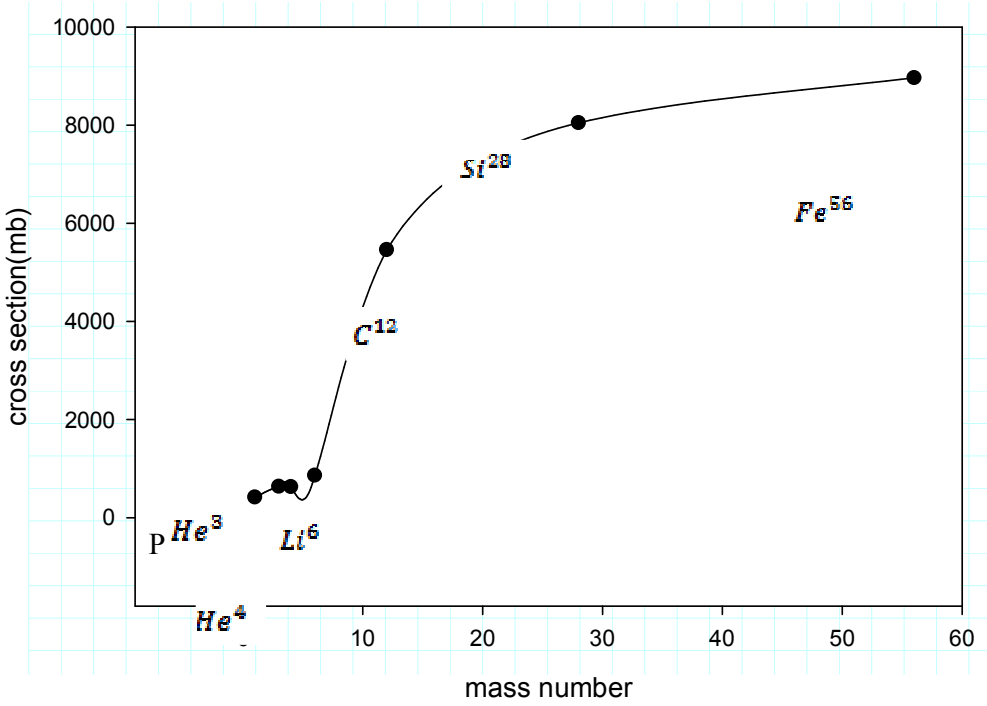

الشكل (2) يوضح علاقة المقطع العرضي للتفاعل النووي بكتلة القذيفة وذلك في حالة تصادمات قذائف مختلفة بالمستحلب النووي عند كمية حركة شعاع 4.5AGeV/c

2. تقدير كثافة الطاقة:

إن معرفة كثافة الطاقة (*energy density*) التي نتجت في التصادمات الشديدة تمكننا من البحث عن الطور الجديد (الانتقال من الطور الهادروني إلى طور كوارك-قليون بلازما)، ولتقدير كثافة الطاقة ε نستخدم صيغة بجوركن(Bjorken) :

$$\varepsilon = \frac{3}{2}\sqrt{< P_T >^2 + m_\pi^2}\left(\frac{dn_S}{d\eta}\right)V^{-1} \qquad (4)$$

حيث V = المساحة العرضية لتداخل النواتين عند التصادم.

$$V = \pi A^{2/3}(1.18)^2 \qquad (5)$$

الجدول (3): متوسط المسار الحر (λ) لقذائف مختلفة عند كميات حركه مختلفة

Element	Energy(AGeV/c)	Mean Free Path λ(cm)	Ref.
S_i^{28}	4.5	1.56	Present work
S_i^{28}	14.6	12.65	[15]
F_e^{56}	1	7.53	[16]
F_e^{56}	1.7	8.4	[17]

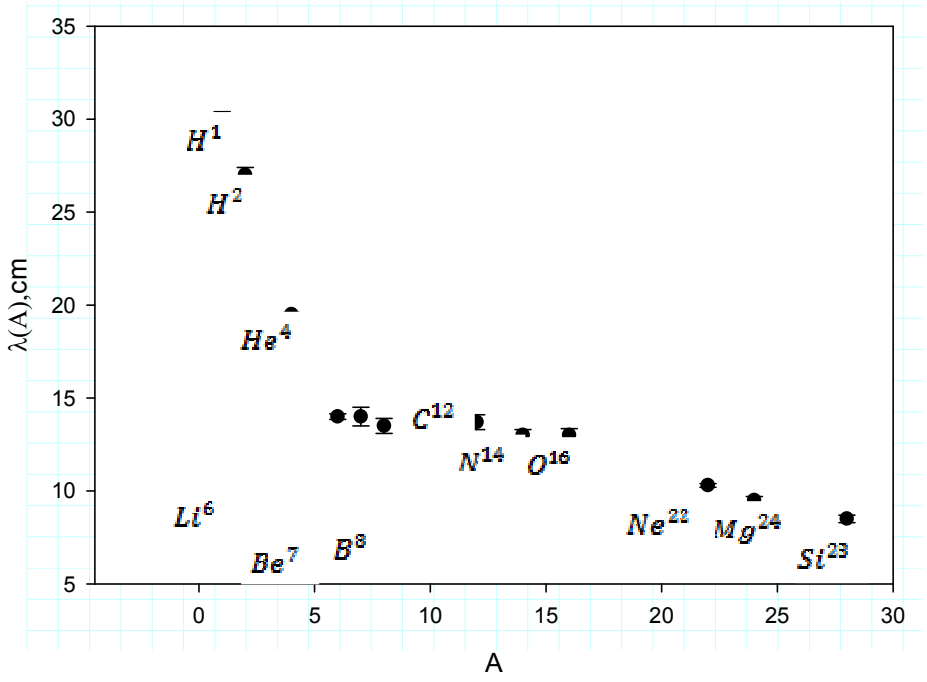

الشكل (1): العلاقة بين المسار الحر $\lambda(A)$ ورقم الكتلة للقذيفة

كذلك يمكن حساب المقطع العرضي للتفاعل باستخدام علاقة Bradt – Peters [7]، وهي تعبير هندسي مفيد لحساب المقطع العرضي لتفاعل الأيون الثقيل في حدود منطقة الطاقة، وتعطى بالمعادلة.

$$\sigma = \pi \left[r^{\circ} \left(A_p^{\frac{1}{2}} + A_t^{\frac{1}{2}} - b \right) \right]^2 \qquad (2)$$

حيث A_t كتلة الهدف، A_p كتلة القديفة، b بارامتر التصادم الذي يمكن حسابه من العلاقة:

$$b = \left[1.3 \left(A_p^{\frac{1}{3}} + A_t^{\frac{1}{3}} \right) + 0.4 \right] fm \qquad (3)$$

حيث $r_{\circ} = 1.25$ fm. وبتطبيق المعادلتين (2) و(3) نجد أن:

$$\begin{bmatrix} \sigma_H = 182.75 \text{ mb}, \sigma_{CNO} = 445.7 \text{ mb}, \\ \sigma_{Ag\ Br} = 2227.05\ mb, \sigma_{Em} = 1521.39\ mb \end{bmatrix}$$

القيم باستخدام المعادلة (2)

نلاحظ أن القيم المحسوبة للمقاطع العرضية باستخدام علاقة Bradt - Peters على اتفاق جيد مع القيم التجريبية، ويوضح الجدول (4) القيم التجريبية للمقطع العرضي لتفاعل قذائف مختلفة مع أهداف المستحلب النووي عند كمية حركة شعاع 4.5AGeV/c ومقارنتها بالقيم المحسوبة باستخدام علاقة Bradt - Peters.

كما نبين في الشكل (2) علاقة المقطع العرضي للتفاعل بكتلة القذيفة في حالة تصادم قذائف مختلفة بالمستحلب النووي عند كمية حركة شعاع 4.5AGeV/c، حيث نلاحظ

وسرعة نسبية $0.3 < \beta < 0.7$، وطاقتها تتراوح بين (26-375MeV). أغلب هذه الجسيمات عبارة عن بروتونات الهدف المرتدة وبعض من الديوترونات Deuterons والترايتونات Tritons. وجدير بالذكر أن شظايا القذيفة المشحونة الثنائية مع زاوية انبعاث ($\theta \leq 3^{\circ}$) تنتج التأين نفسه للمسارات الرمادية، ولكن لم تدرج ضمن حسابات المسارات الرمادية.

- الجسيمات السوداء Black Particles (n_b)، وتمتلك تأيناً نوعياً ($I^* > 10$) ومدى $R < 3mm$ وسرعة نسبية $\beta \leq 0.3$،وطاقتها $E < 30MeV$. هذه الآثار السوداء تنتج عن الشظايا،جسيمات ألفا، وديوترونات، وبروتونات وهي تبدو كجسيمات ثانوية بطيئة ذات تأين عالٍ.

من ثم فإن الجسيمات المنبعثة تكون: شظايا قذيفة (التي قسُمت ثانية إلى مفردة الشحنة، وثنائية الشحنة ومتعددة الشحنة)، والجسيمات الرذاذية n_s، وشظايا الهدف (الجسيمات الرمادية n_g، والجسيمات السوداء n_b). وتحمل أثار هذه الجسيمات وصفاً متكاملاً لسلوك المادة النووية.

النتائج والمناقشة

1. المقطع العرضي للتفاعل

تعدُ دراسة المقطع العرضي للتفاعل من المفاهيم الهامة عند دراسة تصادم الجسيمات عالية الطاقة، حيث يعبر عن احتمالية حدوث الحدث (Event) عند قذف جسيم مفرد عمودياً على هدف يتكون من جسيم واحد لوحدة المساحة. فكرة المقطع العرضي أنه يعطي مساحة تخيلية لكل جسيم، ويتم اختيار المساحة بحيث إذا مر خلالها جسيم ساقط يحدث التفاعل، وإذا مر خارجها لا يحدث التفاعل. ويمكن تصور جسيم الهدف بأنه يشكل مساحة معينة بالنسبة للجسيم الساقط. وعند توجه الجسيم الساقط إلى الهدف فإنه يتفاعل معه ضمن هذه المساحة، وكلما زادت مساحة الهدف زادت احتمالية التفاعل بين الجسيم الساقط والهدف. وتسمى هذه المساحة مساحة مقطع التفاعل، وتتباين مساحة مقطع التفاعل للهدف تبعاً لطبيعة التفاعل وطاقة الجسيم الساقط.

المقطع العرضي (Cross-Section) التجريبي لتفاعلات كل مجموعات الهدف σ_H ،σ_{CNO}،σ_{AgBr} من العلاقة:

$$\sigma = \frac{1}{\lambda \rho} \qquad (1)$$

يقاس المقطع العرضي للتفاعل بوحدة البارن أو الميكرومتر المربع ($1b = 10^{-28}m^2$).

λ متوسط المسار الحر (Mean Free Path)، وهو متوسط المسافة المقطوعة بين التصادمات المتتالية التي يحدثها الجسيم مع النوى.

مسار الجسيم نتيجة التصادم هو خط منكسر كما في الشكل التالي، والنقط على هذا الخط تمثل أماكن التصادمات.

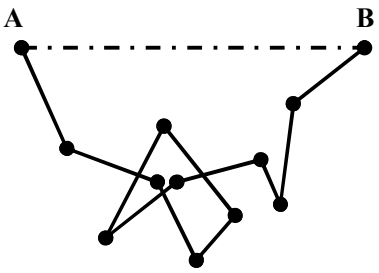

مسار جسيم يتعرض للتصادم

المسافة الفعلية التي يقطعها الجسيم بين النقطتين AوB أكبر من طول الخط الواصل بينهما.

$$\lambda = \frac{\text{طول المسار الكلي الذي يقطعه الجسيم}}{\text{العدد الكلي للتصادمات الحادثة}}$$

يبين الجدول (3) علاقة متوسط المسار الحر بطاقة القذيفة، حيث نلاحظ أن متوسط المسار الحر يزداد بزيادة طاقة القذيفة، كما نلاحظ من الشكل (1) أن متوسط المسار الحر يتناقص بزيادة كتلة القذيفة.

ρ الكثافه (Density) ($gm.cm^{-3}$) لمجموعة النوى المعطاة في الجدول (1) [6]. باستخدام التركيب الكيميائي للمستحلب النووي وباستخدام المعادلة (1)، حيث $\lambda - 1.56cm$ في حالة تصادمات السيلكون مع المستحلب النووي، وجدنا أن:

$$\begin{bmatrix} \sigma_{\mathrm{H}} = 284.9\ \mathrm{mb}.\ \sigma_{\mathrm{CNO}} = 371.47\ \mathrm{mb}. \\ \sigma_{Ag\ Br} = 2575.33\ mb.\ \sigma_{Em} = 804.6\ mb \end{bmatrix}$$

القيم التجريبية

يمكن تقسيم التفاعلات النووية مع نوى المستحلب النووي كما يلي:

- التفاعلات النووية مع النوى الثقيلة $AgBr$ تكون عند: $n_h > 8$.
- التفاعلات النووية مع النوى الخفيفة CNO تكون عند: $2 \leq n_h \leq 8$.
- التفاعلات النووية مع نوى الهيدروجين H تكون عند: $n_h \leq 1$.

على أساس هذه التقسيمات تحصل على:

115 تفاعلاً مع نوى H، 210 تفاعلات مع النوى الخفيفة CNO، و223 تفاعلاً مع النوى الثقيلة $AgBr$ في عينة فيها 548 تفاعلا في حالة تصادمات $Si-Emulsion$ عند كمية حركة شعاع قدرها 4.5AGeV/c، وكل تفاعل من هذه التفاعلات ينتج عنه انبعاث شظايا.

يوضح الجدول (2) نسبة تصادم المقذوف مع مختلف مجموعات النوى في المستحلب النووي. ونلاحظ أن التفاعلات مع H تتزايد بزيادة كتلة الشعاع ، بينما التفاعلات مع $AgBr$ تتناقص بزيادة كتلة الشعاع.

الجدول (2): نسبة تصادم المقذوف مع مجموعات النوى المختلفة في المستحلب النووي

Projectile	Energy (AGeV/c)	H ($< A >= 1$)	CNO ($< A >= 14$)	Ag Br ($< A >= 94$)	Ref.
N^{14}	2.1	12.7	32.9	54	[10]
O^{16}	2	10.8	37.9	51.3	[11]
M_g^{24}	4.5	11.06	34.45	54.49	[12]
S_i^{28}	4.5	20.99	38.74	40.69	Present Work
A_r^{40}	1.8	17.8	34.6	47.5	[13]
F_e^{56}	1.8	16.6	35.6	47.8	[14]

في تجارب المستحلب النووي، وعند حدوث تصادم وإنتاج الشظايا النووية، فإن انبعاث الجسيمات في تصادمات نواة – نواة عالية تمتلك خصائص مختلفة. فصنفت آثار هذه الجسيمات الناتجة على أساس السرعة النسبية $\left(\beta = \frac{v}{c}\right)\beta$ والمدى R المتبقي لها في المستحلب وكثافة حبيبة الأثر المتكون في المستحلب (التأين النوعي) I^*. وهذا التقسيم هو المتبع في المرجع [5]:

1. شظايا القذيفة Projectile Fragments (PFs)، وهي شظايا نواة القذيفة غير المتفاعلة Spectator Projectiles الناشئة من استمرار الجسيم هابطاً في مساره بعد الاصطدام بالنوى الساقطة. هذه الجسيمات تمتلك تقريباً سرعة النوى الساقطة نفسها بمعنى أن سرعتها النسبية $(\beta < 1)$، وهي ذات تأين ثابت وتتميز بمدى طويل وزوايا انبعاث صغيرة.
2. الجسيمات الرذاذية Shower particles (n_s)، تنتج هذه الجسيمات بشكل سريع ومباشرة بعد حدوث التصادم مما يجعل النوى المتبقية في حالة إثارة. هذه الجسيمات مشحونة مفردة نسبية، وتتميز آثار هذه الجسيمات بمداها الطويل نسبياً، وأغلب هذه الجسيمات هي بايونات، وفوتونات سريعة، وبروتونات بالإضافة إلى مساهمة صغيرة من شظايا القذيفة المشحونة المفردة. تمتلك الجسيمات الرذاذية تأيناً نوعياً (Specific Ionization) $I^* \leq 1.4$ حيث $(I^* = I/I_0)$، I يمثل التأين لأثر الجسيم الثانوي، I_0 يمثل الحد الأدنى التجريبي للتأين بزاوية انبعاث $(\theta \leq 3^\circ)$ وسرعة نسبية $\beta \geq 0.7$. مثل هذه الجسيمات تخضع لاستطارة متعددة شديدة. وبناءً على ذلك تنفصل البايونات الناتجة عن شظايا القذيفة المشحونة المفردة.
3. شظايا الهدف Target Fragments (TFs) وهي عبارة عن شلال من الجسيمات أو النيوكليونات المرتدة التي تنبعث من تبخر النواة المتبقية، هذا الصنف قسم إلى:
   - الجسيمات الرمادية Gray Particle (n_g)، وتمتلك تأيناً نوعياً $(1.4 < I^* < 10)$ ومدى $R \geq 3mm$

النووية العادية)، فإن المادة المتفاعلة بشكل قوي تمر بمرحلة تحول لحالة جديدة من المادة تعرف باسم كوارك - قليون بلازما Quark-Gluon Plasma (QGP). تتغير درجة الحرية (Degree of Freedom) خلال مرحلة التحول من الهاردونات متعادلة اللون إلى البارتونات (Partons) ذات الشحنة اللونية [2].

لدراسة هذه المرحلة تجريبياً، لابد من تصادم بين النوى بعد تعجيلها بطاقة عالية؛ إذ إن نوى الاصطدام تخترق بعضها بعضاً، وتبدأ النيوكليونات بتبادل الطاقة والزخم، وبذلك تفقد نوى الاصطدام هويتها بالكامل وتندمج مع بعضها مكونة كرة نارية (Fire Ball) [3] أولية ساخنة تتوسع وتبرد وتؤول في النهاية إلى نيوكليونات وبايونات ...إلخ.

لذلك، فالعديد من النماذج النظرية تُقترح من وقت لآخر لوصف تصادم نواة – نواة وتفسير البيانات التجريبية المتعلقة بمختلف نواتج التصادم. هذه النماذج المختلفة تصف مظاهر مختلفة من التصادم، وذلك لأنه لا يوجد نموذج يمكن أن يصف كل مظاهر التصادمات عند الطاقات العالية. ومن هذه النماذج نموذج بجوركن (Bjorken) [4] الذي يوضح كيفية تقدير كثافة الطاقة وإمكانية التحول من الطور الهادروني إلى طور كوارك – قليون بلازما (QGP).

مصدر البيانات التجريبية

البيانات المستخدمة هي لمعجل *Dubna Synchrophasotron* في روسيا، وذلك باستخدام تقنية المستحلب النووي (Nuclear Emulsion)، حيث تم تعريض كومة (*Stack*) من المستحلب النووي من نوع $\mathbf{NIKFI-BR_2}$ ذات أبعاد $(16.9 \times 9.6 \times 0.06)cm^3$، لشعاع من أيونات السيلكون ذات كمية حركة شعاع قدرها *4.5AGeV/c*، وباستخدام Nikon Microscope متحرك بقوة تكبير 40x Objectives و15x Eye-pieces التُقطت الآثار الابتدائية على مسافة 3mm من حافة الدخول إلى الكومة وجرى تتبعها للخلف للتأكد من أنها لم تأت من تفاعل سابق.

وبهذه الطريقة، جرى تتبع جميع الآثار الابتدائية من دخولها إلى الكومة حتى تفاعلت مع الكومة أو غادرتها، كما تم تعيين مختلف متغيرات (بارامترات) التفاعل لكل نجم Star (n_s،n_g،n_b) زاوية الإنبعاث لكل جسيم) تحت عدسات ذات قوة تكبير 15xEye-pieces و 95xOil Immersion Objectives.

هذه البيانات وزعت على عدة مراكز للطاقة العالية لتحليلها، ومن هذه المراكز (Aligarh) بالهند، ومن هذا المركز تم الحصول على هذه البيانات من الدكتور المشرف (Prof.Mustafa Bayio). وقمت بتحليل هذه البيانات التي تم الحصول عليها في قسم الفيزياء في جامعة مصراتة بليبيا، حيث شملت البيانات في هذه الدراسة على 548 تفاعلاً قابلاً للتحليل من السيلكون مع المستحلب النووي. ويوضح الجدول (1) الكثافة التي تقابل كل عنصر من مكونات المستحلب بوحدة $atoms/cm^3$.

يتكون المستحلب النووي من مادة عجينية تتألف من بلورات دقيقة من هاليد الفضة يكون معظمها من البروم مع مخلوط صغير من اليود، هذه البلورات تكون مغمورة في الجيلاتين (Gelatin)، وهو عبارة عن مادة عضوية معقدة قادرة على امتصاص كميات كبيرة من الماء. إن الوظيفة الأساسية للجيلاتين هي التزويد بشبكة ثلاثية الأبعاد تعمل أساساً على تحديد مكان البلورات الصغيرة ومنعها من الهروب أثناء الإظهار والتثبيت (Development and Fixation). لذلك فالجيلاتين يعتبر مادة ملينة تخفف من هشاشة المستحلب.

كذلك يحتوي المستحلب النووي على ماء بحيث يبقيه رطباً ويمنعه من التقشير.

الجدول (1): التركيب الكيميائي للمستحلب النووي من نوع "NIKFI – BR2"

Element	H^1	C^{12}	N^{14}	O^{16}	B_r^{80}	A_g^{108}
$atoms/cm^3 \times 10^{22}$	3.15	1.41	0.395	0.956	1.028	1.028

المجلد 7، العدد 2، 2014. ص ص. 99- 109

المجلة الأردنية للفيزياء

ARTICLE

بعض الصفات العامة للشظايا المنبعثة في تفاعلات السيلكون مع المستحلب النووي عند طاقة شعاع 4.5GeV لكل نيوكليون

فاطمة عبد السلام أبوزقية ومصطفى عبدالسلام بن نصر بعيو
قسم الفيزياء، كلية العلوم، جامعة مصراتة، مصراتة، ليبيا.

Received on: 4/7/2013; *Accepted on: 30/3/2014*

الملخص: هذه المحاولة أجريت لدراسة بعض مميزات إنتاج الشظايا النووية في التصادمات النووية عالية الطاقة، وذلك من خلال دراسة خصائص الانبعاث مثل المقطع العرضي للتفاعل النووي، والزخوم العيارية للجسيمات النسبية، ودراسة اعتماد هذه الخصائص على كتلة القذيفة والهدف وطاقة القذيفة، في تفاعلات $Si^{28} - Em$ عند كمية حركة شعاع قدرها $4.5GeV/c$ لكل نيوكليون.
النتائج التي تم الحصول عليها في هذه الدراسة تمت مناقشتها ومقارنتها بنتائج باحثين آخرين،حيث لوحظ الاتفاق الجيد مع هذه النتائج. كما تم أيضاً في هذا العمل حساب كثافة الطاقة الناتجة من التصادمات المركزية لنوى السيلكون مع نوى المستحلب النووي، وذلك باستخدام نموذج $Bjorken$.

Some General Properties of the Emitted Fragments in Interactions at 4.5GeV per Nucleon

Fatima Abu Zaghia and Mustafa Bayio
Physics Department, Faculty of Science, Misrata University, Misrata, Libya.

Abstract: An attempt has been made to investigate some features of nuclear fragments produced in high energy heavy ion collisions. Emission characteristics such, as the nuclear cross- section and the normalized moments of relativistic charged particles and their dependence on the projectile and target mass and the projectile energy, produced in (4.5AGeV/c)silicon – emulsion interactions, are investigated. Results obtained in the present work are compared with those reported by other researchers.
The energy density has been calculated using the Bjorken model.

Keywords: Nuclear emulsion; Quark-gluon plasma; Cross-section; Normalized moments; Energy density.
PACS: 25.75.-q

المقدمة

تعتبر تصادمات نواة- نواة من العمليات النووية التي تؤدي إلى تقدير جيد لحالة المادة عند الكثافات العالية ودرجات الحرارة المرتفعة، وذلك بسبب حدوث تصادمات نووية متعددة وإنتاج شظايا متعددة.

لذا فالتشظي النووي عملية مهمة لدراسة التفاعلات النووية ذات الطاقة العالية؛ فهي تزودنا بمعلومات دقيقة عن ميكانيكية التفاعل وكذلك عن تركيب النواة [1].

تعرف النظرية الكمية التي تصف هذه التفاعلات النووية من حيث مميزات وسلوك غالبية المكونات الأساسية للمادة وسلوكها، بديناميكا الكم اللونية (Quantum Chromo-Dynamics) (QCD).، تفترض هذه النظرية انه عندما تزيد درجة حرارة الجسم النووي أكثر من مستوى معين، قدر بحوالي $T_c = 200MeV$، وكثافة طاقة مقدارها $\varepsilon \approx (15-25)\varepsilon_0$، حيث ε_0 (كثافة الطاقة للمادة

Corresponding Author: Fatima Abu Zaghia **Email**: fatbuz77@gmail.com

Authors Index

Subject Index

طرائق البحث (التجريبية / النظرية): يجب أن تكون هذه الطرائق موضحة بتفصيل كاف لإتاحة إعادة إجرائها بكفاءة، ولكن باختصار مناسب، حتى لا تكون تكرارا للطرائق المنشورة سابقا.

النتائج: يستحسن عرض النتائج على صورة جداول وأشكال حيثما أمكن، مع شرح قليل في النص ومن دون مناقشة تفصيلية.

المناقشة: يجب أن تكون موجزة وتركز على تفسير النتائج.

الاستنتاج: يجب أن يكون وصفا موجزا لأهم ما توصلت إليه الدراسة ولا يزيد عن صفحة مطبوعة واحدة.

الشكر والعرفان: الشكر والإشارة إلى مصدر المنح والدعم المالي يكتبان في فقرة واحدة تسبق المراجع مباشرة.

المراجع: يجب طباعة المراجع بأسطر مزدوجة ومرقمة حسب تسلسلها في النص. وتكتب المراجع في النص بين قوسين مربعين. ويتم اعتماد اختصارات الدوريات حسب نظام Wordlist of Scientific Reviewers.

الجداول: تعطى الجداول أرقاما متسلسلة يشار إليها في النص. ويجب طباعة كل جدول على صفحة منفصلة مع عنوان فوق الجدول. أما الحواشي التفسيرية، التي يشار إليها بحرف فوقي، فتكتب أسفل الجدول.

الرسوم التوضيحية: يتم ترقيم الأشكال والرسومات والرسومات البيانية (المخططات) والصور، بصورة متسلسلة كما وردت في النص.

تقبل الرسوم التوضيحية المستخرجة من الحاسوب والصور الرقمية ذات النوعية الجيدة بالأبيض والأسود، على ان تكون أصيلة وليست نسخة عنها، وكل منها على ورقة منفصلة ومعرفة برقمها بالمقابل. ويجب تزويد المجلة بالرسومات بحجمها الأصلي بحيث لا تحتاج إلى معالجة لاحقة، وألا تقل الحروف عن الحجم 8 من نوع Times New Roman، وألا تقل سماكة الخطوط عن 0.5 وبكثافة متجانسة. ويجب إزالة جميع الألوان من الرسومات ما عدا تلك التي ستنشر ملونة. وفي حالة إرسال الرسومات بصورة رقمية، يجب أن تتوافق مع متطلبات الحد الأدنى من التمايز (1200 dpi Resolution) لرسومات الأبيض والأسود الخطية، و 600 dpi للرسومات باللون الرمادي، و300 dpi للرسومات الملونة. ويجب تخزين جميع ملفات الرسومات على شكل (jpg)، وأن ترسل الرسوم التوضيحية بالحجم الفعلي الذي سيظهر في المجلة. وسواء أرسل المخطوط بالبريد أو عن طريق الشبكة (Online)، يجب أرسال نسخة ورقية أصلية ذات نوعية جيدة للرسومات التوضيحية.

مواد إضافية: تشجع المجلة الباحثين على إرفاق جميع المواد الإضافية التي يمكن أن تسهل عملية التحكيم. وتشمل المواد الإضافية أي اشتقاقات رياضية مفصلة لا تظهر في المخطوط.

المخطوط المنقح (المعدّل) والأقراص المدمجة: بعد قبول البحث للنشر وإجراء جميع التعديلات المطلوبة، فعلى الباحثين تقديم نسخة أصلية ونسخة أخرى مطابقة للأصلية مطبوعة بأسطر مزدوجة، وكذلك تقديم نسخة إلكترونية تحتوي على المخطوط كاملا مكتوبا على Microsoft Word for Windows 2000 أو ما هو استجد منه. ويجب إرفاق الأشكال الأصلية مع المخطوط النهائي المعدل حتى لو تم تقديم الأشكال إلكترونيا. وتخزن جميع ملفات الرسومات على شكل (jpg)، وتقدم جميع الرسومات التوضيحية بالحجم الحقيقي الذي ستظهر به في المجلة. ويجب إرفاق قائمة ببرامج الحاسوب التي استعملت في كتابة النص، وأسماء الملفات على قرص مدمج، حيث يعلَم القرص بالاسم الأخير للباحث، وبالرقم المرجعي للمخطوط للمراسلة، وعنوان المقالة، والتاريخ. ويحفظ في مغلف واقٍ.

الفهرسة: تقوم المجلة الأردنية للفيزياء بالإجراءات اللازمة لفهرستها وتلخيصها في جميع الخدمات الدولية المعنية.

حقوق الطبع

يُشَكِّل تقديم مخطوط البحث للمجلة اعترافاً صريحاً من الباحثين بأنّ مخطوط البحث لم يُنْشَر ولم يُقَدَّم للنشر لدى أي جهَة أخرى كانت وبأي صيغة ورقية أو إلكترونية أو غيرها. ويُشترط على الباحثين ملء أنموذجٍ يَنُصُّ على نقْل حقوق الطبع لتُصبح ملكاً لجامعة اليرموك قبل الموافقة على نشر المخطوط. ويقوم رئيس التحرير بتزويد الباحثين بإنموذج نقل حقوق الطبع مع النسخة المُرْسَلَة للتنقيح. كما ويُمنع إعادة إنتاج أيِّ جزء من الأعمال المنشورة في المجلّة من دون إذن خَطِّيٍّ مُسْبَق من رئيس التحرير.

إخلاء المسؤولية

إن ما ورد في هذه المجلة يعبر عن آراء المؤلفين، ولا يعكس بالضرورة آراء هيئة التحرير أو الجامعة أو سياسة اللجنة العليا للبحث العلمي أو وزارة التعليم العالي والبحث العلمي. ولا يتحمل ناشر المجلة أي تبعات مادية أو معنوية أو مسؤوليات عن استعمال المعلومات المنشورة في المجلة أو سوء استعمالها.

معلومات عامة

المجلة الأردنية للفيزياء هي مجلة بحوث علميّة عالمية متخصصة مُحكمة تصدر بدعم من صندوق دعم البحث العلمي، وزارة التعليم العالي والبحث العلمي، عمان، الأردن. وتقوم بنشر المجلة عمادة البحث العلمي والدراسات العليا في جامعة اليرموك، إربد، الأردن. وتنشر البحوث العلمية الأصيلة، إضافة إلى المراسلات القصيرة Short Communications، والملاحظات الفنية Technical Notes، والمقالات الخاصّة Feature Articles، ومقالات المراجعة Review Articles، في مجالات الفيزياء النظرية والتجريبية، باللغتين العربية والإنجليزية.

تقديم مخطوط البحث

تُرسَل نسخة أصلية وثلاث نسخ من المخطوط، مُرْفَقَةً برسالة تغطية من جانب الباحث المسؤول عن المراسلات، إلى رئيس التحرير:

أ.د. نهاد عبدالرؤف يوسف،
رئيس التحرير، المجلة الأردنية للفيزياء،
عمادة البحث العلمي والدراسات العليا،
جامعة اليرموك، إربد، الأردن.
هاتف : 111 11 72 2 962 00 / فرعي: 2075
فاكس : 121 11 72 2 962 00
بريد إلكتروني : jjp@yu.edu.jo

تقديم المخطوطات إلكترونيًا: اتبع التعليمات في موقع المجلة على الشبكة العنكبوتية.

ويجري تحكيمُ البحوثِ الأصيلة والمراسلات القصيرة والملاحظات الفنية من جانب مُحكّمين اثنين في الأقل من ذوي الاختصاص والخبرة. وتُشَجِّع المجلة الباحثين على اقتراح أسماء المحكمين. أما نشر المقالات الخاصّة في المجالات الفيزيائية النَشِطَة، فيتم بدعوة من هيئة التحرير، ويُشار إليها كذلك عند النشر. ويُطْلَب من كاتب المقال الخاص تقديم تقرير واضح يتّسم بالدقة والإيجاز عن مجال البحث تمهيداً للمقال. وتنشر المجلةُ أيضاً مقالات المراجعة في الحقول الفيزيائية النشطة سريعة التغيُّر، وتُشَجّع كاتبي مقالات المراجعة أو مُستَكتبيها على إرسال مقترحٍ من صفحتين إلى رئيس التحرير. ويُرْفَق مع البحث المكتوب باللغة العربية ملخص (Abstract) وكلمات دالة (Keywords) باللغة الإنجليزية.

ترتيب مخطوط البحث

يجب أن تتم طباعة مخطوط البحث ببنط 12 نوعه Times New Roman، وبسطر مزدوج، على وجه واحد من ورق A4 (21.6 × 27.9 سم) مع حواشي 3.71 سم ، باستخدام معالج كلمات ميكروسوفت وورد 2000 أو ما اسْتَجَد منه. ويجري تنظيم أجزاء المخطوط وفق الترتيب التالي: صفحة العنوان، الملخص، رموز التصنيف (PACS)، المقدّمة، طرق البحث، النتائج، المناقشة، الخلاصة، الشكر والعرفان، المراجع، الجداول، قائمة بدليل الأشكال والصور والإيضاحات، ثَمّ الأشكال والصور والإيضاحات. وتُكْتَب العناوين الرئيسة بخطٍ **غامق**، بينما تُكْتَب العناوين الفرعية بخطٍ *مائل*.

صفحة العنوان: وتشمل عنوان المقالة، أسماء الباحثين الكاملة وعناوين العمل كاملة. ويكتب الباحث المسؤول عن المراسلات اسمه مشارا إليه بنجمة، والبريد الإلكتروني الخاص به. ويجب أن يكون عنوان المقالة موجزا وواضحا ومعبرا عن فحوى (محتوى) المخطوط، وذلك لأهمية هذا العنوان لأغراض استرجاع المعلومات.

الملخص: المطلوب كتابة فقرة واحدة لا تزيد على مائتي كلمة، موضحة هدف البحث، والمنهج المتبع فيه والنتائج وأهم ما توصل إليه الباحثون.

الكلمات الدالة: يجب أن يلي الملخص قائمة من 4-6 كلمات دالة تعبر عن المحتوى الدقيق للمخطوط لأغراض الفهرسة.

PACS: يجب إرفاق الرموز التصنيفية، وهي متوافرة في الموقع http://www.aip.org/pacs/pacs06/pacs06-toc.html.

المقدمة: يجب أن توضّح الهدف من الدراسة وعلاقتها بالأعمال السابقة في المجال، لا أن تكون مراجعة مكثفة لما نشر (لا تزيد المقدمة عن صفحة ونصف الصفحة مطبوعة).

Subscription Form

Jordan Journal of PHYSICS

An International Peer-Reviewed Research Journal issued by the Support of the Scientific Research Support Fund

Published by the Deanship of Research & Graduate Studies, Yarmouk University, Irbid, Jordan

Name: ..... الأسم:

Specialty:..... التخصص:

Address: ..... العنوان:

P.O. Box:..... صندوق البريد:

City & Postal Code: ..... المدينة/الرمز البريدي:

Country: ..... الدولة:

Phone: ..... رقم الهاتف:

Fax No:..... رقم الفاكس:

E-mail:..... البريد الإلكتروني:

No. of Subscription: ..... عدد الإشتراكات:

Method of Payment:..... طريقة الدفع:

Amount Enclosed:..... المبلغ المرفق:

Signature: ..... التوقيع:

Cheques should be paid to Deanship of Research and Graduate Studies - Yarmouk University.

I would like to subscribe to the Journal
For

- One Year
- Two Years
- Three Years

One Year Subscription Rates

	Inside Jordan	Outside Jordan
Individuals	JD 8	€ 40
Students	JD 4	€ 20
Institutions	JD 12	€ 60

Correspondence

Subscriptions and Sales:

Prof. Ibrahim O. Abu-AlJarayesh
Deanship of Research and Graduate Studies
Yarmouk University
Irbid – Jordan
Telephone: 00 962 2 711111 Ext. 2075
Fax No.: 00 962 2 7211121

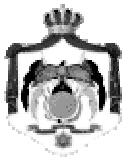

المملكة الأردنية الهاشمية

جامعة اليرموك

المجلة الأردنية

للفيزياء

مجلة بحوث علمية عالمية متخصصة محكّمة

تصدر بدعم من صندوق دعم البحث العلمي

المجلد (7)، العدد (2)، 2014م / 1436هـ

المجلة الأردنية

للفيزياء

مجلة بحوث علمية عالمية محكّمة

المجلد (7)، العدد (2)، 2014م / 1436هـ

المجلة الأردنية للفيزياء: مجلة علمية عالمية متخصصة محكّمة تصدر بدعم من صندوق دعم البحث العلمي، وزارة التعليم العالي والبحث العلمي، الأردن، وتصدر عن عمادة البحث العلمي والدراسات العليا، جامعة اليرموك، إربد، الأردن.

ترسل البحوث إلى العنوان التالي:

الأستاذ الدكتور نهاد عبد الرؤوف يوسف
رئيس تحرير المجلة الأردنية للفيزياء
عمادة البحث العلمي والدراسات العليا، جامعة اليرموك
إربد ، الأردن
هاتف 7211111 2 962 00 **فرعي** 2075
E-mail: *jjp@yu.edu.jo*
Website: *http://Journals.yu.edu.jo/jjp*